ENGINEERING POLYMER SURFACE CHEMISTRY AND TOPOGRAPHY VIA ADDITIVE MIGRATION AND PHYSICAL SECTIONING

BY

HONGYAN GU, B. Eng., M. Eng.

A Thesis

Submitted to the School of Graduate Studies

in Partial Fulfillment of the Requirements

for the Degree

Doctor of Philosophy

McMaster University

ENGINEERING POLYMER SURFACE CHEMISTRY AND TOPOGRAPHY

DOCTOR OF PHILOSOPHY (2011) McMaster University
(Chemical Engineering) Hamilton, Ontario

TITLE: Engineering Polymer Surface Chemistry and Topography via Additive Migration and Physical Sectioning

AUTHOR: Hongyan Gu,
B. Eng. (Zhejiang University)
M. Eng. (Zhejiang University)

SUPERVISOR: Professor Shiping Zhu

NUMBER OF PAGES: xxxii, 218

Abstract

Advanced polymer surface modification technologies allow modification of polymers with various functionalities or robustness to environment. However, existing technologies are still facing challenges in modifying plastic parts that have large dimensions or complex geometries. Furthermore, to obtain long-lasting surface modification, some materials must be surface-treated with plasma or harsh chemicals, and such pretreatments significantly complicate operations and increase costs.

We proposed a surface-active-additive (surfadditive) approach that is fundamentally different from existing post-treatment methods for surface chemistry modification. Our strategy was to design a type of additives that migrate to the surface of a plastic part during manufacturing and entangles with bulk polymer chains to achieve stable surface properties. Two types of surfadditives were synthesized in this work. The first type is a block copolymer having the “head-neck-body” structure. The “head” and “neck” of the chain molecule consist of a low-surface-energy component such as fluorinated segments and a reactive component such as triethoxy silane. The “body” of the surfadditive is polymethyl methacrylate (PMMA), which is designed for applications in acrylic plastics. The second type of surfadditives is hybrid magnetic material, which was synthesized by grafting polymer chains that contain nanosilica cages and PMMA backbone from iron nanoparticles. The polymeric surfadditives were applied in the injection molding and casting processes of PMMA. The effect of processing temperature, surfadditive structure, concentration, and mold material on the surface modification were investigated.

In exploring new surface physical property modification techniques, we developed a new one-step nanopatterning method for topography construction that is based on chattering. Chatters are unwanted wavy structures generated from vibrations in cutting. They are mostly random in size because of uncontrolled vibration frequencies. Using an oscillating diamond knife with tunable oscillation frequency in ultramicrotomy, we succeeded in obtaining control over chattering. This “controlled chattering” method was demonstrated to be an excellent technology to fabricate wavy surface patterns on a variety of materials including thermoplastic, thermosetting and soft metals. The size of wavy patterns prepared by this method was tunable from 30 nm to micrometer scale through adjusting cutting speed and oscillation frequency. The effects of materials’ mechanical properties and cutting speed on the pattern formation were systematically investigated. In addition, the controlled chattering was also extended to the fabrication of one-dimensional polymer and metal nanowires with ultra-high aspect ratios up to 10^4. Different morphologies such as nanoribbons, nanorods were obtained through oscillation phase adjustment. The size of nanowires was found tunable through adjusting cutting depth, cutting speed, as well.

Acknowledgements

First and foremost, I would like to express my deepest gratitude to my supervisor, Dr. Shiping Zhu, for his continuous guidance, encouragement and support during my PhD study. His dedication to work, insight into science, and concern about students really impressed me and had been a source of motivation for me to achieve my goals. I treasure all the advices and trainings received from him, without these, I would never have grown and been stimulated so much. I simply could not wish for a better and friendlier supervisor.

I'm also grateful to Dr. Santiago Faucher, who co-supervised part of my thesis and provided me with lots of useful discussions and suggestions. He is an intelligent, passionate and capable person from whom I have a lot to learn.

I thank my committee members, Dr. John Vlachopoulos and Dr. Gianluigi Botton for their inspiring discussions and valuable advices.

It has been my best experience to work in the Zhu group with so many great people. My appreciation is extended to Dr. Junwei Zhang, Dr. Wei Feng, Dr. Renxu Chen, Dr. Xiang Gao, Dr. Zhilin Jin, Dr. Zhenggang Xiao, Rachel Gong, Sara Alibeik, Mark Machado, Mohammad Haj-Abed, Jason Doggart, Tom Kowpak, Mark Rattle, Meng Li, Hongyu Lu, Weifeng Liu, Rummana Syeda, Cam Derry, who helped and supported my research. I especially thank Nels Grauman who helped me with some revision work and contributed lots of time to the group activities.

I would also like to thank Dr. Carlos Filipe for providing me generous access to their UV spectrometer for diffusion experiments. I am grateful to Dr. Yang Chen, Dr. Nick Burke (Chemistry and Chemical Biology), Dr. Zhilin Peng (Centre for Emerging Device Technology), Dr. Ravi Selvaganapathy, Dr. Stephen Veldhuis, Dr. Michael Bruhis (Mechanical Engineering), Dr. An-chang Shi, Dr. David Venus (Physics and Astronomy) for helpful discussions. Marcia Reid from Electron Microscopy Facility helped me a lot in preparing samples and was always willing to help.

The department of Chemical Engineering provided me with a great environment for study and research. Kathy Goodman, Lynn Falkiner, Naci Cole, Doug Keller, Justyna Derkach, Dan Wright have always been very helpful. Paul Gatt is the most handy and efficient technician I have ever known. Without his help, my thesis would never have been completed.

I appreciate the financial supports from Natural Science and Engineering Research Council, and Ontario Centre of Excellence.

Finally, I thank my parents, my brother and my husband Huaifeng Hua for their selfless love and support throughout all these years. I am most grateful to my husband for giving me constant encouragement in the pursuit of my goals.

Preface

The thesis is of the sandwich style and is based on the following journal articles or manuscripts:

- Gu H.; Zhang J., Faucher S.; Zhu S. Novel polymeric surfadditives synthesized via atom transfer radical polymerization and their surface migration properties. *Macromolecular Reaction Engineering*, 2011, in press.

- Gu H.; Faucher S., Zhu S. Magnetic organo-silica nanoparticles for localized polymer surface modification, *Macromolecular Materials and Engineering* 2011, accepted for publication.

- Gu H.; Zhang J.; Faucher S.; Zhu S., Controlled chattering - a new "cutting edge" technology for nanofabrication, *Nanotechnology*, 2010, 21: 355302.

- Gu H.; Faucher S.; Zhu S. Controlled Chattering on PMMA and epoxy: effect of crosslinking and cutting speed on pattern formation, *Polymer, 2011*, 52: 2525-2531.

- Gu H.; Zhu S. A mechanical approach for the fabrication of polymer and metal nanowires, *Nanotechnology*, 2011, 22: 265355.

- Gu H.; Faucher S.; Zhu S. Diffusion of semi-flexible polyelectrolyte through nanochannels, *AIChE Journal*, 2010, 56(7): 1684-1692.

Table of Contents

List of Schemes

List of Figures

List of Tables

Nomenclature

a	size of monomeric unit in semi-flexible chain
A_s	polycarbonate membrane surface area in a diffusion cell
A	amplitude of oscillation input (V)
AFM	atomic force microscopy
AIBN	azobisisobutyronitrile
APTES	(3-aminopropyl)trimethoxysilane
ATRP	atom transfer radical polymerization
BiBB	α-bromoisobutyryl bromide
Br-MTESP	2-bromo-2-methyl-N-(3-(triethoxysilyl)propyl)
propanamide	
c	polymer concentration in diffusion cell
c_m	monomer concentration in solution for calculation of Debye screen length
$CaCl_2$	calcium chloride
Cu	copper
CuBr	copper bromide
Δc	concentration difference across diffusion membrane
$CDCl_3$	deuterated chloroform
CFRP	controlled free radical polymerization
d	wavelength of wavy structures (nm)

d_{Fe}	the density of iron (7.874 g/cm^3)
D_0	diffusion coefficient in bulk
D_{blob}	predicted diffusion coefficient based on blob theory
D_{eff}	effective diffusion coefficient as measured
D_{Rouse}	diffusion coefficient in Rouse model
DI	de-ionized
DMF	dimethylformamide
DMSO	dimethyl sulfoxide
EDX	energy dispersive X-ray analysis
EGDMA	ethylene glycol dimethacrylate
EO	ethylene oxide
Fe-I	iron nanoparticles grafted with ATRP initiator on surface
FEP	fluorinated ethylene propylene
Fe-POSS	iron nanoparticles grafted with POSS polymer
Fe-POSS-PMMA	iron nanoparticles grafted with POSS-MMA copolymers
FTIR	Fourier transform infrared spectra
g	number of monomeric units inside a blob
GPC	gel permeation chromotography
h	oscillation frequency in controlled chattering (kHz)
HV	Vikers hardness
k	mass transfer coefficient
k_0	constant factor in prediction of polyer surface tension

k_B	Boltzmann constant
k_p	propogation rate
k_{act}	radical activation rate in ATRP
k_{dact}	radical deactivation rate in ATRP
l	membrane thickness or nanochannel length
l_p	persistence length
l_B	Bjerrum length
$l_{//}$	dimension of polymer chain inside nanotube based on blob theory
L	length of polymer along its contour
$\mathrm{L_n}$	complexing ligand in ATRP
m	orders of diffraction
M	general molecular weight polymer
MMA	methyl methacrylate
$\mathrm{M_n}$	number average molecular weight of polymer
$\mathrm{M_W}$	weight average molecular weight of polymer
$\mathrm{M_t^m}$	transition metal
n	moles of polymer molecules diffused through porous membrane in diffusion experiment
N_A	Avogadro’s constant
N	degree of polymerization
N^*	number of blobs in a polymer chain

NaCl	sodium chloride
$NaHCO_3$	sodium bicarbonate
NMR	nuclear magnetic resonance spectroscopy
p	porosity of the membrane (%)
PC	polycarbonate
PCTE	track-etched polycarbonate membrane
PDI	polydispersity index of polymer molecular weight
PEG	polyethylene glycol
PFDA	1H,1H-perfluoro-n-decyl acrylate
PFNOL	1H,1H-perfluoro-1-nonanol
PFOBMP	(perfluoro-octyl)-2-bromo-2-methyl-propionate
PFO-SiMA-MMA	block copolymer with a fluorinated head, siloxane neck and PMMA body
PMDETA	N,N,N’N’-pentamethyldiethylenetriamine
PMMA	poly(methyl methacrylate
polyOEGMA	poly(oligoethylene glycol methacrylate)
POSS	polyhedral oligomeric silsesquioxanes
PS	polystyrene
R	radius of magnetic nanoparticles
$R\cdot$	radical
R_g	radius of gyration
R-X	dormant species in ATRP

R_H	hydrodynamic radius of a polymer chain in solution
R_t	radius of a nanochannal
s_b	pattern size on block surface (nm)
SEM	scanning electron microscopy
SI-CFRP	surface initiated controlled free radical polymerization
SI-ATRP	surface initiated atom transfer radical polymerization
s_s	pattern size on thin sections (nm)
SMMs	surface modifying molecules
t	duration of diffusion experiments (s)
T	absolute temperature
T_g	glass transition temperature
TEA	triethylamine
TEM	transmission electron microscopy
TEOSi-FMA-MMA	block copolymer with a siloxane head, fluorinated neck and PMMA body
TESPMA	methacryloxypropyl 3-(triethoxysil) propylmethacrylate
TGA	thermogravimetric analysis
THF	tetrahydrofuran
TFT	trifluorotoluene
v	cutting speed (mm/s)
W	weight loss of samples in TGA measurement
WCA	water contact angle

XPS	X-Ray photoelectron spectroscopy

Greek letters

α	knife angle
α_c	clearance angle in microtomy
δ	boundary layer thickness
γ	the ratio of blob radius over tube radius when a polymer chain was confined in a tube
γ_s	surface tension of polymer
γ_∞	surface tension of a polymer with infinite molecular weight
θ_i	angle of incident light
θ_m	diffraction angle
η	liquid viscosity
κ^{-1}	Debye electrostatic screen length
λ	Odijk length scale
w	width of rod in Odijk model
ζ_{chain}	friction coefficient of a confined chain in a small tube

Chapter 1 Introduction

Polymers have been widely used for decades since they have excellent bulk mechanical properties, are inexpensive and are easy to process. In many applications, such as adhesion, self-cleaning, scratch/abrasion resistance, biological separation, optical reflection/diffraction, nanotechnology, etc., the surface chemical and physical properties of polymers play an important role in their successful use. Studies on polymer surface modification techniques has been very intensive in the past decades, and the advances in polymer surface engineering techniques have allowed for endowing polymer surfaces with various properties without affecting the bulk, thus transforming inexpensive plastic materials into valuable finished products.

1.1 Background

1.1.1 Coating and Polymer Surface Modification

Among the surface chemistry modification technologies, coating is the most widely used method that is able to incorporate variable chemistry onto a polymer substrate. A coating is defined as "a liquid, viscous or powdery product (mixture) that results in a solid layer after application on a substrate and subsequent drying"[1]. Coatings can be in many forms depending on the purpose of application and can be applied to various materials using many techniques; for example, powder-like or other solid materials can be deposited onto a substrate surface by sputtering or vapor deposition methods. These techniques, including physical vapor deposition (PVD)[2,3] or chemical vapor deposition (CVD)[4-7], usually involve an evaporation procedure either by raised temperature or pressure to form a homogeneous phase for controlled and uniform deposition. Therefore, these operations are mostly conducted in closed chambers. These techniques allow for the deposition of very thin films with precisely controlled thickness, and are used mostly for applications of high-end products such as lenses or delicate devices. However, there are also drawbacks to these coating methods: for example, the deposition chamber is only available for small-sized parts, the types of coating materials are very limited and the operation costs are relatively high as compared to other coating techniques. Liquid coatings such as paints or lacquers are normally applied by the wet coating method. This type of coatings has the most diversity in functions and can be carried out in a do-it-yourself manner or at an industrial scale. Among the various decorative coatings, surface protective coating based on a sol-gel process is an important category[8-10]. In general, the key factor contributing to a protective layer is the formation of three dimensional polymer/hybrid structures[11]. Since the wet coating process involves solvent evaporation, crosslinking along with volume change, it is difficult to precisely control the coating thickness. For some inert materials such as polyolefin, acrylic or polycarbonate, it is also challenging to achieve good adhesion between the coated layer and substrate without using special treatment or modifier.

Although coating is a very useful approach to modify materials' surface properties and has been used over a long history, the disadvantages of coating are quite obvious with regard to economic and ecological concerns. First, the sequential operations steps for coating significantly increase the cost of manufacturing. For example, the extra cost for a scratch resistant coating on optical lenses is normally about 50-200% more. Secondly, for wet coating, the application efficiency of coating is normally low since the major component of the coating dispersion is solvent and eventually it evaporates to the environment. Meanwhile, there is also the potential of serious problems arising from the evaporating solvent. In many applications, the solvents used to disperse coating material are mostly organic solvents, which are harmful or even toxic to human health. New legislation has exerted a force on the coating industry to seriously decrease the use of solvents or to find "greener" chemical replacements.

1.1.2 Polymer Migration/ Segregation and Surface Modification

In most applications, polymer additives should be homogeneously dispersed within the bulk material for property modification. Phase segregation caused by insufficient dispersion or poor compatibility of additives could result in defects or even fail to maintain desired properties. However, in some situations, controlled additive segregation could be taken advantage of to achieve specified local functions. One example is the lubricated plastic molding, where spontaneous surface migration of additive to the surface/interface results in an additive-rich layer around the molded parts, hence facilitating mold separation[12]. These additives, normally named as molding-aids, are typically short chain alkanes, fluorinated oligomers, or highly branched molecules, which preferentially partition near host material surface due to lower surface/interface energy. The molding-aid agents could form a low-viscosity fluid or low-friction layer between the polymer/mold wall interface and act as lubricant in mold separation.

One mechanism that describes the surface migration of additives is the surface free energy difference[13]. The surface free energy is defined as "the work required to increase the area of a substance by one unit area". For polymer blends with multiple components exposed to air, the polymer species with lower surface free energy take precedence of concentrating at the polymer-air interface, and thus the total interfacial tension of the system was minimized. In general, migration force is proportional to the surface energy difference between the host polymer and additive[14-16]. This relationship has been used to explain the surface enrichment phenomenon of miscible polymer blends such as PS-b-PEO/PS[17] and poly(vinyl methyl ether)/polystyrene (PVME/PS)[18], or immiscible blends as poly(dimethyl siloxane)/polystyrene[19-22]. However, the surface migration of molecules regarding to surface free energy difference is not limited to additives with different chemical components. It could also happen to polymer blends with different chain length distribution. The surface tension of polymer scales as $\gamma_s = \gamma_\infty - k_0/M_n^\alpha$,[23, 24] where γ_∞ is the surface tension for a polymer with infinite molecular weight, k_0 is constant factor depending on the nature of a given molecule. k_0 can be positive, negative or zero for different compositions and structures of the molecule. For instance, when PDMS is terminated with hydrophilic end groups, $k_0 \approx 0$. Therefore, the effect of chain length on surface tension is negligible. However when PDMS is terminated with hydrophobic groups, k_0 is found to be positive. That is, the surface tension of hydrophobic PDMS increases with its chain length.

Table 2.1 Surface tensions for various materials

Material/ chemical constitution	**Surface tension (mN/m = dyn/cm)**
polyamide	32-46
polyester	40-49
polycarbonate	43-47
poly(methyl methacrylate)	31-41
polystyrene (PS)	37-43
Polyurethane	36-39
organosilane	30-50
fluorinated acrylic polymer	10-20

Surface tension values of some common materials or chemical components measured at 20°C are listed in Table 1.1[25, 26]. Most polymers such as polyamide, polycarbonate, polyester, PMMA, PS, polyurethane or organosilanes have the surface tension between 30-50 mN/m. Ranges of values were given because surface tension is dependent on chemical composition and chain structures. However, the surface tension of fluorinated acrylic polymers is only about 10-20 mN/m, which is significantly lower than others. Because of this, fluorinated molecules have been the most studied as surface modifying molecules (SMMs) in recent years. McCloskey et al. synthesized fluorine containing macromolecules which effectively migrate to the surface of poly(urethane urea)[27]. Hopken[28] and Shimizu[29] independently reported that their copolymers with fluorinated segments migrate towards the surface and formed a separated domain. Suk et al. studied the surface enrichment of polymer chains with both ends capped with fluorinated units[30], and explained the surface enrichment of fluorinated segments as a result of both conformational rearrangement and migration.

Another theory that explains the preferential surface partition is configurational entropy. The hypothesis is that each segment of polymer chains has much lower configurational entropy near rigid surfaces than in bulk polymer systems[31, 32]. Therefore, it results in greater concentration of polymer chain ends at surfaces. This theory is proven to be useful for explaining the migration phenomena in homopolymer melt systems, where smaller polymer chains migrate to the surfaces of long chain polymers.

As compared to coating, surface modification by surface-active molecule migration and segregation is simpler in terms of operation. Furthermore, the new surface layer formed by the aforementioned mechanism is a composite layer that is molecularly integrated into the bulk; therefore, the adhesion problems existing in some coating situations can be solved without costly post-treatment. The possibility of achieving various surface modifications with surface-active molecule migration mainly depends on the design and synthesis of functional/telechelic polymers, which should be integrated with surface-active constitutions, compatible segments and functional groups. However, current studies on the polymer surface migration are still preliminary, focusing mostly on homopolymers or 2-block copolymers.

1.1.3 Atom Transfer Radical Polymerization and Functional Polymer Synthesis

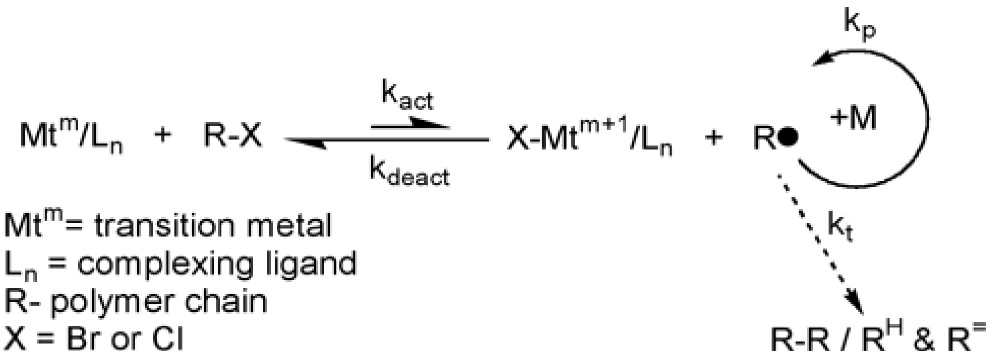

Scheme 2.1 Schematic representation of ATRP process

Free radical polymerization has been widely employed in the production of acrylic, vinyl and olefinic polymers under ample environments. It is the most frequently used technique as compared to other techniques (ionic or condensation polymerization) as it has mild tolerance to impurities, requires moderate reaction conditions and is flexible with regards to the selection of polymerization processes. Furthermore, the controlled Free Radical Polymerization (CFRP) allows for tailoring macromolecules with precisely controlled molecular weights and compositions. Among the CFPR techniques, Atom Transfer Radical Polymerization (ATRP) polymerization is one of the mostly studied. It has been applied to the controlled polymerization of a wide range of monomers including (acrylates, methacrylates, styrenes, vinylpyridines, acrylamides, acylonitrile)[65]. Schematic illustration of the ATRP mechanism is shown in Scheme 1.1[66]. The control of ATRP was achieved through the reversible deactivation and reactivation of radicals ($R^{\cdot}$) and dormant species (R-X) by halogen exchange with a transition metal complex. In the deactivation process, propagating radicals are end-caped with halogens cleaved from the transition metal complex at its oxidized state. The transition of radicals into dormant species results in a low radical concentration, therefore minimizing irreversible termination. Meanwhile, some of the dormant species are reactivated by the redox reaction with the metal complex, which releases active radicals to propagate with monomers. In this manner, polymer chains grow slowly and steadily with tunable structure. Alkyl halide (e.g. Ethyl α-bromoisobutyrate, tert-Butyl α-bromoisobutyrate) or functionalized halides (e.g. 2-bromo-2-methyl-N-(3-(triethoxysilyl)propyl) propanamide or BMTP, synthesized in our lab) are typical types of initiator[67-72]. Transition metals (e.g. Cu)[73-75] complexed with a ligand (bidentate nitrogen, bipyridine/tripyridine derivatives, diamine/triamine derivatives, etc.[76]) are normally used as catalysts. Since ATRP is tolerant to many functional groups such as allyl, amino, epoxy, hydroxy and fluorinated functional groups presented in the initiator or monomers, it is a facile approach to synthesize mono- or multi-functional polymers. For instance, to synthesize a fluorinated polymer, one can either use fluorinated initiator[77, 78] or fluorinated monomers in an ATRP process[79-82]. To obtain multi-functionality, different combinations of functional initiators or monomers in a batch or semi-batch process can be used.

1.1.4 Surface Modification by Polymer Grafting

Polymer grafting is a special type of coating method that makes a single layer of polymer chains with one end tethered to the substrate. Based on this mechanism, the surface grafting can be mainly divided into two categories: "grafting to" and "grafting from" approaches[33,34]. In the former approach, prefabricated polymer chains are attached to a surface by covalent bonding or physical interaction between one chain-end and the substrate surface. Due to steric repulsion and diffusion-controlled interaction[35,36], achieving high grafting density is a challenge for this method. In the "grafting from" approach, polymer chains are directly initiated from an immobilized surface modified with initiator. Since monomers are smaller than polymer chains, the steric and diffusion effects become less significant in this case; therefore higher grafting density can be achieved. By clever selection of an initiator, surface grafting can be carried out in a number of controlled processes including anionic[37-39], cationic[39-42], ring-opening[43-45] or free radical polymerizations. In particular, the controlled living processes are of most interest as they allow for preparation of brushes with controlled thickness, composition or structure. Among various means of Surface Initiated- Controlled Free Radical Polymerizations (SI-CFRP), ATRP is the most studied approach that is used to graft polymers onto various materials' surfaces. Surface initiated ATRP (SI-ATRP) was firstly reported by Huang and Wirth, who successfully grafted poly(aryliamide) brushes onto benzyl choride functionalized porous silica[46]. Later, intensive studies were carried out for the synthesis of various polymers, e.g. polymethyl methacrylate (PMMA)[47], polystyrene (PS)[48], poly(hydroxyethyl methacrylate)[49], Poly(oligoethylene glycol methacrylate) (polyOEGMA)[50] and PS-b-PMMA brushes[51] and other polymers on a variety of surfaces. While proof of concept studies of SI-ATRP are mostly carried out on planar substrates concerning convenience of characterization, later studies have also been intensively conducted for grafting polymer chains onto particle surfaces. The covalently attached polymer brushes could not only provide particles with good stability against aggregation, but also could be integrated with unique particles to generate new types of advanced materials. A variety of polymers have been successfully grafted from many types of nanomaterials including silicon dioxide[52-55], metal[56,57], metal oxide[58-61], or clay[62-64].

Surface grafting of polymer chains provides accurate control over surface chemistry and coating thickness, however it is an inherently expensive approach that requires multi-step operations such as surface pretreatment, polymerization and purification. The operation of ATRP normally has to be conducted in oxygen-free environment. This makes direct applications of surface grafting on large scale impractical. On the other hand, if surface grafted products, particularly particle-based products, could be efficiently used as additives for localized functioning, the extra unit cost from a new ingredient could become insignificant. In other words, on a low-level loading basis, the application functional additive for specified modification is feasible.

1.1.5 Challenges in Surface Modification and Surfadditive Proposal

In summary of the existing surface chemistry modification methods, coating is the most widely used but still has drawbacks such as high cost, size limitation, poor adhesion or environmental concerns in various means. To achieve permanent adhesion of the coated layer to the substrate, some materials have to be surface treated by plasma or chemical etching prior to coating. This again adds to the complexity of a coating process. In this respect, surface modification by surface-active polymer migration seems to be favorable since it does not involve any additional facilities. Nonetheless, the adhesion of the surface functional layer could be superior, as the migrated molecular chain ends are entangled with the host polymer chains. Although current study of polymer surface migration is very preliminary and is limited to homopolymer or monofunctional copolymers, the potential of expanding its versatility with more complicated polymers is quite promising. Recent developments in living radical polymerization have allowed for facile synthesis of block copolymers with multiple functionalities. Consequently, many functional monomers, such as acrylate derivatives, are commercially available, and a wide selection of functionalities from polyethylene glycol (PEG), fluorocarbon, siloxane, amine, nanisilica, etc. can be obtained. These chemicals can be readily used in ATRP processes to construct well-defined multifunctional polymer structures.

The polymer surface grafting approach has been well studied in the recent years and can be used to incorporate almost every type of polymers onto a broad range of surfaces. Although it appears uneconomical to be used as a direct modification method for large-scale applications, it provides another feasibility to be used as additive for modifying polymer surfaces. In surface modification, it is estimated that only a small amount of material is needed to form a new complex layer. For example, to cover the surface of a 5mm-thick bulk material, the amount of nanoparticles needed is less than of 0.01vol%, if there is 500 nm-thick nanoparticle-rich layer is to be produced. A good selection of application methods with high application efficiency is capable of turning an expensive ingredient into a negligible part. In fact, the effective use of ingredient/additive eventually relies on how it is effectively and easily manipulated. Perhaps one of the most direct ways of manipulation is magnetic response. By using magnetic materials such as nickel, iron, or iron oxides nanoparticles as vehicles, functional structures attached to these particles could be delivered to desired locations of a polymer product. The attachment of functional species onto magnetic particles can now be easily conducted using SI-ATRP technology.

In order to develop a new surface modification approach that integrates the molding and coating procedure, we started the “polyshell” project in Aug. 2008. The objective of the project is to develop either a polymeric or nanoparticle based surface-active-additive (termed as “surfadditive”) that migrates to the surface of the polymer part during processing to form a stable functional shell. Our concept, developed in this work, would allow the additive to be premixed into the resin such that no additional processes or steps are required following mold release. The characteristics of the surfadditive technology should comply with the following facets:

1. The additive to be designed should have at least one segment compatible with the bulk material and the other segment(s) providing functionality and surface migration. The functionality can be chosen from copolymerization of derivative monomers having hydrophilic/hydrophobic or reactive segments. Surface migration ability of the surfadditives can be obtained by incorporating segments with low surface energy such as fluorinated units into the polymer chain, or using magnetic particles that can be manipulated by magnetic field.
2. For the polymeric surfadditive, since the surface energy driven migration of polymer in a polymer matrix is dependent on its molecular weight, the polydispersity of polymer chains should remain low to achieve uniform and faster migration. Polymer chains with low polydispersity can be synthesized by CFRP.
3. The chain length of polymer sufadditive should be sufficiently long, otherwise it could be leached out of the matrix easily during application. Thus the molecular weight of additive polymer needs to be optimized by controlling the reaction time in a controlled radical process.

4. The surfadditive should have sufficient stability during molding process or in storage. Its moisture/heat/pH sensitivity should be optimized.

To make practically useful surfadditives, commercially available or low-cost monomers/fillers should be considered with priority. The modified polymer surface should also have the properties comparable or even superior to the existing products.

1.2 Surface Topography Modification/ Patterning

1.2.1 Current Techniques of Surface Patterning

Besides chemistry modification, surface engineering has also taken into account the control of morphology (roughness, topography). Techniques capable of fabricating well-defined surface structures at nano- or micrometer scales (patterning), have been intensively studied. On surface patterning, lithography was an indispensable contributor which accomplished all kinds of topographic structures[83]. Conventional lithography, including projection lithography and scanning beam lithography has been well studied and highly developed for the patterned structures. However, it requires high capital cost facilities and is not suitable for high throughput application. In comparison, some of the unconventional lithographic (or nonlithographic) methods such as replica molding[84-86], embossing[87,88], microcontact printing[89-91] and edge lithography[92,93] are more cost effective and offer alternatives to fabricate more complicated structures on a variety of materials. However, the mold/mask/templates used in unconventional lithographic methods have to be fabricated by conventional lithographic methods or molecular-self assembly. Although the material selectivity or structure versatility of lithographic techniques can be improved by a combination of different operations in unconventional approaches, the tedious operations as well as low productivity and waste are major obstacles for large-scale application.

1.2.2 Chatters in Imbalanced Cutting

Cutting is a dynamic process between the cutting tool and workpiece. There are many types of cutting tools designed for difference purposes: e.g., saw, drill, milling cutter, lathe, blade, knife, scissors, etc. Among all kinds of cutting process, orthogonal cutting using a knife/blade is the simplest one. Ideally, any cutting process should be conducted at a stable condition; therefore it generates separated parts with high quality surface finish. However, due to multitude facts (e.g., environmental resonance, inhomogeneity in sample, poor alignment) or external disturbances, there are always vibrations of the cutting tool or work piece occurrent. Such vibrations directly render uneven cutting forces exerted on the work piece. Opposing the cutting force, there is a corresponding force from the work piece to balance it. In most situations, it takes time for the corresponding force to change accordingly, and this small delay induces a force imbalance in the system. The imbalanced cutting then leads to uneven cut in depth and generates groovy structures, which are normally called “chatters”. Since most vibrations are unexpected and random in frequency, chatters are normally not uniform in size. In fact, it is known that chatters result from vibration cutting and the period of chatters is determined by the frequency of vibration. In practice, people who experience chatters most, including mechanical engineers and technicians, are making every effort trying to minimize or eliminate chatters. Unfortunately, no one has ever thought about making use of chattering.

1.2.3 A Precision Cutting Tool: Ultramicrotome

In physical sectioning/cutting, ultramicrotomy is one of the most precise facilities that are capable of making high quality sections. The sections prepared by ultramicrotomy are mostly used in electron microscopy, where specified thickness from nano- to micrometer scale is needed for high-resolution imaging. The photograph of a microtome (Leica UCT®) is shown in Figure 1.1. In general, the operation of microtomy is based on the controlled advance and stroke of the sample holder towards a stationary knife in controlled steps. The facility can be programmed to make consecutive cuts with desired cutting depth and speed. In each cut, first, the sample arm is given an incremental advance that determines the depth of cut; then it moves downwards delivering the specimen to the stationary knife. During the down stroke of the sample arm, the sample is forced against the edge of the knife, resulting in a thin section being cut. After that, the sample arm returns back to the original position before the next step begins. The mechanism controlling the stepping and advance of sample holder is generated by a uniquely designed stepping motor and an internal lever, which transforms micrometer-increment into nanometer-increment steps[92]. The transformation is so precise that each increment can be controlled to a range of 1 nm. Sections prepared by ultramicrotomy are normally collected by the wet-sectioning method. That is, the knife is integrated to a “boat” filled with water. The water-filled boat has two functions: firstly, it lubricates the cutting process, thus reducing damage of the sections. Secondly, the section that falls from the knife-edge, floats on the water surface and can be easily picked up using a loop or TEM grid.

Figure 2.1 Photograph of the Leica UCT ultramicrotome.

During ultramicrotomy, the sections are more or less compressed along the cutting direction. The degree of compression is dependent on the angle of knife, cutting parameters and/or the properties of the materials. However, it is very difficult to totally eliminate compression. In 2000, Studer and Genaegi invented an oscillating knife for ultramicrotomy with the aim to reduce compression[94]. The oscillating knife consisted of a regular diamond knife (45° knife angle) mounted with a piezo-transducer (0-2000 Hz). At low cutting speeds (0.05-0.2 mm/s), it was found that the application of oscillating diamond knife almost eliminated compression on PS samples. Later, an oscillating cryo-knife was developed to reduce compression of vitreous sections. Al-amoudi et al. then studied the effects of oscillation on sectioning dextran aqueous systems containing yeast and PS beads using a 35° oscillating knife[95]. At the cutting speed of 0.4 mm/s, it was found that the compression was reduced to 15-25% from 40-45% with an optimal frequency of 20-25 kHz. They speculated that the compression reduction is because that the oscillation cutting reduces cutting angle when the speed of the knife (vibration speed) exceeds the speed of sample (cutting speed)[94]. In Al-amoudi's study, it was measured that the amplitude of the knife-edge at 20-25 kHz was about 20 nm. That is, the mean speed of the knife-edge was 0.4-0.5 mm/s, which is close to the speed of the moving sample during cutting. Upon this, it can be expected that the compression reduction effect could be more profound if the oscillation frequency is higher or the sample speed is slower.

With a fixed oscillation frequency, lower cutting speed is therefore favorable for reducing compression.

1.2.4 The Proposal of Controlled Chattering

As mentioned in section 1.2.2, chatters are resulted from unexpected vibration during a cutting process. The size of chatters is related to the vibration frequency as well as the cutting speed. At a given vibration frequency, a higher cutting speed is prone to generate larger chatters[96]. Since chatters are unwanted, people normally operate cutting at lower speed. On the other hand, in order to reduce compression, it is preferred to conduct cutting at higher cutting speed in conventional microtomy. The invention of oscillation knife provides another approach to reduce compression during microtomy, however the oscillation cutting mechanism suggests using a low cutting speed. For example, when prepare sections for most plastic or metal specimens, cutting speed should be < 2 mm/s. In fact, the microtome can be adjusted to a wide range of cutting speeds from 10^{-2} mm/s to 10^{2} mm/s. Regardless of the original purpose of designing an oscillation diamond knife for microtomy, its capability of functioning at highly controlled oscillation frequency appears to be a valuable asset to us. We are interested in extending the chattering study using a controlled vibration cutting tool, by which the chattering frequency can be controlled at a given cutting condition. Fortunately, the commercial oscillation diamond knife is tunable from 25 kHz to 45 kHz in frequency, and 0-30 V in output voltage. Our idea was that, if vibration could be controlled, chattering should be manipulative as well. As a result, the size of wavy structure should be tunable through adjusting cutting conditions such as cutting speed or oscillation frequency. It is known that patterns with feature sizes in the nano- or sub-micrometer scale are highly demanded for applications in photovoltaic, optical or biological applications. The fabrication of highly controllable nanopatterns by means of controlled chattering represents a new nonlithographic technique for nanofabrication. In addition, the controlled chattering process is a fast operation that could be finished in one step, involves no chemical reactions or treatment, and does not generate byproducts or pollutions, which is an ideal "green" process.

1.3 References

1. Kooistra, M. F. *Verf Vademecum; kluwer TEchniek: Deventer, The Netherlands* **1995**.
2. Knotek O., L. F., Mittal K.L. *Metallized Plastics 2, Fundamental and Applied Aspects, Plenum Press, New York,* **1991**.
3. Baumer, S. *Hand book of Plastic Optics, Wiley-VCH Verlag GmbH & Co. KGaA, Weiheim* **2005**, 195.
4. Zajickova, L.; Bursikova, V.; Janca, J. *Vacuum* **1998,** 50, (1-2), 19-21.
5. Erlat, A. G.; Spontak, R. J.; Clarke, R. P.; Robinson, T. C.; Haaland, P. D.; Tropsha, Y.; Harvey, N. G.; Vogler, E. A. *J. Phys. Chem. B* **1999,** 103, (29), 6047-6055.

6. Rats, D.; Hajek, V.; Martinu, L. *Thin Solid Films* **1999,** 340, (1-2), 33-39.
7. Damasceno, J. C.; Camargo, S. S.; Cremona, M. *Thin Solid Films* **2003,** 433, (1-2), 199-204.
8. Wen, J.; Wilkes, G. L. *J. Inorg. Organomet. Polym.* **1995,** 5, (4), 343-375.
9. Haas, K. H.; Wolter, H. *Curr. Opin. Solid State Mat. Sci.* **1999,** 4, (6), 571-580.
10. Haas, K. H. *Adv. Eng. Mater.* **2000,** 2, (9), 571-582.
11. Amerio, E.; Fabbri, P.; Malucelli, G.; Messori, M.; Sangermano, M.; Taurino, R. *Prog. Org. Coat.* **2008,** 62, (2), 129-133.
12. Hong, Y.; Cooper-White, J. J.; Mackay, M. E.; Hawker, C. J.; Malmstrom, E.; Rehnberg, N. *J. Rheol.* **1999,** 43, (3), 781-793.
13. Toussaint, A. *Prog. Org. Coat.* **1996,** 28, (3), 183-195.
14. Chen, X.; Gardella, J. A.; Cohen, R. E. *Macromolecules* **1994,** 27, (8), 2206-2210.
15. Green, P. F.; Christensen, T. M.; Russell, T. P.; Jerome, R. *Macromolecules* **1989,** 22, (5), 2189-2194.
16. Petitjean, S.; Ghitti, G.; Jerome, R.; Teyssie, P.; Marien, J.; Riga, J.; Verbist, J. *Macromolecules* **1994,** 27, (15), 4127-4133.
17. O'Malloy, J. J.; Thomas, H. R.; Lee, G. M. *Macromolecules* **1979,** 12, (5), 996-1001.
18. Bhatia, Q. S.; Pan, D. H.; Koberstein, J. T. *Macromolecules* **1988,** 21, (7), 2166-2175.

19. Tanaka, K.; Takahara, A.; Kajiyama, T. *Macromolecules* **1998,** 31, (3), 863-869.
20. Nakanishi, H.; Pincus, P. *J. Chem. Phys.* **1983,** 79, (2), 997-1003.
21. Schmidt, I.; Binder, K. *Journal De Physique* **1985,** 46, (10), 1631-1644.
22. Hariharan, A.; Kumar, S. K.; Russell, T. P. *Macromolecules* **1990,** 23, (15), 3584-3592.
23. Degennes, P. G. *Comptes Rendus De L Academie Des Sciences Serie Ii* **1988,** 307, (18), 1841-1844.
24. Jalbert, C.; Koberstein, J. T.; Yilgor, I.; Gallagher, P.; Krukonis, V. *Macromolecules* **1993,** 26, (12), 3069-3074.
25. *Wiley InterScience - Wiley Database of Polymer Properties. Surface Chemical Consitution and Surface Tension: Table 1. John Wiley & Sons. Inc.* **2003**.
26. Lee, H.; Archer, L. A. *Macromolecules* **2001,** 34, (13), 4572-4579.
27. McCloskey, C. B.; Yip, C. M.; Santerre, J. P. *Macromolecules* **2002,** 35, (3), 924-933.
28. Hopken, J.; Moller, M. *Macromolecules* **1992,** 25, (9), 2482-2489.
29. Nakata, M.; Sakai, A.; Shirai, H.; Hanna, J.; Shimizu, I. *Jpn. J. Appl. Phys. Part 1 - Regul. Pap. Short Notes Rev. Pap.* **1991,** 30, (10), 2562-2568.
30. Suk, D. E.; Matsuura, T.; Park, H. B.; Lee, Y. M. *J. Membr. Sci.* **2006,** 277, (1-2), 177-185.

31. Agarwal, U. S.; Dutta, A.; Mashelkar, R. A. *Chem. Eng. Sci.* **1994,** 49, (11), 1693-1717.

32. Helfand, E.; Wasserman, Z. R. *Macromolecules* **1976,** 9, (6), 879-888.

33. Barbey, R.; Lavanant, L.; Paripovic, D.; Schuwer, N.; Sugnaux, C.; Tugulu, S.; Klok, H. A. *Chem. Rev.* **2009,** 109, (11), 5437-5527.

34. Zhao, B.; Brittain, W. J. *Prog. Polym. Sci.* **2000,** 25, (5), 677-710.

35. Balazs, A. C.; Singh, C.; Zhulina, E.; Chern, S. S.; Lyatskaya, Y.; Pickett, G. *Prog. Surf. Sci.* **1997,** 55, (3), 181-269.

36. Ruhe, J.; Knoll, N. *J. Macromol. Sci.-Polym. Rev* **2002,** C42, (1), 91-138.

37. Jordan, R.; Ulman, A.; Kang, J. F.; Rafailovich, M. H.; Sokolov, J. *J. Am. Chem. Soc.* **1999,** 121, (5), 1016-1022.

38. Advincula, R.; Zhou, Q. G.; Park, M.; Wang, S. G.; Mays, J.; Sakellariou, G.; Pispas, S.; Hadjichristidis, N. *Langmuir* **2002,** 18, (22), 8672-8684.

39. Advincula, R., Polymer brushes by anionic and cationic Surface-Initiated Polymerization (SIP). In *Surface-Initiated Polymerization I*, Springer-Verlag Berlin: Berlin, **2006**; Vol. 197, pp 107-136.

40. Jordan, R.; Ulman, A. *J. Am. Chem. Soc.* **1998,** 120, (2), 243-247.

41. Zhao, B.; Brittain, W. J. *J. Am. Chem. Soc.* **1999,** 121, (14), 3557-3558.

42. Zhao, B.; Brittain, W. J. *Macromolecules* **2000,** 33, (2), 342-348.

43. Jaworek, T.; Neher, D.; Wegner, G.; Wieringa, R. H.; Schouten, A. J. *Science* **1998,** 279, (5347), 57-60.

44. Kratzmuller, T.; Appelhans, D.; Braun, H. G. *Adv. Mater.* **1999,** 11, (7), 555-558.

45. Husemann, M.; Mecerreyes, D.; Hawker, C. J.; Hedrick, J. L.; Shah, R.; Abbott, N. L. *Angew. Chem.-Int. Edit.* **1999,** 38, (5), 647-649.

46. Huang, X. Y.; Wirth, M. J. *Anal. Chem.* **1997,** 69, (22), 4577-4580.

47. Ejaz, M.; Yamamoto, S.; Ohno, K.; Tsujii, Y.; Fukuda, T. *Macromolecules* **1998,** 31, (17), 5934-5936.

48. Matyjaszewski, K.; Miller, P. J.; Shukla, N.; Immaraporn, B.; Gelman, A.; Luokala, B. B.; Siclovan, T. M.; Kickelbick, G.; Vallant, T.; Hoffmann, H.; Pakula, T. *Macromolecules* **1999,** 32, (26), 8716-8724.

49. Huang, W. X.; Kim, J. B.; Bruening, M. L.; Baker, G. L. *Macromolecules* **2002,** 35, (4), 1175-1179.

50. Feng, W.; Zhu, S. P.; Ishihara, K.; Brash, J. L. *Biointerphases* **2006,** 1, (1), 50-60.

51. Sedjo, R. A.; Mirous, B. K.; Brittain, W. J. *Macromolecules* **2000,** 33, (5), 1492-1493.

52. Pyun, J.; Jia, S. J.; Kowalewski, T.; Patterson, G. D.; Matyjaszewski, K. *Macromolecules* **2003,** 36, (14), 5094-5104.

53. Liu, P.; Tian, J.; Liu, W. M.; Xue, Q. J. *Polym. Int.* **2004,** 53, (2), 127-130.

54. Wang, Y. P.; Pei, X. W.; He, X. Y.; Yuan, K. *Eur. Polym. J.* **2005,** 41, (6), 1326-1332.

55. Mulvihill, M. J.; Rupert, B. L.; He, R. R.; Hochbaum, A.; Arnold, J.; Yang, P. D. *J. Am. Chem. Soc.* **2005,** 127, (46), 16040-16041.

56. Chen, R. X.; Madaughlin, S.; Botton, G.; Zhu, S. P. *Polymer* **2009,** 50, (18), 4293-4298.

57. Li, D. X.; He, Q.; Cui, Y.; Li, J. B. *Chem. Mat.* **2007,** 19, (3), 412-417.

58. Lattuada, M.; Hatton, T. A. *Langmuir* **2007,** 23, (4), 2158-2168.

59. Sun, Y. B.; Ding, X. B.; Zheng, Z. H.; Cheng, X.; Hu, X. H.; Peng, Y. X. *Eur. Polym. J.* **2007,** 43, (3), 762-772.

60. Wang, Y.; Teng, X. W.; Wang, J. S.; Yang, H. *Nano Lett.* **2003,** 3, (6), 789-793.

61. Fan, X. W.; Lin, L. J.; Messersmith, P. B. *Compos. Sci. Technol.* **2006,** 66, (9), 1198-1204.

62. Zhao, H. Y.; Argoti, S. D.; Farrell, B. P.; Shipp, D. A. *J. Polym. Sci. Pol. Chem.* **2004,** 42, (4), 916-924.

63. Zhao, H. Y.; Farrell, B. P.; Shipp, D. A. *Polymer* **2004,** 45, (13), 4473-4481.

64. Behling, R. E.; Williams, B. A.; Staade, B. L.; Wolf, L. M.; Cochran, E. W. *Macromolecules* **2009,** 42, (6), 1867-1872.

65. Matyjaszewski, K. *Controlled/Living Radical Polymerization Progress in ATRP, NMP, and RAFT. ACS Symposium Series* **2000,** 768.

66. Wang, J. S.; Matyjaszewski, K. *Macromolecules* **1995,** 28, (23), 7901-7910.

67. Kotani, Y.; Kato, M.; Kamigaito, M.; Sawamoto, M. *Macromolecules* **1996,** 29, (22), 6979-6982.

68. Ando, T.; Kamigaito, M.; Sawamoto, M. *Tetrahedron* **1997,** 53, (45), 15445-15457.

69. Uegaki, H.; Kamigaito, M.; Sawamoto, M. *J. Polym. Sci. Pol. Chem.* **1999,** 37, (15), 3003-3009.

70. Zhang, X.; Matyjaszewski, K. *Macromolecules* **1999,** 32, (22), 7349-7353.

71. Destarac, M.; Matyjaszewski, K.; Boutevin, B. *Macromol. Chem. Phys.* **2000,** 201, (2), 265-272.

72. Percec, V.; Kim, H. J.; Barboiu, B. *Macromolecules* **1997,** 30, (26), 8526-8528.

73. Brandts, J. A. M.; van de Geijn, P.; van Faassen, E. E.; Boersma, J.; van Koten, G. *J. Organomet. Chem.* **1999,** 584, (2), 246-253.

74. Kotani, Y.; Kamigaito, M.; Sawamoto, M. *Macromolecules* **1999,** 32, (8), 2420-2424.

75. Matyjaszewski, K.; Jo, S. M.; Paik, H. J.; Gaynor, S. G. *Macromolecules* **1997,** 30, (20), 6398-6400.

76. Xia, J.; Zhang, X.; Matyjaszewski, K. *Transition metak catalysis in macromolecular design; ACS symposium series,* **2000,** 760, 207-233.

77. Perrier, S.; Jackson, S. G.; Haddleton, D. M.; Ameduri, B.; Boutevin, B. *Tetrahedron* **2002,** 58, (20), 4053-4059.

78. Shen, J. G.; Hogen-Esch, T. *J. Am. Chem. Soc.* **2008,** 130, (33), 10866-10867.

79. Hvilsted, S.; Borkar, S.; Siesler, H. W.; Jankova, K., Novel fluorinated polymer materials based on 2,3,5,6-tetrafluoro-4-methoxystyrene. In *Advances in Controlled/Living Radical Polymerization*, Matyjaszewski, K., Ed. Amer Chemical Soc: Washington, **2003**; Vol. 854, 236-249.

80. Li, K.; Wu, P. P.; Han, Z. W. *Polymer* **2002,** 43, (14), 4079-4086.

81. Li, X. S.; Gan, L. H.; Gan, Y. Y. *Polymer* **2008,** 49, (7), 1879-1884.

82. Yang, Y. J.; Wang, Z.; Gao, Y.; Liu, T.; Hu, C. P.; Dong, Q. Z. *J. Appl. Polym. Sci.* **2006,** 102, (2), 1146-1151.

83. Joachim, C.; Gimzewski, J. K.; Aviram, A. *Nature* **2000,** 408, (6812), 541-548.

84. Zhao, X. M.; Xia, Y. N.; Whitesides, G. M. *Adv. Mater.* **1996,** 8, (10), 837-&.

85. Kim, E.; Xia, Y. N.; Whitesides, G. M. *Nature* **1995,** 376, (6541), 581-584.

86. Resnick, D. J.; Dauksher, W. J.; Mancini, D.; Nordquist, K. J.; Ainley, E.; Gehoski, K.; Baker, J. H.; Bailey, T. C.; Choi, B. J.; Johnson, S.; Sreenivasan, S. V.; Ekerdt, J. G.; Willson, C. G., High resolution templates for step and flash imprint lithography. In *Emerging Lithographic Technologies Vi, Pts 1 and 2*, Englestad, R. L., Ed. Spie-Int Soc Optical Engineering: Bellingham, 2002; Vol. 4688, 205-213.

87. Chou, S. Y.; Krauss, P. R.; Renstrom, P. J. *Appl. Phys. Lett.* **1995,** 67, (21), 3114-3116.

88. Trau, M.; Yao, N.; Kim, E.; Xia, Y.; Whitesides, G. M.; Aksay, I. A. *Nature* **1997,** 390, (6661), 674-676.

89. Kumar, A.; Biebuyck, H. A.; Whitesides, G. M. *Langmuir* **1994,** 10, (5), 1498-1511.

90. Childs, W. R.; Nuzzo, R. G. *J. Am. Chem. Soc.* **2002,** 124, (45), 13583-13596.

91. Loo, Y. L.; Willett, R. L.; Baldwin, K. W.; Rogers, J. A. *J. Am. Chem. Soc.* **2002,** 124, (26), 7654-7655.

92. Xu, Q. B.; Rioux, R. M.; Dickey, M. D.; Whitesides, G. M. *Accounts Chem. Res.* **2008,** 41, (12), 1566-1577.

93. Gates, B. D.; Xu, Q. B.; Love, J. C.; Wolfe, D. B.; Whitesides, G. M. *Ann. Rev. Mater. Res.* **2004,** 34, 339-372.

94. Studer, D.; Gnaegi, H. *J. Microsc.-Oxf.* **2000,** 197, 94-100.

95. Al-Amoudi, A.; Dubochet, J.; Gnaegi, H.; Luthi, W.; Studer, D. *J. Microsc.-Oxf.* **2003,** 212, 26-33.

96. Al-Amoudi, A.; Studer, D.; Dubochet, J. *J. Struct. Biol.* **2005,** 150, (1), 109-121.

Chapter 2 Research Objectives and Thesis Outline

2.1 Research Objectives

We were aimed to develop new technologies that are capable of modifying polymer surfaces in one step with less expensive facilities. To modify polymer surface chemistry, a surface-active-additive (surfadditive) approach was proposed. This approach is to be integrated with the plastic molding process, in which surfadditive and plastic granule or powder are premixed, and the surfadditive molecules migrate to the surface of the parts during the molding process. Such surfadditives, should have three major components: a functionality providing surface property modification, a manipulable composition driving additive to bulk surface and a compatible segment ensuring permanent surface modification. Since acrylic plastics are one of the mostly used materials in industry, we decided to synthesis methacrylate based surfadditives to prove the concept. To demonstrate this proposal, two types of surfadditives are to be synthesized and characterized:

1. A telechelic copolymer having the head-neck-body structure;
2. A magnetic nanoparticle grafted with functional polymeric brushes.

Besides, the applications of surfadditives in typical molding processes are to be investigated. Effects of surfadditive loading, processing methods and conditions on surface modification are to be studied.

In modifying polymer surface topography, a nonlithographic nanopatterning method based on chattering is proposed. Knowing that chatters are resulted from uncontrolled vibration in unstable cutting, we hypothesize that uniform "chatters" can be produced by conducting vibration cutting with a controlled oscillation source. To testify this, the oscillation diamond knife (DIATOME®) is to be used in a microtome system. Representative polymers, both thermoplastic and thermosetting, are to be tested. Optimal cutting conditions, including cutting speed, oscillation frequency or cutting depth are to be investigated.

2.2 Thesis Outline

This thesis is composed of 8 chapters and one appendix. The first two chapters provide a general introduction of the research background, objective and thesis outline.

Chapter 3, entitled "novel polymeric surfadditives synthesized via atom transfer radical polymerization and their surface migration properties", reports the synthesis and application of block copolymer surfadditives bearing head-neck-body structure. Two types of polymers having similar body structure but different head and neck components were synthesized and applied to injection molding and casting process of acrylic plastic. The effect of surfadditive concentration, molding temperature, molecular structure as well as mold surface on surface modification was studied.

Chapter 4, entitled "Magnetic organo-silica nanoparticles for localized polymer surface modification", consists the synthesis and application of a magnetic surfadditive for polymer surface chemistry modification. Synthesis work includes preparation of initiator grafted iron nanoparticles, surface-initiated ATRP of methacrylated POSS monomer and MMA. Successful synthesis of functional magnetic particles was demonstrated by various characterization methods. The magnetic nanoparticles were incorporated to MMA syrup in a casting process. The effect surface modification with various amounts of surfadditives was demonstrated.

Chapter 5, entitled "Controlled chattering - a new "cutting edge" technology for nanofabrication" is an article published in Nanotechnology, 2010, 21: 355302. This article reports a new nanofabrication method for preparing wavy patterns on polymer surfaces using a microtomy facility. The concept of "controlled chattering" was introduced for the first time. Proof-of-concept results on PMMA were provided, and the size of patterns was successfully controlled from 30nm to micrometer scale. Large-scale uniformity of patterns was demonstrated by diffraction experiments.

Chapter 6, entitled "Controlled Chattering on PMMA and epoxy: effect of crosslinking and cutting speed on pattern formation" is an article to be published in the journal of Polymer. This article reports an in-depth study of controlled chattering technology in terms of crosslinking degree, mechanical properties, and cutting speed. Results on representative thermoplastic and thermosetting polymers (PMMA and epoxy) were compared. A linear relationship between the cutting speed and pattern size were found. The slope of the linear relation was correlated to the compression theory in cutting process.

Chapter 7, entitled "A mechanical approach for the fabrication of polymer and metal nanowires" is an article submitted to the journal of Nanotechnology. This article reports a new method for the fabrication of nanowires based on controlled chattering technology. This method was demonstrated on both polymer and soft metals such as aluminum and copper. Through adjusting cutting depth and wavy phase alignment, nanowires with ribbon-like or rod-like structures were fabricated. The size of nanowires was tunable from sub-100nm to over 1 micrometer by changing cutting depth or speed. The aspect ratio of nanowires fabricated by this method can as high as 10^4.

Chapter 8 summarizes the major contribution of this thesis and provides perspectives for future work on polymer surface engineering.

Appendix A consists an article entitled “Diffusion of semi-flexible polyelectrolyte through nanochannels” which is published in AIChE Journal, 2010, 56(7): 1684-1692. This part of work was conducted in the first year of PhD program, and was aimed to investigate the confined diffusion of sodium polystyrene sulphonate (PSS) molecule through the track-etched polycarbonate membranes using a custom designed diffusion cell. A series of PSS standards diffusing through polycarbonate membranes with different pore sizes in salt-free solutions were studied. A crossover region between free diffusion (3D) and highly confined diffusion (1D) was identified.

Appendix B provides additional TEM images of PMMA and metal nanowires fabricated by controlled chattering.

Chapter 3 Novel Polymeric Surfadditives Synthesized via Atom Transfer Radical Polymerization and Their Surface Migration Properties

This chapter is reproduced based on the article by Gu H. Zhang J. Faucher S. and Zhu S., Novel Polymeric Surfadditives Synthesized via Atom Transfer Radical Polymerization and Their Surface Migration Properties. *Macromolecular Reaction Engineering*, 2011, in press. Copyright © 2011 WILEY-VCH Verlag GmbH & Co. KGaA, Weinheim.

Author contributions: Hongyan Gu performed all the experiments, characterization and manuscript preparation. Dr. Junwei Zhang assisted the injection molding of PMMA samples. Dr. Santiago Faucher participated in some discussion and provided helpful suggestions. Dr. Shiping Zhu supervised this work and participated manuscript revision.

3.1 Abstract

Multi-functional tri-block copolymers having fluorinated and triethoxysilane side chains and polymethacrylate backbone have been synthesized and used as surface-active additives (termed as "surfadditive") in molding and casting acrylic parts. The fluorinated block facilitates migration of surfadditive molecules to the part surface and the acrylate block provides rooting to the part matrix, while the silane block offers functionality to the part surface. This uniquely designed surfadditive allows surface functionalization and modification without post-processing steps. This work reports the design and synthesis of surfadditives and demonstrates their surface enrichment in molding and cell casting of poly(methyl methacrylate) (PMMA) samples. The effects of processing temperature, surfadditive structure and concentration, as well as mold surface property on the surface modification are systematically investigated.

3.2 Introduction

Materials having specific surface properties different from bulk have been of great interest in the recent years. There are many different approaches developed in polymer surface modification for improving adhesion, wettability, biocompatibility, chemical/mechanical resistance, etc. These approaches such as various coatings[1-5], surface radiation by plasma or UV[6-10], surface roughening by chemical/physical treatments[11,12], and surface grafting of functional polymers or monomers[13,14] have been highly developed in the recent decades. However, most of these technologies involve multiple steps in operation and some of them are limited to treat small-sized parts only. In comparison, surface modification by adding low surface energy additives during processing is simple and more flexible[15-17]. Previous studies on the low surface energy additives have been mainly focused on monofunctional polymers, such as fluorinated block copolymer, for the purpose of increasing hydrophobicity of the polymer surfaces[17]. The design and synthesis of multi-functional additives for surface functionalization and modification however have been rarely explored.

In a motivation to develop multi-functional surface-active additives (termed as “surfadditives”) that can be used to modify polymer surface properties in molding and casting, we synthesized and tested telechelic acrylic tri-block copolymers having fluorinated, ethoxysilyl and methacrylic functionalities via atom transfer radical polymerization (ATRP). A surfadditive molecule has a “head-neck-body” structure with its “body” being compatible with the bulk material while “head” and “neck” provide functionalities. Either the “head” or “neck” is required to have a low surface free energy, such as fluorinated segments. Scheme 3.1 shows the schematic design of the surfadditive molecules and their migration processes. The surfadditive must be miscible with bulk materials, however, during molding or casting, the molecules can preferentially migrate/segregate to the surface driven by surface energy difference between the surfadditive and bulk materials.

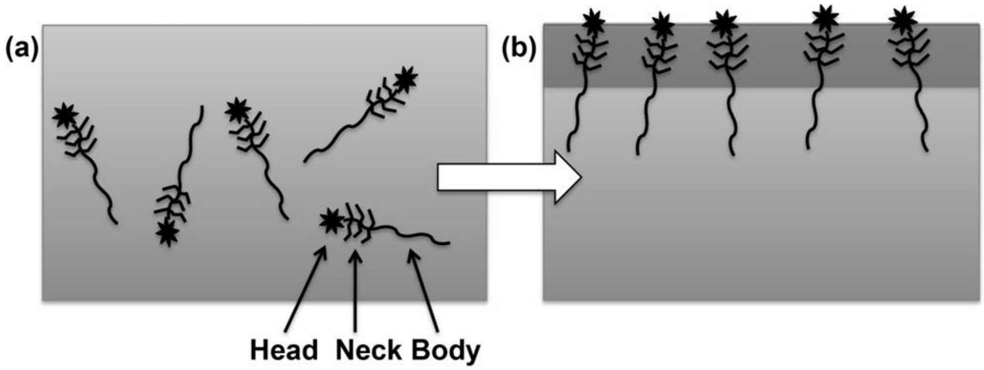

Scheme 3.1 (a) Surfadditive molecules having a “head-neck-body” structure are premixed with the bulk substrate material. (b) The surfadditive molecules migrate to the substrate surface with their “head” or “neck” parts towards the outmost surface and a surfadditive-rich layer is thus formed on the sample surface.

This design of surfadditive requires synthesis of well-controlled tri-block acrylic copolymers. Fortunately, the development of atom transfer radical polymerization (ATRP) has provided a powerful tool for such purpose. It allows for easy control of molecular functionality and sequence with functionalized initiator and/or monomer. For example, fluorinated polymers were synthesized via ATRP from fluorinated monomer or fluorinated initiator with controlled molecule structure[18-21]. Crosslinkable polymers could also be synthesized from acrylic monomers containing pendent trialkoxysilyl groups. In the surface chemistry, hydrolyzed -SiOH groups normally serve as a primer that facilitates successive surface modification. An industrial example is 3-trimethoxysilyl propyl methacrylate (TMSPMA). Well-controlled TMSPMA samples were successfully prepared via ATRP[22, 23]. However, the methoxysilyl group is very sensitive to moisture and it hydrolyzes rapidly in air. Preservation and polymerization of methoxysilyl-containing monomers require a very strict anhydrous condition. In comparison, 3-triethoxy propylmethacrylate (TESPMA) is more stable and the ethoxysilyl group hydrolyzes more slowly than methoxysilyl functionalized chemicals. This stability requirement is essential because the product must remain dormant during molding/casting but can be reactivated under a certain condition later.

In this work, two types of surfadditives containing both fluorocarbon and triethoxysilyl moieties are synthesized in a one-pot process and characterized by various means that include GPC, NMR and DSC. The surface migration property of the surfadditives and the effect of the processing conditions on PMMA surface modification were investigated by water contact angle measurements and EDX analysis.

3.3 Experimental Section

3.3.1 Materials

Table 3.1 summarizes the chemicals used in this work and their specifications.

Table 3.1 List of chemicals and their specifications

Chemicals	Abbrev.	Grade, Supplier	Purpose
toluene[a]		HPLC, Aldrich	solvent, synthesis of initiator Br-MTESP
tetrahydrofuran[a]	THF	HPLC, Aldrich	solvent, synthesis of initiator PFOBMP
trifluorotoluene[a]	TFT	anhydrous, ≥99%, Sigma-Aldrich	solvent, ATRP of TEOSi-FMA-MMA
anisole[a]		Anhydrous, 99.7%, Sigma-Aldrich	solvent, ATRP of PFO-SiMA-MMA
(3-aminopropyl)trimethoxysilane	APTES	97%, Aldrich	reactant, synthesis of initiator Br-MTESP
α-bromoisobutyryl bromide	BiBB	98%, Aldrich	reactant, synthesis of initiator Br-MTESP and PFOBMP
1H,1H-perfluoro-1-nonanol	PFNOL	98%, Exfluor Corp.	reactant, synthesis of initiator PFOBMP
sodium chloride	NaCl	>99%, Caledon laboratories Ltd.	purificant, synthesis of initiator PFOBMP
sodium bicarbonate	$NaHCO_3$	ACS, EMD Chemicals Inc.	purificant, synthesis of initiator PFOBMP
calcium chloride	$CaCl_2$	anhydrous, Fisher Scientific	purificant, synthesis of initiator PFOBMP
pentane		HPLC, ≥99.0%, Sigma-Aldrich	eluent, chromatography of PFOBMP
diethyl ether		HPLC, ≥99.9%, Sigma-Aldrich	eluent, chromatography of PFOBMP
triethylamine	TEA	99.5%, Aldrich	catalyst, synthesis of initiator Br-MTESP and PFOBMP
copper bromide	CuBr	99.999% Aldrich	catalyst, ATRP of both polymers
N,N,N’,N”,N”-pentamethyldiethylenetriamine	PMDETA	99%, Aldrich	ligand, ATRP of both polymers
1H,1H-perfluoro-n-decyl acrylate[b]	PFDA	97%, Exfluor Res. Corp.	monomer 1, ATRP of TEOSi-FMA-MMA
methacryloxypropyl 3-(triethoxysil) propylmethacrylate[b]	TESPMA	99%, Gelest	monomer 1, ATRP of PFO-SiMA-MMA
methyl methacrylate [b]	MMA	99%, Aldrich	monomer 2, ATRP of TEOSi-FMA-MMA and PFO-SiMA-MMA
methanol [a]	methanol	HPLC, Aldrich	precipitator, TEOSi-FMA-MMA purification
dimethyl sulfoxide [a]	DMSO	99.9%, Fisher Scientific	precipitator, PFO-SiMA-MMA purification

[a] Solvents were dried over CaH_2 and distilled under reduced pressure. [b] Inhibitor in monomers was removed by passing monomer through an inhibitor remover column (Aldrich). Monomers were dried using molecular sieves for a few days and stored in freezer under nitrogen protection.

3.3.2 Synthesis of Functionalized ATRP Initiators

The ATRP initiator bearing triethoxy silane moiety: 2-bromo-2-methyl-N-(3-(triethoxysilyl)propyl) propanamide (Br-MTESP,) was synthesized according to reference[24]. The second type of ATRP initiator: (perfluoro-octyl)-2-bromo-2-methyl-propionate (PFOBMP) was synthesized as follows: 5.55 g TEA (55 mmol) and 22.5 g 1H,1H-perfluoro-1-nonanol (PFNOL, 50 mmol) and 120 ml THF were well mixed in a round bottom flask immersed in an ice bath. BiBB of 12.8 g (56 mmol) diluted with 20ml THF was then added dropwisely to the stirred solution through a funnel. The reaction was carried out in an ice bath for 3 hours, and then at room temperature for another 18 hours. THF in the resultant mixture was then evaporated using a rotary evaporator. Subsequently, the mixture was diluted with 300 ml of ethyl acetate and was washed with 200 ml de-ionized (DI) water, 200 ml $NaHCO_3$ solution (0.02 mol/L), 200 ml NaCl solution (0.02 mol/L) and finally with 200 ml DI water twice. The top layer of the liquid was collected and dried with anhydrous $CaCl_2$. After 24 hours, the mixture was filtered to remove $CaCl_2$ and was then rotary evaporated to remove ethyl acetate. The crude yield of this reaction was about 75%. The resultant product was further purified with a chromatography column. The column was built with 60 Å silica gel, pentane/diethyl ether (1/9) was used as eluent.

3.3.3 Synthesis of TEOSi-FMA-MMA Block Copolymer

A typical procedure for the synthesis of TEOSi-FMA-MMA in one pot is shown in Scheme 3.2. (1) 28.62 mg CuBr (0.2 mmol), 35 mg PMDETA (0.2 mmol), 4.68 g PFDA (10 mmol) and 5ml anhydrous TFT were mixed in a 50 ml three-neck flask with vigorous stirring. One of the necks was connected to a condenser to reflux the evaporated solvent. The other two necks were sealed with rubber septums, and were used for feeding and nitrogen purging. (2) 0.37 g Br-MTESP (1 mmol) and 5ml of TFT were mixed in a 10 ml pear-shaped flask. Both mixtures were deoxygenated through five vacuum-refill cycles of nitrogen, and bubbled with nitrogen for another 30 min. (3) The mixture in 50 ml three-neck flask was placed into an oil bath preheated to 90˚C. The polymerization started with an injection of Br-MTESP/TFT solution through the rubber septum. (4) After 45 minutes, 10.5 ml deoxygenated MMA was injected into the 50 ml flask. The reaction was carried out for another 3 hours under nitrogen protection. (5) Finally, the polymer mixture was stopped by exposure to air. Polymer was precipitated in anhydrous cold methanol, filtered and was repeated for three times to remove excess monomer, solvent and copper. The purified polymer was dried in a vacuum oven at 40˚C overnight.

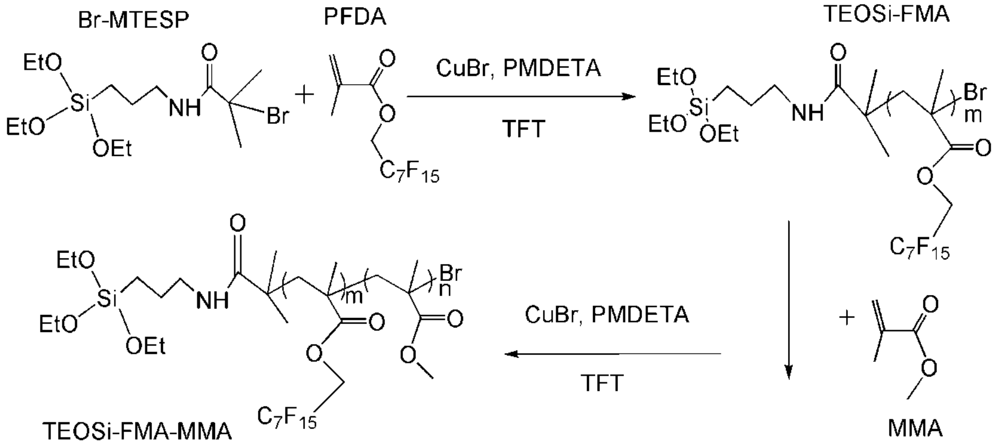

Scheme 3.2 One-pot synthesis of TEOSi-FMA-MMA block copolymer via ATRP in TFT using Br-MTESP as the initiator, PFDA as first monomer and MMA as the second monomer.

3.3.4 Synthesis of PFO-SiMA-MMA Block Copolymer

The synthesis of PFO-SiMA-MMA as shown in Scheme 3.3 was conducted in the following procedure: (1) 28.7 mg CuBr (2 mmol), 34.7 mg PMDETA (2 mmol), 5.8 g TESPMA (10 mmol) and 5 ml anhydrous anisole were added into in a 50 ml three-neck flask containing a magnetic stirrer bar. The flask was deoxygenated through five vacuum-refilling cycles of nitrogen and bubbled with nitrogen for another 30 min before reaction. (2) 1.20 g PFOBMP (1 mmol) was dissolved in 5ml anhydrous anisole in another container and the mixture was deoxygenated in a similar procedure. (3) The 50 ml flask was then placed into an oil bath preheated to 90˚C. A condenser was attached to the top of the reactor to circumfluence solvent and monomer. The polymerization started when

PFOBMP/anisole solution was transferred into the flask through a double-tipped needle purged by nitrogen. The mixture was stirred vigorously and was protected with continuous nitrogen flow all through the reaction. (4) After 150 minutes of polymerization, 10.5 ml MMA was transferred to the flask through a double-tipped needle similar to the procedure in (3). (5) After 18 hours, the polymerization was stopped by exposure to air. The polymer was precipitated in DMSO for three times to get rid of monomer and ligands. It was then diluted in THF and filtered through basic alumina to remove copper. The final product was obtained by vacuum dry under 80˚C overnight.

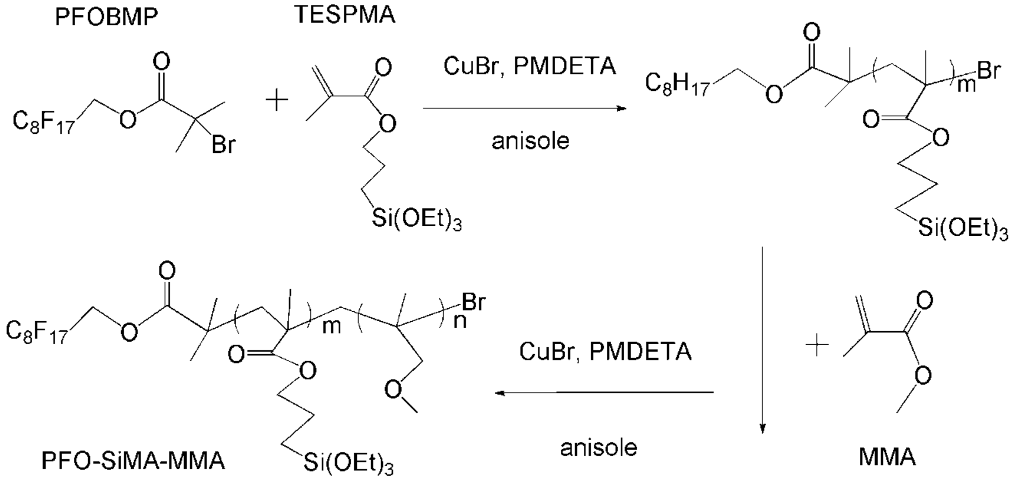

Scheme 3.3 One-pot synthesis of PFO-SiMA-MMA block copolymer via ATRP in anisole using PFOBMP as the initiator, TESPMA as the first monomer and MMA as the second monomer.

3.3.5 Preparation of Parts by Injection Molding

A desired amount of surfadditive was mixed with PMMA powder (Mw: 350,000 g/mol, Aldrich) inside a laboratory mixing molder (Atlas LMM) at temperatures from 140 to 220˚C. The mixture was sufficiently mixed with a rotating screw operated at 100 rpm. After a certain period of mixing, the screw was then pushed forward so that the sample melt was extruded and injected into an aluminum mold to form a $40 \times 15 \times 3$ mm ($L \times W \times D$) part. The polymer together with the mold was then air cooled to room temperature and released from the mold.

3.3.6 Preparation of Parts by Cell Casting

A desired amount of surfadditive was mixed with MMA/PMMA solution containing 10wt% of PMMA (Mw: 350,000 g/mol, Aldrich) in MMA and 0.1wt% of BPO. The addition of PMMA was to obtain a proper solution viscosity for casting. The mixture of 4ml was injected into a glass mold. The chamber size was 50 mm in diameter and 2mm in thickness. The mixture was allowed to polymerize for 8 hours at 60˚C and another 4 hours at 120˚C. In the experiments of studying the effect of mold surface on surfadditive migration, the inner surface of glass mold was covered with an FEP thin film (0.0035” thick, McMaster-Carr).

3.3.7 Characterization Methods

3.3.7.1 Molecular Weight

The relative number-average molecular weight (M_n) and polydipersity index (PDI) of the polymers were measured by gel permeation chromatography (GPC, Waters). DMF was used as eluent because it dissolved fluorinated oligomer better than THF. The flow rate of DMF was 0.5 ml/min. The calibration range was 700 to 35,000 g/mol based on PMMA standards.

3.3.7.2 Nuclear Magnetic Resonance Spectrum

^{1}H-NMR spectra were conducted on a Bruker AV200 NMR instrument. Most samples were tested using $CDCl_3$ as solvent. However, the fluorinated oligomer obtained from Br-MTESP initiated PFDA polymerization in the synthesis of TEOSi-FMA-MMA was not soluble in regular deuterated solvents. ^{1}H-NMR spectrum of oligomer was obtained in a mixed solvent of TFT and $CDCl_3$.

3.3.7.3 Differential Scanning Calorimetry (DSC) Measurements

The glass transition temperatures (T_g) of the polymer samples were measured in a differential scanning calorimetry (DSC Q200, TA instrument). Two heating cycles from 0˚C to 300˚C at a heating and cooling rate of 15˚C/min were used. The glass transition temperature was estimated based on the intersection of two tangents at the start of the corresponding endotherm in the second heating cycle.

3.3.7.4 Water Contact Angle (WCA) Measurement

The WCA of the molded or casted parts were measured by a standard goniometer (Ramé-hart instrument Co.) at room temperature (22˚C). The reported water contact angle values were the average of 15 measurements in 15 seconds. Each sample was measured for 6 times at different locations to estimate the standard deviation.

3.3.7.5 Energy Dispersive X-ray (EDX) Spectroscopy

The EDX measurements were conducted on a Tescan Vega II LSU scanning electron microscope (Tescan USA, PA) facility with X-Max 80 detector (Oxford Instruments, MA). The accelerate voltage was set to 5 kV. Six-to-ten spots were taken and analyzed in each measurement to obtain the standard deviation of the elemental data.

3.4 Results and Discussion

3.4.1 Synthesis of Surfadditives

Successful ATRP of fluorinated acrylate/methacrylate monomers has been reported in literatures using TFT as solvent, CuBr as catalyst and PMDETA as ligand[25, 26]. In the synthesis of TEOSi-FMA-MMA block copolymers, the initial molar ratio of the initiator Br-MTESP as the “head” to monomer 1H,1H-perfluoro-n-decyl acrylate (PFDA) was 1:10. ^{1}H NMR spectra of Br-MTESP, PFDA and the reaction mixture after 45 min polymerization were shown in Figure 3.1(A), (B) and (C). The presence of the peaks at 2.0-1.8 ppm and the precipitated polymer confirmed the formation of fluorinated oligomers[27]. By comparing the peak areas of the resonance at 4.6 ppm (C_7F_{15}-CH_2-O- protons of the monomer and polymer) with those at 6.1 and 5.4 ppm (CH_2=$C(CH_3)$ olefinic protons in the monomer), the PFDA conversion can be estimated from $[A_{4.6}-(A_{6.1}+A_{5.4})]/A_{4.6}\times100\%$. The conversion of PFDA reached 25% after 45 min of reaction. That is, there were 2.5 monomer units in average incorporated into the “neck” of each polymer chain. In the second step of polymerization, deoxygenized MMA as the “body” (MMA: initiator=100:1 in mole) was injected to the reactor. The conversion of MMA reached 30% based on gravimetry measurement after 3 hours of polymerization. Since MMA is much more reactive than fluorinated methacrylate in copolymerization [28] and the molar ratio of MMA to PFDA is 100:7.5, PFDA copolymerized in the second step can be neglected. Based on the conversion data, the molecular weight of TEOSi-FMA-MMA was estimated to be 4,500 g/mol from $MW = MW_{Br\text{-}MTESP} + MW_{PFDA}\times2.5 + MW_{MMA}\times30$. Table 3.2 summarizes the ATRP of TEOSi-FMA-MMA.

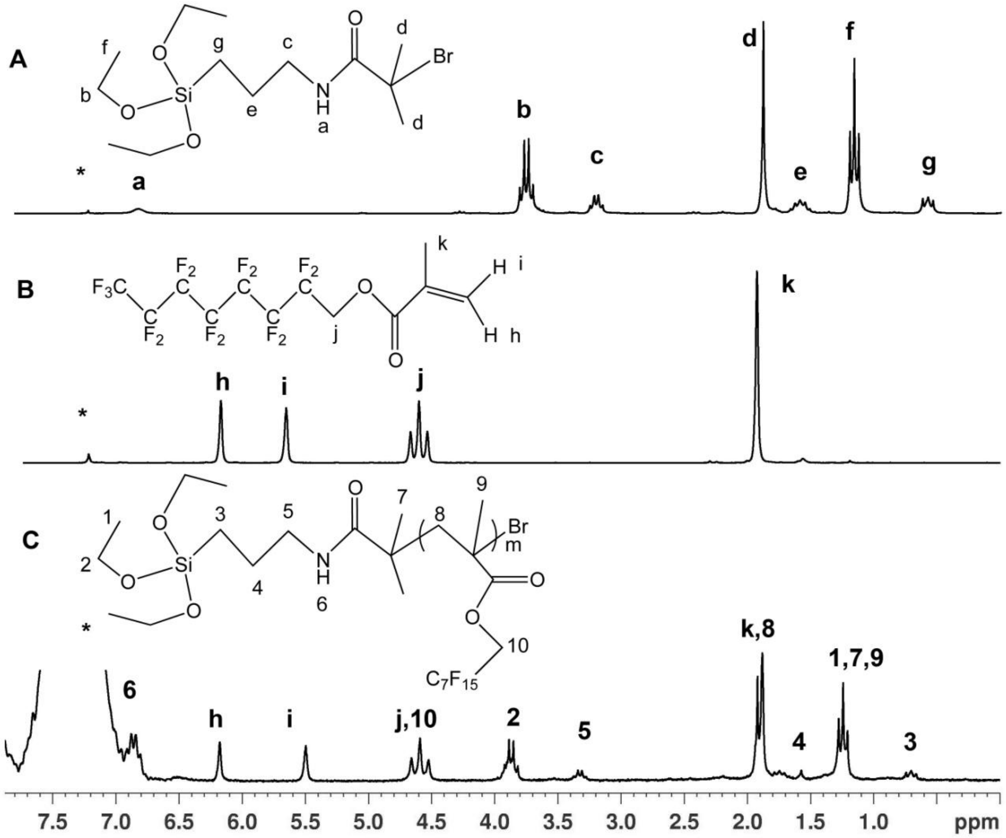

Figure 3.1 ^{1}H NMR spectra of (A) Br-MTESP (initiator) in $CDCl_3$, (B) PFDA (monomer) in $CDCl_3$ and (C) the reaction mixture of TEOSi-FMA (oligomer) and PFDA (monomer) in TFT and $CDCl_3$. The signals marked by "*" are assigned to solvents.

Table 3.2 ATRP recipe and results of TEOSi-FMA-PMMA and PFO-SiMA-PMMA

Polymer	**[I][a]/[M1] /[MMA]**	**M1 conv. (%)[b]**	**MMA Conv. (%)[c]**	**MW_{Theo}[d]. g/mol**	**$M_{n,GPC.}$ (g/mol)/PDI**	**F count (n/chain)**	**Si count (n/chain)**
TEOSi-FMA-PMMA	1:10:100	25 (PFDA)	30	4,500	5,500/1.8	37.5	1
PFO-SiMA-PMMA	1:10:100	85 (TESPMA)	29	6,000	6,700/1.6	17	8.5

[a] Initiator was Br-MTESP for TEOSi-FMA-PMMA and PFOBMP for PFO-SiMA-MMA.

[b] Conversion data were estimated from ^{1}H NMR spectra.

[c] Conversion data were obtained using gravimetric method.

[d] Theoretical molecular weight was calculated based on NMR results.

Similarly, PFO-SiMA-MMA was synthesized in one-pot with PFOBMP as initiator (“head”), methacryloxypropyl 3-(triethoxysil) propylmethacrylate (TESPMA) (“neck”) and MMA (“body”) as the first and second monomer. Anisole was chosen as solvent because it was a better solvent for the fluorinated oligomer (PFO-SiMA) than other nonpolar solvents. Successful ATRP of TESPMA in anisole mediated by CuBr/PMDETA was reported elsewhere[29]. The initial molar ratio of the initiator PFOBMP to the monomer TESPMA was 1:10 (Table 3.2). ^{1}H NMR spectra of PFOBMP, TESPMA and the reaction mixture after 150 min of polymerization are shown in Figure 3.2(A), (B) and (C). The

TESPMA conversion was obtained from the integrated areas for olefinic $CH_2=C(CH_3)$-protons (0.61 and 0.55 ppm) for TESPMA as compared with the peak area of $–CH_2$-Si- in TESPMA and oligomer at 0.6-0.7 ppm. The conversion reached 85% in 150 min. That is, 8.5 monomer units were incorporated into each chain as the “neck” prior to the addition of MMA. In the second step of polymerization, deoxygenated MMA of 100 to 1 based on the initiator was added for the chain extension. The second step of polymerization was carried out for 18 hours at 90˚C, and the MMA conversion was measured 29% gravimetrically (29 PMMA units). The molecular weight of PFO-SiMA-MMA block copolymer was estimated 6,000 g/mol from $MW_2 = MW_{PFOBMP} + MW_{TESPMA} \times 8.5 + MW_{MMA} \times 29$ (Table 3.2).

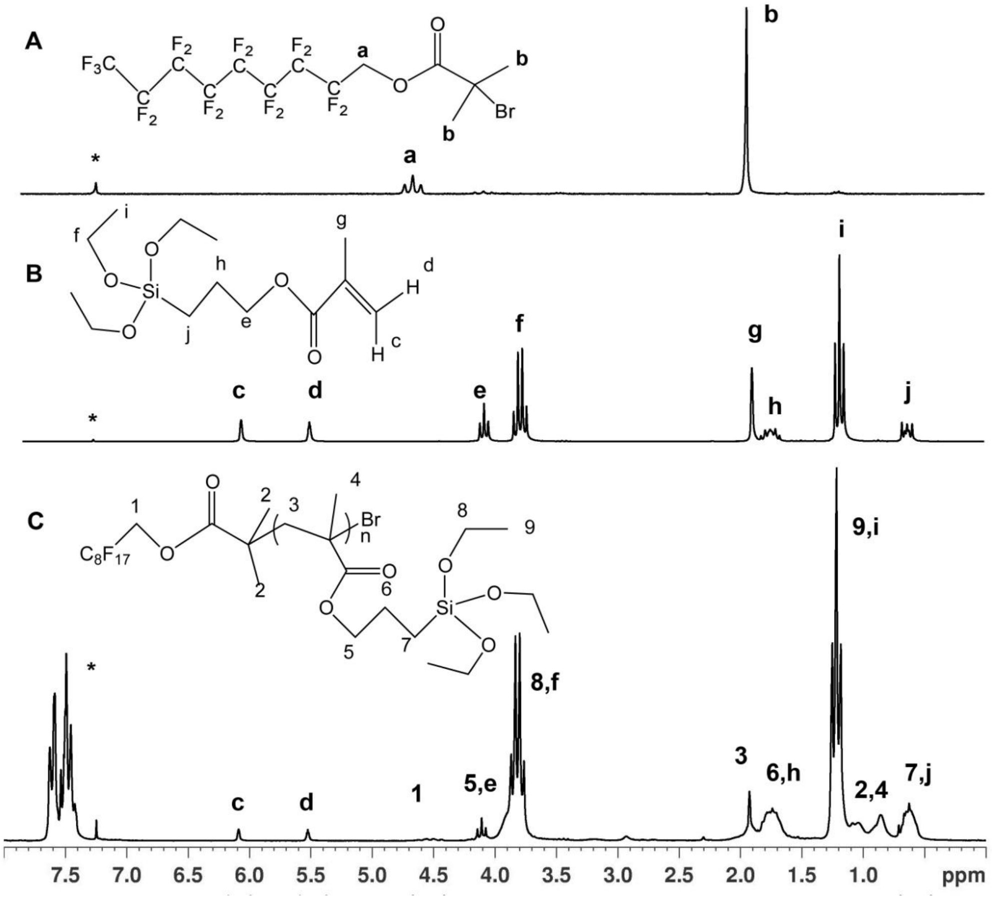

Figure 3.2 ^{1}H NMR spectra of (A) PFOBMP (initiator) in $CDCl_3$, (B) TESPMA (monomer) in $CDCl_3$ and (C) the reaction mixture of PFO-SiMA (oligomer) and TESPMA (monomer) in anisole and $CDCl_3$. The signals marked by “*” are assigned to solvents.

3.4.1 Characterization of Surfadditives

Figure 3.3 gives the GPC elution curves of oligomers and surfadditive polymers in DMF. It was not possible for us to measure the molecular weight of the TEOSi-FMA (the first block of oligomer obtained in the synthesis of TEOSi-FMA-MMA), since its solubility in regular non-fluorinated solvent was very poor. However, the first block of oligomer in the synthesis of PFO-SiMA-MMA (shown as PFO-SiMA) was soluble in DMF and the relative molecular weight from PMMA-calibrated GPC was about 2,400 g/mol. A PDI of 1.4 suggested that the polymerization of TESPMA initiated by PFOBMP followed a controlled radical polymerization mechanism. The molecular weights of TEOSi-FMA-MMA and PFO-SiMA-MMA obtained were 5,500 g/mol and 6,700g/mol, which were slightly larger than those estimated from the NMR and gravimetric results (Table 3.2). The PDI of TEOSi-FMA-MMA and PFO-SiMA-MMA were 1.6 and 1.8, respectively, indicating good control in the one-pot synthesis of block copolymers mediated by copper(I) bromide/PMDETA (please note that short chains normally have much higher polydispersity than long chains and the polydispersity decreases with chain length in controlled/living radical polymerization).

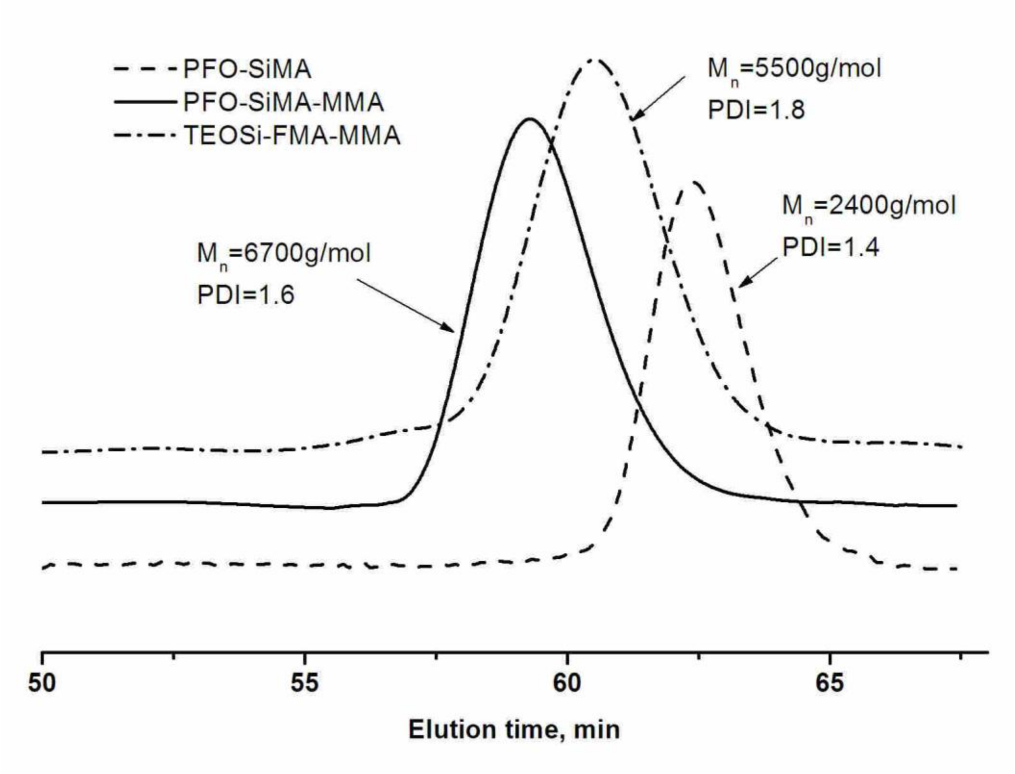

Figure 3.3 GPC elution curves of PFO-SiMA, PFO-SiMA-MMA and TEOSi-FMA-MMA using DMF as eluent.

The thermal properties of raw PMMA powder and the surfadditives were studied by DSC at a heating rate of 15˚C/min. Figure 3.4 shows that the T_g of PMMA bulk material (MW: 350,000 g/mol) was 128˚C, while those of TEOSi-FMA-MMA and PFO-SiMA-MMA were 112 ˚C and 86 ˚C, respectively. It is well known that the T_g of PMMA prepared by free radical polymerization is about 105 ˚C. However, it has also been reported that using different initiators, PMMA samples prepared from free radical polymerization could have their T_g value varied from 104˚C to 128˚C [30]. The differences of T_g between TEOSi-FMA-

MMA and PFO-SiMA-MMA and PMMA bulk materials suggested the effect of fluorinated and siloxane blocks on the PMMA thermal properties. However the different Tg's between TEOSi-FMA-MMA and PFO-SiMA-MMA merely indicated different effects of fluorinated and siloxane blocks on the PMMA thermal properties, which could also be attributed to the sequence of functional structures (e.g. the fluorinated moiety was in the PFO-SiMA-MMA chain end while it was in the TEOSi-FMA-MMA side chain). It should be pointed out that this comparison between the T_gs of the surfadditives and that of the bulk PMMA demonstrated that the surfadditives could be applied to the exiting molding processes of PMMA without alternating operation temperature (i.e., the Tg of both surfadditives are lower that of PMMA).

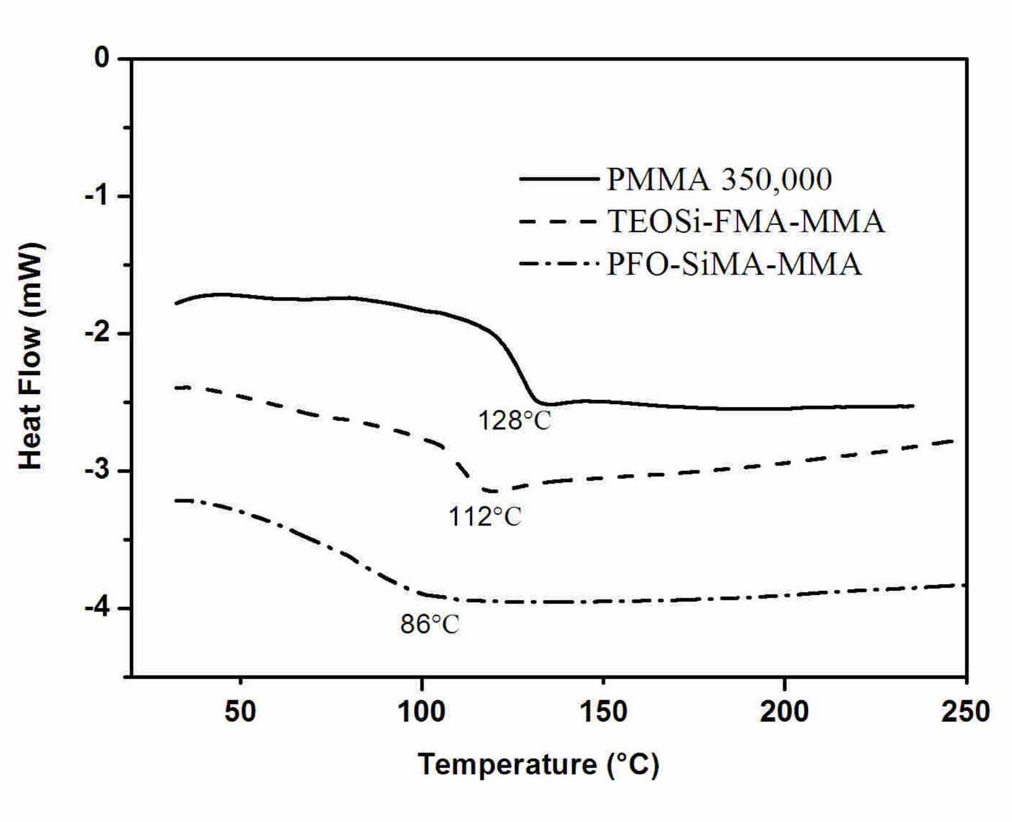

Figure 3.4 DSC measurements of three polymer samples carried out at 15˚C/min heating rate. The solid curve is PMMA having molecular weight 350,000 g/mol. The dashed and dash-dotted curves are TEOSi-FMA-MMA and PFO-SiMA-MMA, respectively.

3.4.2 Effect of Processing Temperature on Surface Modification

For thermoplastic materials, extrusion and injection molding are the most widely used processes in industry for manufacturing small to medium sized parts.

In the injection molding experiments of PMMA, various amounts of surfadditives were pre-mixed with PMMA in a mini-mixing molder (ATLAS LMM) at the molten state. After injected into the mold, the surfadditive molecules started to migrate from the melt to surface, as the surface energy of the fluorinated molecule was much lower[31,32]. A typical industrial injection molding process takes less than one minute for a single injection cycle[33]. However, in this study, the injected mold was hold for an extra hour with heating to enhance migration of the surfadditive molecules. The effects of processing temperature and surfadditive concentration on the part surface properties were examined.

The PMMA parts with TEOSi-FMA-MMA as additive were molded at different temperatures from 140˚ to 220˚, all above their transition temperatures. The injection mold was made of aluminum and the inner surface was polished for smooth part surface. The wettability of the PMMA parts was studied by water contact angle (WCA) measurements. Figure 3.5 shows that the WCA's of the control samples of PMMA and TEOSi-FMA-MMA molded at 180˚C were 80˚ and 108˚, respectively. The incorporation of 1wt% TEOSi-FMA-MMA into MMA resulted in an increase of WCA from 80˚ to over 95˚. The migration of the surfadditive molecules in the melt was dependent on viscosity of the system. Increasing temperature resulted in lower viscosity and thus facilitated the migration. The optimal processing temperature for molding PMMA with TEOSi-FMA-MMA was found to be about 180˚C. Further increase of temperature did not change the WCA much. The significant increase of WCA of these samples confirmed that the PMMA part surfaces were enriched with the fluorinated surfadditive molecules.

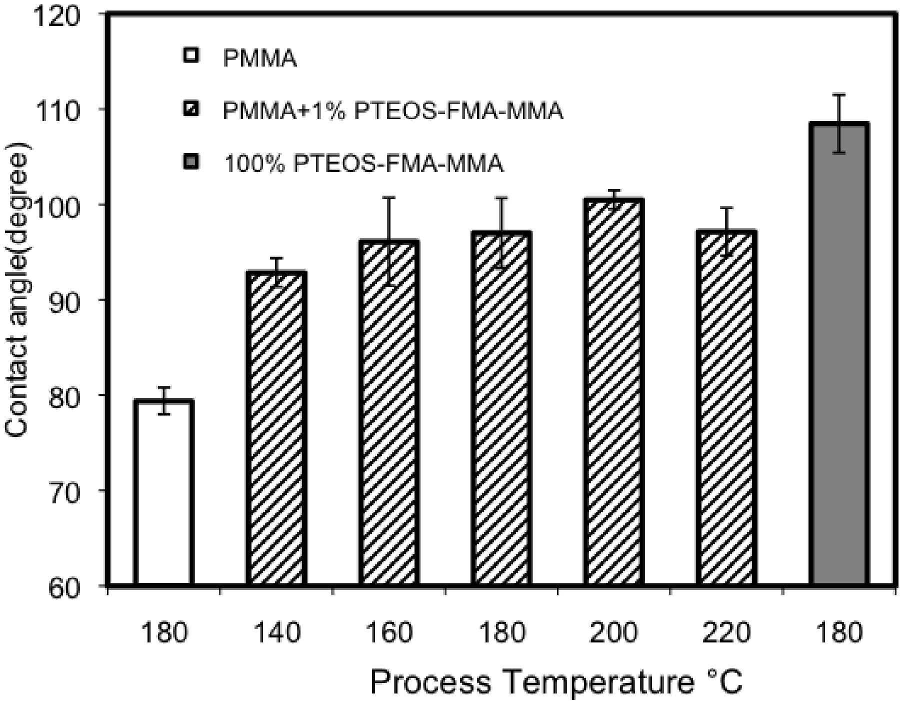

Figure 3.5 Water contact angle of the PMMA parts molded with TEOSi-FMA-MMA at different temperatures. The pure PMMA and TEOSi-FMA-MMA control samples were processed at 180˚C.

3.4.3 Effect of Surfadditive Concentration on PMMA Surface Modification

The effect of surfadditive concentration on the surface property was also studied by adding different amount of TEOSi-FMA-MMA into PMMA raw materials. Figure 3.6 gives the WCA data of the PMMA parts containing 1 to 5wt% of TEOSi-FMA-MMA molded at 180˚C for 1 hour. As the surfadditive concentration increased from 0 to 5%, the WCA increased from 78° to 105°. For a thin film fabricated from the pure surfadditive, the WCA was 110°. It becomes clear that the surface coverage of surfadditive was not complete. Ideally, if the time for the surfadditive migration was sufficient, the part surfaces should be fully covered by the surfadditive molecules for the lowest surface energy. However, in this work, as shown in Figure 3.6, adding 1% surfadditive increased the WCA of PMMA from 78° to 96°. Further increase of the concentration resulted in only a mild increase in the WCA.

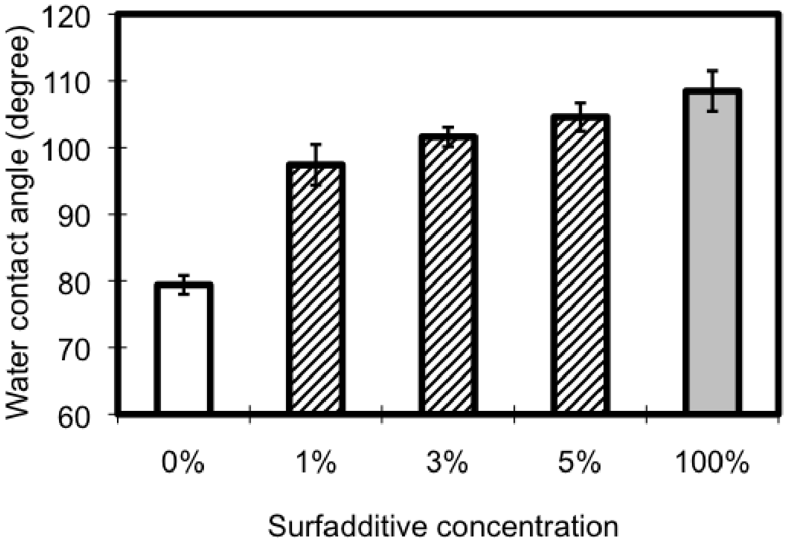

Figure 3.6 Effect of TEOSi-FMA-MMA concentration on water contact angle of the parts molded at 180˚C.

For a 2-3mm thick part, the amount of surfadditive required for a mono-layer surface was estimated to be $<10^{-3}$ % of the total weight. The surfadditive amount used in this work was about 3 orders of magnitude higher, suggesting the presence of surfadditive molecules in the bulk matrix. In the other extreme case, if the surfadditive molecules were homogenously distributed in the bulk (i.e., no migration), its concentration on the surface region should be the same as in the bulk. However, this was not the case, either. The time scale in molding the parts might be a factor that limited the migration of surfadditive molecules to surface. The diffusion coefficient of such surfadditive molecules in the PMMA melt was estimated to be in the order of 10^{-12} -10^{-14} cm^2/s, depending on the melt viscosity [34]. A time scale of 1 hour was not adequate for surfadditive migration through a 3 mm thick film. However, most industrial injection molding processes take only a few seconds or minutes to finish. Therefore, an enhanced post-treatment process to facilitate sufficient surface migration of the surfadditive molecules becomes necessary.

3.4.4 Effect of Mold Surface on Surface Modification

In addition, we also evaluated the surfadditive approach for casting processes that often involve much longer time than injection molding. Generally, the casting processes have advantages in producing thick acrylic boards. The major difference between casting (both cell casting and continuous casting) and other processes lies in their operation pressure and raw materials. In extrusion and injection molding, the raw materials are usually powders or pellets. The melt viscosity in mold is high[35]. In contrast, the raw materials for cell casting are liquid resins, such as monomers, syrups or low molecular weight thermosets, which have much lower viscosities than polymer melts. The viscosity increases during casting, particularly in the late stage, and the overall time scale is usually about 5 to 20 hours [20, 31].

In the cell casting experiments, we used two types of molds, i.e., bare glass molds and fluorinated ethylene propylene (FEP) covered glass molds. We chose FEP instead of PTFE for smooth surfaces to minimize the effect of surface roughness on the WCA measurements. Figure 3.7 shows the WCA data of PMMA parts casted from the different molds with 1 wt% surfadditive addition. The FEP molds always gave higher WCA than the glass counterparts. For the control samples of pure PMMA, the difference between the two molds was about 10°. This difference could be attributed to a surface roughness effect. We measured the mold surface roughness by a profilometer, where the glass mold was 30 nm and the FEP mold was about 450 nm. The difference between the parts containing 1wt% of TEOSi-FMA-MMA was increased to 24°. The difference between the parts containing 1wt% of PFO-SiMA-MMA reached 45^{o} with 110° from FEP molds and 65° from glass molds. The data clearly demonstrated the strong effect of the surfadditive addition on the PMMA part surface properties. However, this surfadditive effect must be introduced by an appropriate mold surface. The mold surface determined if the "head" or "neck" of the surfadditive molecule came to the very top layer of the part surface. The fluorinated block clearly favored the FEP mold.

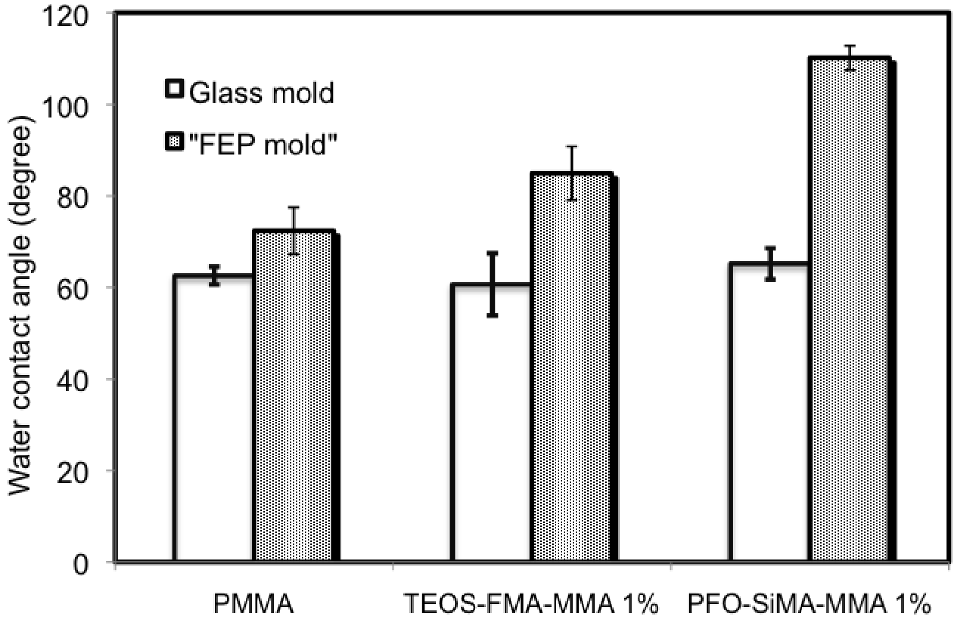

Figure 3.7 WCA results of PMMA parts containing 1% surfadditive cell casted from glass and FEP molds.

The WCA's of the parts casted from the glass molds were similar regardless of the surfadditive type. However, those from the FEP molds were very different with the different surfadditives. The parts with PFO-SiMA-MMA gave much larger WCA's than with TEOSi-FMA-MMA. This could be attributed to the different molecular structure of PFO-SiMA-MMA and TEOSi-FMA-MMA, as the former has a fluorinated "head" and the later has a fluorinated "neck". It was reported that different sequence of fluorinated block in a polymer chain could affect the surface properties differently[36] and the end-caped fluorinated structure showed better efficiency in surface modification[19]. From this point of view, PFO-SiMA-MMA should be more favorable for achieving high surface modification efficiency.

Furthermore, Sugiyama and coworkers found that the number of fluorine atoms also affected the surface migration and more fluorinated segments resulted in larger surface coverage[33]. In our work, PFO-SiMA-MMA had 8 fluorocarbons (17 fluorine atoms) on the "head", while TEOSi-FMA-MMA had about doubled fluorine content (about 17.5 fluorocarbons, 37 fluorine atoms) on the "neck". However, the WCA results indicated that the former was more effective than the latter in migrating to the outmost surface of the parts, particularly when FEP molds were used for casting. Overall, there are many factors (e.g. monomer sequence, fluorocarbon number, and total polymer molecular weight) affecting the surface migration process. For the purpose of introducing reactive species onto polymer surface, an ideal design is that fluorinated "neck" drives surfadditive molecules to surface while silane "head" provides surface functionality and modification.

3.4.5 Elemental Analysis of the Surfadditive Modified Polymer Surface

The part surfaces prepared in this work were further analyzed by an energy-dispersive X-ray (EDX) spectroscopy. Figure 3.8 shows the atomic weight compositions of fluorine and silicon in the modified PMMA composites prepared in glass and FEP molds. The overall fluorine and silicon contents in the pure surfadditive were generally consistent with those estimated from the monomer conversion data shown in Table 3.1. In the synthesis of TEOSi-FMA-MMA, the conversion of PFDA (10:1 molar ratio to initiator) was about 25% while that of MMA (100:1 molar ratio to initiator) was about 30%. Therefore, the theoretical contents of fluorine and silicon should be about 15.7 wt% and 0.62wt%, respectively. The EDX measurements gave 13.92% of fluorine and 0.29% of silicon. It should be noted that the error in EDX measurements became significant at such a low Si content. On the other hand, for PFO-SiMA-MMA, the theoretic weight percentages of fluorine and silicon were about 5.4% and 4.0% while the EDX gave 6.7% and 3.7%, respectively. The EDX experimental data agreed well with the theoretical values.

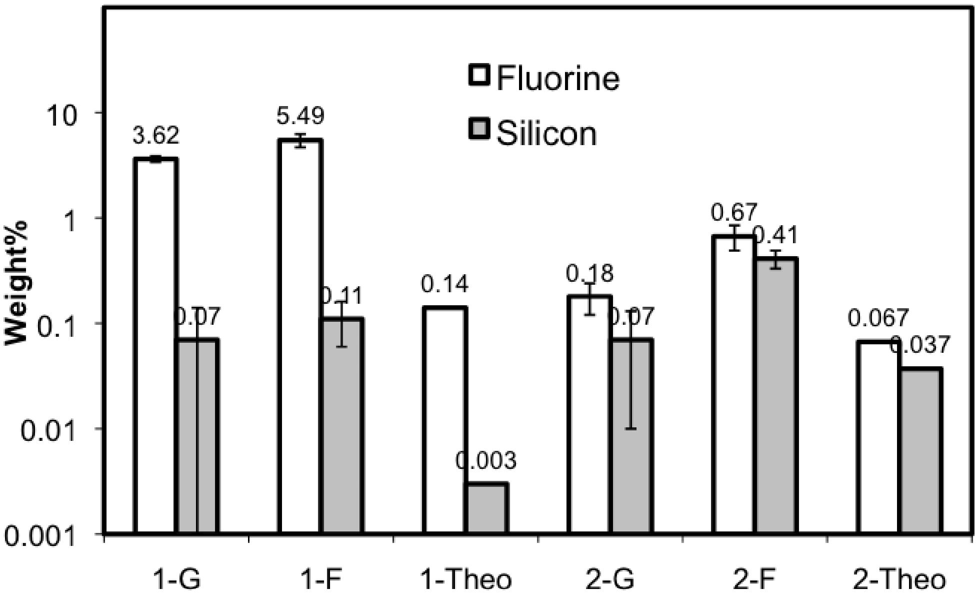

Figure 3.8 Weight percent of fluorine and silicon (in log scale) at the surface of PMMA parts containing 1wt% of surfadditive measured by EDX at 5kV. 1-G and 1-F represent the parts containing 1wt% of TEOSi-FMA-MMA casted from glass and FEP molds respectively. 2-G and 2-F represent the parts containing 1wt% of PFO-SiMA-MMA cased from glass and FEP molds, respectively. 1-Theo and 2-Theo are the estimated values of fluorine and silicon assuming a homogeneous distribution of surfadditive molecules in the PMMA bulk.

If the 1wt% surfadditive was homogeneously dispersed in the PMMA bulk, the atomic contents of fluorine and silicon would be 1% of their respective amounts in the surfadditive. That is, the theoretical fluorine and silicon contents in the casted parts containing 1 wt% TEOSi-FMA-MMA would be 0.14 wt% and

0.003wt% (denoted 1-Theo in Figure 3.8) and those with 1wt% PFO-SiMA-MMA were 0.07wt% and 0.04wt% (denoted 2-Theo in Figure 3.8). In all the parts casted either from glass molds or FEP molds, the fluorine and silicon contents in the surface layer (note: the layer thickness was about 400 nm at 5kV accelerate energy) were significantly higher than their theoretical values of a homogenous dispersion. When 1 wt% TEOSi-FMA-MMA was used, the fluorine at the part surface casted from FEP mold was 38 times more concentrated than its homogeneous dispersion. When 1 wt% PFO-SiMA-MMA was used, the fluorine concentration at the surface was increased about 10 times.

It should be noted that in the water contact angle measurement, the WCA of PFO-SiMA-MMA modified sample was higher than that of TEOSi-FMA-MMA counterpart at the same loading. The WCA data reflected difference in the chemical composition at the very surface of the part, while the EDX data gave an average composition in a 400 nm-thick layer. In other words, the migration of PFO-SiMA-MMA to the top layer was less than that of TEOSi-FMA-SiMA, but there were more fluorocarbons exposed to the outmost surface in the former case because of the “head” fluorocarbons. The EDX results also showed that, for the parts containing 1% surfadditive, the surface enrichment of fluorine and silicon was also strongly affected by the mold surface. The enrichment was much more significant with FEP molds than with glass molds. The FEP molds appeared to be favored in bringing the fluorinated surfadditive molecules to the surface.

3.5 Conclusions

In this work, we reported the design and synthesis of a novel type of surface-active additives (termed as "surfadditives") for the purposes of surface functionalization and modification of polymeric materials. These surfadditive molecules were tri-block copolymers synthesized via atom transfer radical polymerization (ATRP) in one pot and were assumed a "head-neck-body" structure. The "head" (or "neck") was a fluorinated block that facilitated migration of the surfadditive molecules to part surface due to its low surface free energy. The "neck" (or "head") was a triethoxysilyl block that could provide functionality for further surface modification or enhanced adhesion to coated layer. The "body" was a PMMA block that provided rooting for the part matrix materials. It was demonstrated that adding a small amount of the surfadditive significantly changed the surface property of the injection molded and cell casted PMMA parts. This approach of surface modification is advantageous over other methods such since it requires no extra post-processing operations. The surfadditive molecules are added to an initial recipe and migrate to the part surface during molding or casting. The surface enrichment of the surfadditives was confirmed by water contact angle measurements and EDX elemental analysis. The migration of surfadditives in polymer melts was found to be too slow for a typical injection molding process. The cell casting process was favored for the surfadditive migration. It was found that the sequence of the blocks, the number of fluorine atoms in the chain, and the surface property of the mold all played important roles in the surface enrichment of surfadditives.

3.6 References

1. Schulz, U. *Appl. Optics* **2006,** 45, (7), 1608-1618.
2. Haas, K. H. *Adv. Eng. Mater.* **2000,** 2, (9), 571-582.
3. Malinauskas, A. *Polymer* **2001,** 42, (9), 3957-3972.
4. Schulz, U.; Kaiser, N. *Prog. Surf. Sci.* **2006,** 81, (8-9), 387-401.
5. Lahann, J. *Chem. Eng. Commun.* **2006,** 193, (11), 1457-1468.
6. Wagner, H. E.; Brandenburg, R.; Kozlov, K. V.; Sonnenfeld, A.; Michel, P.; Behnke, J. F. *Vacuum* **2003,** 71, (3), 417-436.
7. Tan, K. L.; Woon, L. L.; Wong, H. K.; Kang, E. T.; Neoh, K. G. *Macromolecules* **1993,** 26, (11), 2832-2836.
8. Borcia, C.; Borcia, G.; Dumitrascu, N. *Rom. J. Phys.* **2011,** 56, (1-2), 224-232.
9. Munzert, P.; Schulz, U.; Kaiser, N. *Surf. Coat. Technol.* **2003,** 174-175, 1048-1052.
10. Ricard, A. *J. Phys. D-Appl. Phys.* **1997,** 30, (16), 2261-2269.
11. Gu, H. Y.; Zhang, J. W.; Faucher, S.; Zhu, S. P. *Nanotechnology* **2010,** 21, (35), 355302.
12. Erbil, H. Y.; Demirel, A. L.; Avci, Y.; Mert, O. *Science* **2003,** 299, (5611), 1377-1380.

13. Edmondson, S.; Osborne, V. L.; Huck, W. T. S. *Chem. Soc. Rev.* **2004,** 33, (1), 14-22.
14. Barbey, R.; Lavanant, L.; Paripovic, D.; Schuwer, N.; Sugnaux, C.; Tugulu, S.; Klok, H. A. *Chem. Rev.* **2009,** 109, (11), 5437-5527.
15. Lee, H.; Archer, L. A. *Macromolecules* **2001,** 34, (13), 4572-4579.
16. Narrainen, A. L.; Hutchings, L. R.; Ansari, I. A.; Clarke, N.; Thompson, R. L. *Soft Matter* **2006,** 2, (2), 126-128.
17. Casazza, E.; Mariani, A.; Ricco, L.; Russo, S. *Polymer* **2002,** 43, (4), 1207-1214.
18. Betts D, J. T., LeRoux D, DeSimone JM. *ACS Symp Serries* **1998,** 685.
19. Ni, H. G.; Wang, X. F.; Zhang, W.; Wang, X. P.; Shen, Z. Q. *Surf. Sci.* **2007,** 601, (17), 3632-3639.
20. Perrier, S.; Jackson, S. G.; Haddleton, D. M.; Ameduri, B.; Boutevin, B. *Tetrahedron* **2002,** 58, (20), 4053-4059.
21. Hansen, N. M. L.; Gerstenberg, M.; Haddleton, D. M.; Hvilsted, S. *J. Polym. Sci. Pol. Chem.* **2008,** 46, (24), 8097-8111.
22. Du, J. Z.; Chen, Y. M. *Macromolecules* **2004,** 37, (17), 6322-6328.
23. Koh, K.; Ohno, K.; Tsujii, Y.; Fukuda, T. *Angew. Chem.-Int. Edit.* **2003,** 42, (35), 4194-4197.
24. Sun, Y. B.; Ding, X. B.; Zheng, Z. H.; Cheng, X.; Hu, X. H.; Peng, Y. X. *Eur. Polym. J.* **2007,** 43, (3), 762-772.
25. Granville, A. M.; Brittain, W. J. *Macromol. Rapid Commun.* **2004,** 25, (14), 1298-1302.

26. Li, H.; Bin Zhang, Z.; Hu, C. P.; Ying, S. K.; Sen Wu, S.; Xu, X. D. *React. Funct. Polym.* **2003,** 56, (3), 189-197.

27. Lim, K. T.; Lee, M. Y.; Moon, M. J.; Lee, G. D.; Hong, S. S.; Dickson, J. L.; Johnston, K. P. *Polymer* **2002,** 43, (25), 7043-7049.

28. *Wiley InterScience- Wiley Database of Polymer Properties: Free Radical Copolymerization Reactivity Ratios John Wiley & Sons, Inc.* **1999**.

29. Xiong M.; Zhang K.; . Chen Y.M. *Eur. Polym. J.* **2008,** 44, (11), 3835-3841.

30. Teng, H.X.; Koike, K.; Zhou, D.Y.; Satoh, Z.; Koike, Y.; Okamoto, Y. *J. Polym. Sci. Pol. Chem.* **2009,** 47, (1), 315-317.

31. Donald, R. V.; Dominick, R. V. *Plastics processing data handbook. Van Nostrand Reinhold, NY,* **1990**, 38.

32. Schaub, T. F.; Kellogg, G. J.; Mayes, A. M.; Kulasekere, R.; Ankner, J. F.; Kaiser, H. *Macromolecules* **1996,** 29, (11), 3982-3990.

33. Sugiyama, K.; Nemoto, T.; Koide, G.; Hirao, A. *Macromol. Symp.* **2002,** 181, 135-153.

34. Hopkinson, I.; Kiff, F. T.; Richards, R. W.; Bucknall, D. G.; Clough, A. S. *Polymer* **1997,** 38, (1), 87-98.

35. Strong, A. B. *Plastics: Materials and Processing, Third Edition, Columbus, Ohio,* **2006**, 599-600.

36. Prathab, B.; Aminabhavi, T. M.; Parthasarathi, R.; Manikandan, P.; Subramanian, V. *Polymer* **2006,** 47, (19), 6914-6924.

Chapter 4 Magnetic Organo-silica Nanoparticles for Localized Polymer Surface Modification

This chapter is reproduced based on the manuscript of Gu H, Faucher S, Zhu S. Magnetic Organo-silica Nanoparticles for Localized Polymer Surface Modification. *Macromolecular Materials and Engineering* 2011, accepted in June.

Author Contributions: Hongyan Gu performed all the lab experiments and characterizations. Dr. Santiago Faucher provided helpful discussions to this work. Dr. Shiping Zhu supervised this work, and participated in paper revision.

4.1 Abstract

Magnetic organo-silica nanoparticles were synthesized by grafting block copolymers of methacryloxypropylheptaisobutyl-T8-Silsequixane (MPB-POSS) and methyl methacrylate (MMA) from magnetic iron nanoparticles via surface-initiated atom transfer radical polymerization (ATRP). The hybrid nanoparticles had the morphology of magnetic iron core and PMMA/POSS composite shell. A small amount of the nanoparticles was added as "smart additive" in casting PMMA sheets for a localized surface modification purpose. It was demonstrated that the particles were readily brought to the surface of the casted piece by applying a magnet field to the molding. At 1wt% loading, the sample had a 50-time higher particle content in a 100μm-thick surface layer than in the bulk. The indentation hardness of the modified surface was increased by 30%.

4.2 Introduction

Polyhedral oligomeric silsesquioxanes (POSS) has a cage-like molecular structure and is regarded as the smallest particle of silica. A POSS cage normally consists of 8, 10 or 12 Si atoms with its size in the range of 1 to 3 nm[1]. The small size and other unique physical properties make POSS an ideal type of filler or reinforcement for nanocomposite materials. It has been found that POSS moieties could remarkably improve mechanical strength, elastic modulus, thermal stability and gas permeability of host materials[2-5] as well as enhance resolution/sensitivity of lithographic resists[6-9]. The recent advances in synthesis and manufacturing of

POSS derivatives with various organic substituents provide great opportunities in developing novel organic-inorganic hybrid materials, such as super hydrophobic[10,11], biocompatible[12,13], cationic conjugating[14,15] and other polymeric/composite materials[16]. POSS-containing methacrylate monomers have attracted particular attention in polymerization[17,18]. Such monomers were polymerized in solution or on surface via conventional free radical polymerization[19,20] and controlled/living radical polymerization[10,11]. Grafting of POSS methacrylate from a flat silicon wafer surface via surface-initiated atom transfer radical polymerization (ATRP) has also been reported[21]. The POSS layer thickness and polymer molecular weight has been demonstrated to be controllable using controlled free radical polymerization.

Although numerous investigations have been conducted on synthesis and characterization of POSS-containing materials, little attention has been paid to combining POSS with stimuli-responsive materials for advanced functioning. The current researches have mainly focused on developments of new composite materials[22-24] and mechanical modifications of bulk polymers[2,25,26]. However, in many applications, only localized modification, e.g. surface, is required and original bulk properties are preferably retained. A key factor in improving materials properties at certain spots or areas by POSS addition is the delivery and assembly of POSS moieties at targeted locations in the host matrix. Incorporating another functional group or smart carrier such as magnetic particle, surface-active agent, and chemical-, temperature-, light-responsive species becomes essential.

In surface modification, such as scratch/abrasion resistance, chemical protection, anti-oxidization and optoelectronics etc, it is ideal if functional additives can be localized and concentrated to targeted surface areas. Various coating techniques are widely used in surface modifications. However, it becomes particularly challenging with specially shaped and complex geometries, as well as inner surfaces. In such applications, chemical modification of bulk materials is often required. An effective alternative approach is to develop "smart additive" that can migrate to targeted areas during polymer processing. The migration can be caused by immiscibility of additive with bulk materials or by external fields, such as electrical, magnetic and shear forces, that drive additive to the targeted areas.

In this paper, we report the synthesis and application of magnetic nanoparticles grafted with POSS-PMMA copolymer. A commercial grade iron nanoparticle product is used as raw material in synthesis since it is relatively inexpensive for industrial applications. The iron nanoparticle cores function as vehicles to deliver POSS moieties to targeted locations of the host materials, while PMMA segments improve dispersion of the particles in the PMMA matrix. The POSS magnetic nanoparticles are used as additive in PMMA board casting to generate POSS-rich surfaces. The particle migration by magnetic field and surface modification for PMMA sample hardness are experimentally demonstrated.

4.3 Experimental Section

4.3.1 Materials

Table 4.1 summarizes the chemicals used in this work and their specifications.

Table 4.1 List of chemicals and their specifications

Chemicals	**Abbrev.**	**Grade, Supplier**	**Purpose**
iron nanoparticle		99.5%, 30nm, MK Impex Corp.	magnetic core of functional particles
toluene[a]		HPLC, Aldrich	solvent, synthesis of initiator Br-MTESP and SI-ATRP of nanoparticles
tetrahydrofuran[a]	THF	HPLC, Aldrich	purifictant, SI-ATRP of iron particles
petroleum ether		reagent, Aldrich	purifictant, synthesis of Br-MTESP grafted iron particles
triethylamine	TEA	99.5%, Aldrich	catalyst, synthesis of Br-MTESP and grafting it onto iron particle surface
copper bromide	CuBr	99.999% Aldrich	catalyst, surface initiated ATRP
N,N,N’,N”,N” pentamethyl-diethylenetriamine	PMDETA	99%, Aldrich	ligand, surface initiated ATRP
(3-aminopropyl) trimethoxysilane	APTES	97%, Aldrich	reactant, synthesis of Br-MTESP
α-bromoisobutyryl bromide	BiBB	98%, Aldrich	reactant, synthesis of Br-MTESP
methacryloxypropylheptaisobutyl-T8-silsequixane	MPB-POSS	99%, Gelest	monomer , surface initiated ATRP step 1
methyl methacrylate[b]	MMA	99%, Aldrich	monomer, surface initiated ATRP step 2
benzoyl peroxide	BPO	97%, Aldrich	initiator, PMMA sheet casting
poly(methyl methacrylate)	PMMA	350,000 g/mol, Aldrich	thickener, PMMA sheet casting

[a] Solvents were dried over CaH_2 and distilled under reduced pressure. [b] Inhibitor in monomer was removed by passing monomer through an inhibitor remover column (Aldrich).

4.3.2 Synthesis of Br-MTESP and Initiator-grafted Iron Particles

2-Bromo-2-methyl-N-(3-(triethoxysilyl)propyl) propanamide (Br-MTESP) was synthesized from α-bromoisobutyryl bromide and (3-aminopropyl) triethoxysilane following the literature[27]. Dispersions of iron nanoparticles were prepared as follows: 0.2 g of bare iron nanoparticles and 1 ml of oleic acid were added into 100 ml of toluene, and the mixture was ultrasonicated for 30 min. The chemical grafting of Br-MTESP onto iron nanoparticles were according to the literature[27]. The final product was precipitated with petroleum ether and was magnetically collected, washed with methanol for 5 times and dried under vacuum.

^{1}H-NMR ($CDCl_3$): 0.63 (t, 2H, $SiCH_2$), 1.19 (t, 9H, CH_3CH_2OSi), 1.65 (m, 2H, CH_2), 1.93 (q, 6H, CH_3C), 3.24(t, 2H, CH_2NH), 3.79(t, 6H, CH_3CH_2OSi), 6.88(s, 1H, NH).

4.3.3 Surface-initiated ATRP (SI-ATRP) on Iron Particles

A typical procedure for the surface-initiated ATRP of POSS on iron nanoparticles is as follows: Fe-I nanoparticle (0.15 g), POSS (1.62 g) and toluene (5 ml) were added into a 25 ml round bottom flask that was placed in an oil bath preheated to 90˚C. Copper bromide (14.4 mg), PMDETA (17.3 mg) and toluene (5 ml) were added into a 10ml pear-shaped flask. Both flasks were deoxygenated through five vacuum-refill cycles of nitrogen under stirring. The polymerization was started with the injection of the catalyst suspension into the 25 ml flask through a double-tipped needle. After 12 hours of polymerization with nitrogen protection, 5.5 ml of MMA was then injected into the reactor. The reaction continued for an additional 12 hrs at the same condition. The product was stopped by exposure to air. Polymer-grafted nanoparticles were magnetically collected, washed with THF for 5 times and vacuum-dried. The grafted polymer chains were cleaved for characterization following a method described by Wang and coworkers[28].

4.3.4 PMMA Sheet Preparation

The surface-grafted magnetic particles were applied as additive in PMMA syrup casting in the presence of a magnetic field. Scheme 4.1 shows the schematic illustration of the casting process. The casting syrup was prepared by dissolving 10wt% of PMMA (MW: 350,000 g/mol) in MMA to have its viscosity proper for casting. A desired amount of the particles and 0.1wt% of BPO were then added to the syrup followed by ultrasonication for 30 min. The mixture was then injected into a custom-designed casting cell (5 cm× 5 cm), consisting of a steel board and a glass sheet sealed by silicon rubber. The casting cell was then placed into an oven preheated to 60°C beside a permanent magnet. The permanent magnet used in this study is made of neodymium-iron-boron plated with nickel (McMASTER CARR. Cop.), and the dimension is 5 cm× 5 cm× 0.6 cm. This magnet has the ultras-high magnetic property, which was able to provide a maximum pull of about 16.8 kg. It should be noted that the placement of the casting cell with the magnet is important in controlling the migration direction of magnetic particles. In this work, the casting cell was placed parallel to the planar magnet at a distance of about 2 cm (D1) and there was also a distance of 3 cm between the cell and magnet central lines (D2). By doing so, the samples were casted under a magnetic gradient larger than that in the middle of the magnet. The migration of magnetic particles in the MMA syrup starts immediately after the placement of the magnet, and finishes in about 5 minutes to form a darker layer on one side of the mold. The polymerization of PMMA takes 6 hours in the first step at 60°C, The magnetic particles therefore migrated to one side of the mold and distributed to the surface more uniformly, and then the oven temperature was raised to 150°C for another 5 hours to complete the polymerization.

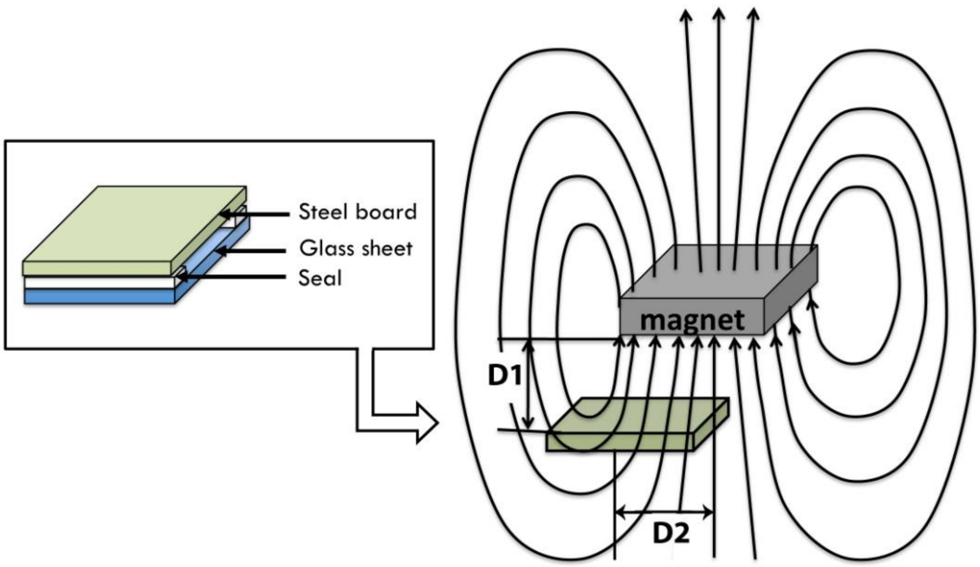

Scheme 4.1 Magnetic casting of the PMMA boards containing Fe-POSS-PMMA particles. The casting cell consists of a polished steel board, glass sheet and silicon rubber seal. The cell was placed under a planar magnet during casting.

4.3.5 Characterization and Measurement

Fourier transform infrared (FT-IR) spectra were conducted on Nicolet 510 FT-IR instrument. The particle sample was grinded with anhydrous potassium bromide and prepared as pellets using Carver press at 15,000 psi. The spectra were over the range of 500-4000 cm^{-1} in the transmission mode.

X-Ray photoelectron spectroscopy (XPS) measurements of the surface-modified iron nanoparticles were conducted on Thermo Scientific K-Alpha XPS system (East Grinstead, UK) with a monochromated Al K-Alpha x-ray source. The survey spectra were acquired with high pass energy (200 eV) and low point density (1 eV step size). Surface elemental compositions were calculated from the background-subtracted (Shirley) peak areas derived from the transmission function corrected regional spectra.

The energy dispersive x-ray spectroscopy (EDX) measurements were conducted on Tescan Vega II LSU scanning electron microscope (Tescan USA, PA) facility with X-Max 80 detector (Oxford Instruments, MA). The accelerate voltage was 20kV. Dried polymer sample was fixed to a sample stage with desired amount of carbon tape.

Thermogravimetric analysis (TGA) experiments of the particle samples were performed on Netzsch STA 409 facility at a scan rate of 10°C/min in argon atmosphere from 30°C to 800°C. The grafting densities of initiator and polymers on nanoparticle surfaces were calculated according to the following equation [29]:

$$\text{Density}(\text{molecules}/\text{nm}^2) = \frac{W \times r \times N_A \times d_{Fe}}{M\left(1-W\right) \times 3 \times 10^{21}}$$

where W is the sample weight loss, r is the iron nanoparticle radius (15 nm), N_A is Avogadro's constant, d_{Fe} is the iron density (7.874 g/cm^3), and M is the molecular weight of grafted molecules degraded from surface.

Transmission electron microscope (TEM) images of the nanoparticles were obtained from JEOL1200 TEMSCAN at an accelerating voltage of 80 keV. The bare iron particle sample prior to the modification was dispersed in cyclohexane stabilized with oleic acid (10wt% based on the particle) and oleylamine (10wt%). Fe-I and Fe-POSS-PMMA particles were directly dispersed in THF at desired concentrations. A small drop of sample dispersion was placed on a carbon-coated copper grid and was air-dried for TEM observation.

Microscopic images of PMMA sheet cross-sections were obtained from Zeiss Axiovert 100 microscope system equipped with AxioCam HR camera. In the sample preparation, a small piece of the reinforced PMMA sheet was embedded in epoxy resin and was sectioned with a microtome to a thickness of 300 nm. The epoxy was stained with toluidine blue O to assist identification of the sample edges.

The microhardness measurements of the modified PMMA sheets were conducted on CLEMEX microhardness system equipped with a pyramid tipped diamond indenter. The hardness was tested based on the Vickers hardness testing method. The loading force was 50g for all tests to ensure that the indentation depth was within the thickness of the additive-rich layer. The hardness unit was in Vickers Pyramid Number (HV), which is equivalent to kilogram force/square millimeter.

4.4. Results and Discussion

4.4.1 Surface Initiated ATRP of Iron Nanoparticles

Scheme 4.2 shows a schematic procedure for the synthesis of functionalized magnetic nanoparticles. Firstly, ATRP initiator Br-MPTES was grafted onto the iron nanoparticles in toluene under the catalysis of TEA. The resultant particles (Fe-I) were then purified and used to initiate the one-pot ATRP of MPB-POSS followed by MMA addition. The first step of the polymerization was a homopolymerization of POSS-containing monomer (MPB-POSS) in the presence of CuBr/PMDETA complex in toluene. The polymerization was carried out at 90˚C for 12 hrs under nitrogen protection. In the second step, MMA was injected into the reactor for chain extension. It is challenging to characterize polymer molecular weight using regular methods such as gel permeation chromatography, since the hydrodynamic volume of poly(MPB-POSS) differs from available polymer standards of the same molecular weight[30] with appropriate calibration lacking.

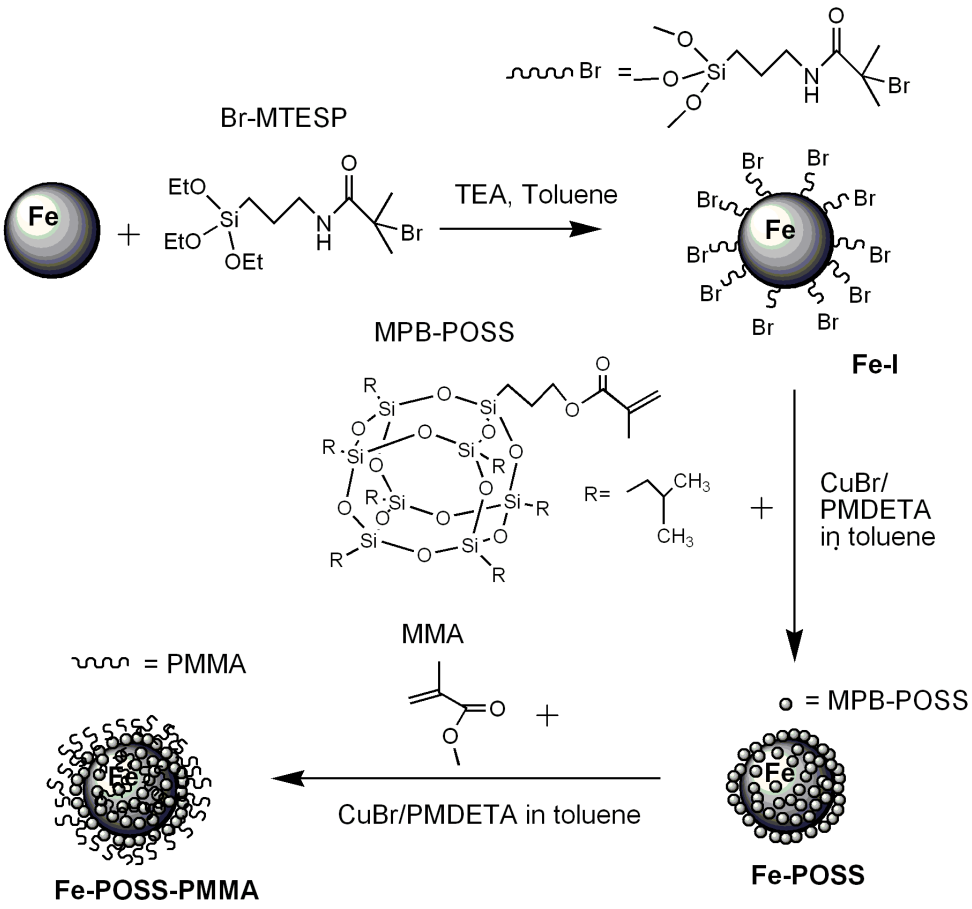

Scheme 4.2 Schematic synthesis of POSS-b-PMMA functionalized iron magnetic particles.

4.4.2 Characterization of Surface Modified Magnetic Nanoparticles

FT-IR and XPS were used to analyze the surface compositions of iron nanoparticles before and after polymer grafting. Figure 4.1 shows the IR spectra of the magnetic nanoparticles (Fe-I, Fe-POSS, and Fe-POSS-PMMA). The alkyl C-H vibration bands of CH_2 at symmetric (2850 cm^{-1}), asymmetric (2920cm^{-1}), and scissor deformation (1460 cm^{-1}) modes were observed in all the samples, confirming the presence of organic components on the particles. The characteristic band of -N-C=O at 1640 cm^{-1} were also observed after the initiator modification (Fe-I). The bands observed at 1730 cm^{-1} were assigned to C=O stretching in O-C=O, which was more apparent after the incorporation of POSS and MMA monomers. The Si-O-Si cage band [31] appeared at 1110 cm^{-1}, which was overlapped with the asymmetrical stretching vibration of C-O-C at ~1050 cm^{-1}. The 594 cm^{-1} and 600 cm^{-1} bands were from oxidized iron (Fe_3O_4) on the particle surface. The IR spectrum provided strong evidence to the attachment of ATRP initiator and the polymerization of POSS and MMA monomers on the iron particle surface.

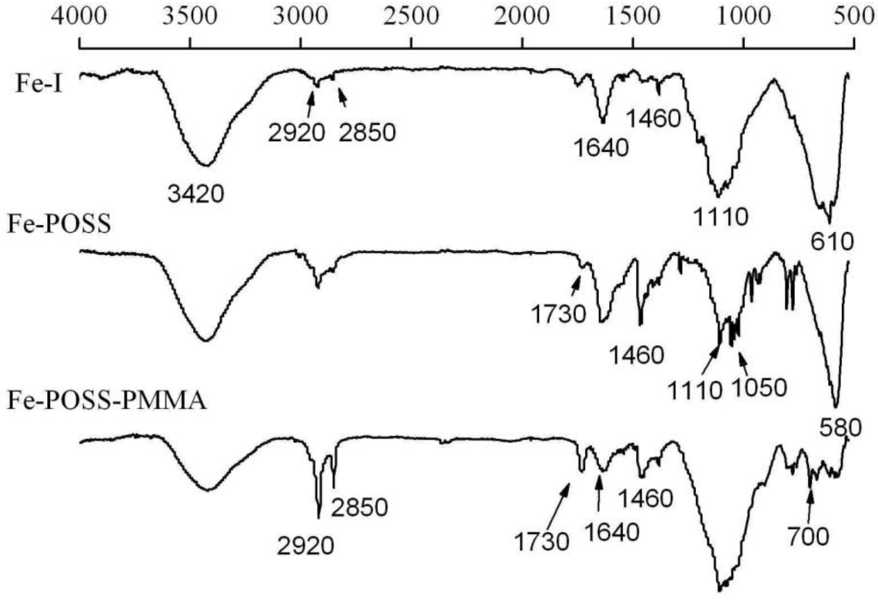

Figure 4.1 IR spectra of the magnetic particles: (1) Fe-Initiator, (2) Fe-POSS and (3) Fe- POSS-PMMA.

Figure 2 (a), (b) and (c) show the XPS surveys of iron nanoparticles grafted with ATRP initiator, MPB-POSS homopolymer and POSS-PMMA copolymer, respectively. The successful immobilization of initiator (Br-MTESP) onto iron nanoparticles (Fe-I) was confirmed by the appearance of characteristic signals of Br3p (184eV), Br3d (72eV), Si2s (155eV), Si2p (103eV), C_{1s} (285eV), N1s (403eV), and O_{1s} (533eV) in Figure 2(a). The atomic ratio of C/N/Si/Br was 7.5/0.9/1/1, which was very close to the theoretical value of 7/1/1/1 for the grafted ATRP initiator. It should be noted that the ratio of oxygen was not used since the surface of iron particles contained –OH groups or iron oxides. As shown in Figure 2(b) and (c), the ratio of C/Si/Br found on Fe-POSS and Fe-POSS-PMMA surfaces was 78/16.6/1 and 288.3/36.6/1, respectively. The increase of C and decrease of Br relative to Si confirmed the growth of polymer chains on the iron nanoparticles. On the other hand, it was found that the ratio of Si/Br on Fe-POSS-PMMA surface was about twice as much as on the Fe-POSS surface, suggesting that the residual MPB-POSS monomer was continually polymerized in the second step. It is known that each MPB-POSS monomer unit contains 8 silicon, and 35 carbon atoms. The ratio of Si/Br in Fe-POSS suggested that the number of POSS units polymerized was about twice as the amount of initiators grafted on the iron surface, and the total amount of POSS units was doubled in the second step of copolymerization with MMA. For surface-initiated ATRP, it was reported that the initiation efficiencies of surface-tethered initiators are normally between 10%-30%, depending on the shape of substrate, types of monomer, and reaction conditions [32-35]. The highest initiation efficiency of surface-tethered initiators was reported to be about 29% on Fe_3O_4 nanoparticles [35]. We estimated the initiation efficiency by comparing the Si/Br ratios on particle surface and that in the cleaved polymer chains. The elemental analysis of the cleaved polymer was performed by an energy dispersive x-ray analysis (EDX). A typical EDX spectrum is shown in Figure 4.3. The ratio of Si/Br in the cleaved MPB-POSS polymer was found to be 72.5/1, i.e., the average number of MPB-POSS units incorporated into each chain was about 9. Comparing this ratio to the XPS result of Fe-POSS surface, we found that the initiation efficiency of grafted initiators in the first step was about 22%. In the second step of surface polymerization, the total number of carbon atoms was the sum of the carbons in PMMA (N_{MMA}) and those in POSS (N_{POSS}) and the number of Si was mainly from the POSS units. The molar ratio of $N_{MMA}/N_{POSS}=5.8/1$ on the particle surface was estimated from $(N_{MMA}\times5+N_{POSS}\times35)/(N_{POSS}\times8) = 288.2/36.6$. The degree of polymerization for the grafted chains was thus about 18 POSS units and 104 of MMA units, corresponding to a molecular weight of 27,600g/mol.

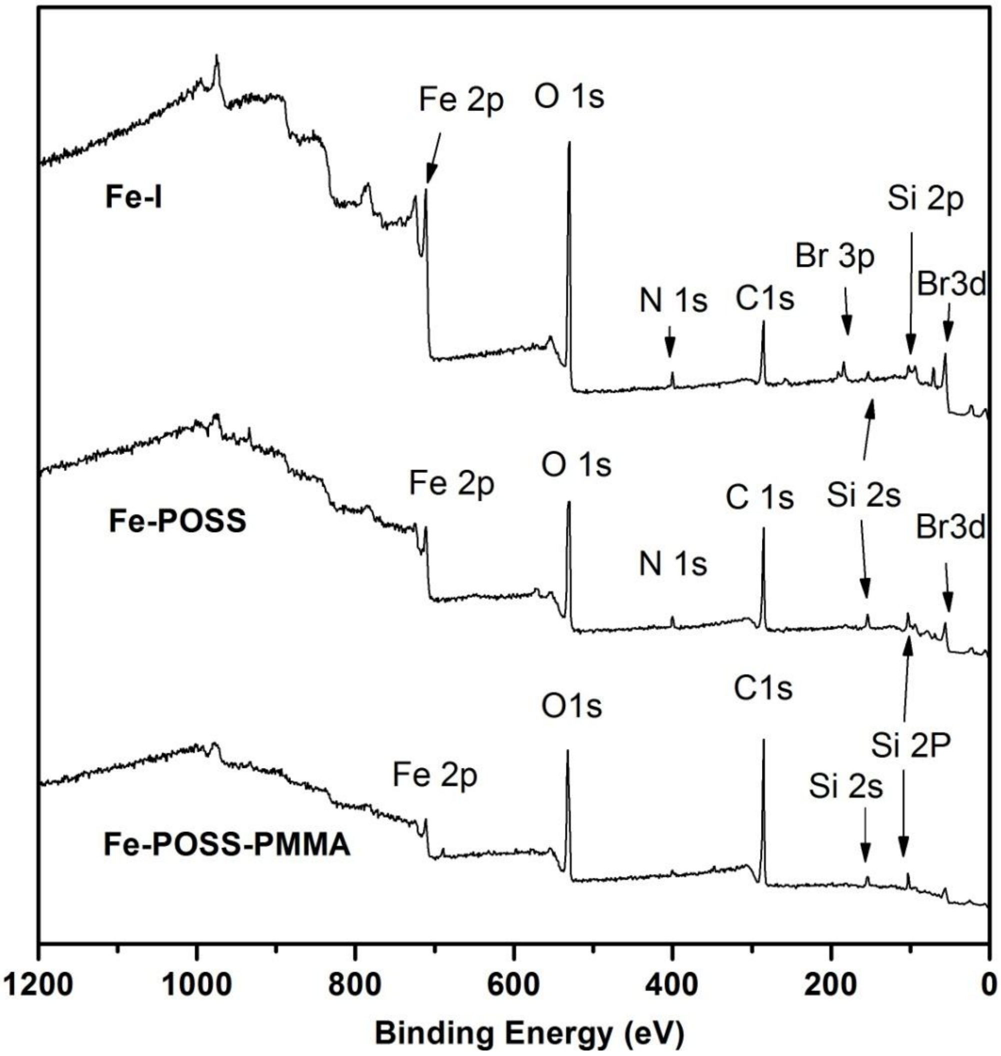

Figure 4.2 XPS survey scans of magnetic nanoparticles.

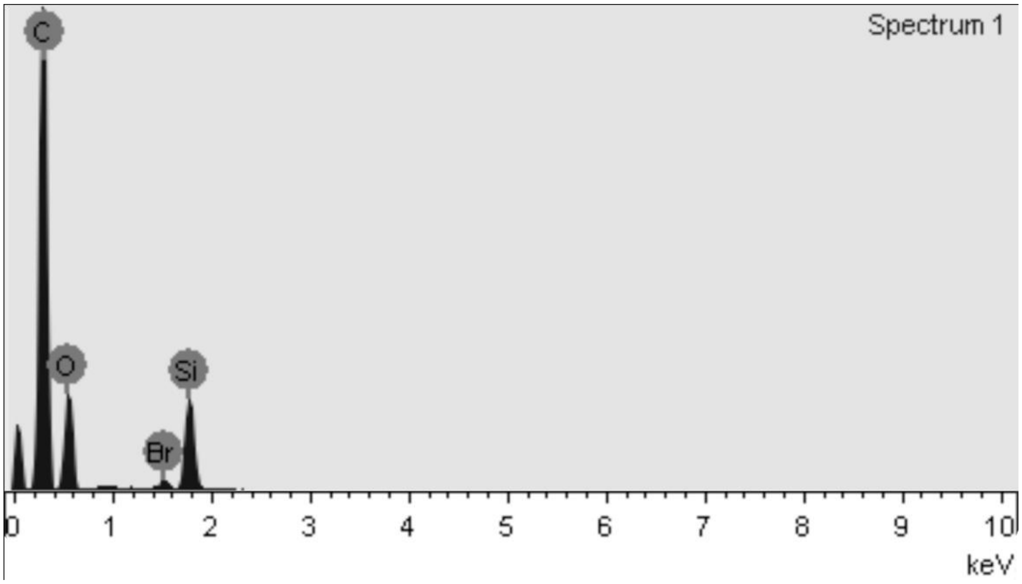

Figure 4.3 EDX spectrum of MPB-POSS polymer cleaved from iron nanoparticles. Atomic ratio of Si/Br = 72.5/1.

Figure 4.4 shows the TGA curves of Fe-I, Fe-POSS and Fe-POSS-PMMA. The weight loss of Fe-I was only 1%. Considering that the SiO_2 ashes remained after the degradation of initiator molecule, we estimated that the grafting density of Br-MTESP on the iron nanoparticles (diameter= 30 nm) was about 1.14 molecules/nm^2. This level of initiator density was slightly higher than that of flat substrate surfaces, but was comparable to the values reported on the surface-initiated polymerization on Fe_3O_4 nanoparticles[27, 35]. As shown in Figure 4.4, the weight losses of Fe-POSS and Fe-POSS-PMMA were about 6.5% and 12.9%, respectively, which were significantly higher than that of Fe-I. Based on the POSS polymer molecular weight obtained from EDX elemental analysis and TGA data, it was calculated that the grafting density of POSS polymer on iron nanoparticles was 0.31 chain/nm^2. That is, the initiation efficiency of surface-tethered Br-MTESP in the ATRP of MPB-POSS was about 27%, close to the result of 22% from the elemental analysis. Based on a similar method, it was estimated that the grafting density of POSS-PMMA copolymer on iron nanoparticles was about 0.15 chain/nm^2. Compared to the first step of polymerization, the grafting density in the second step was significantly reduced.

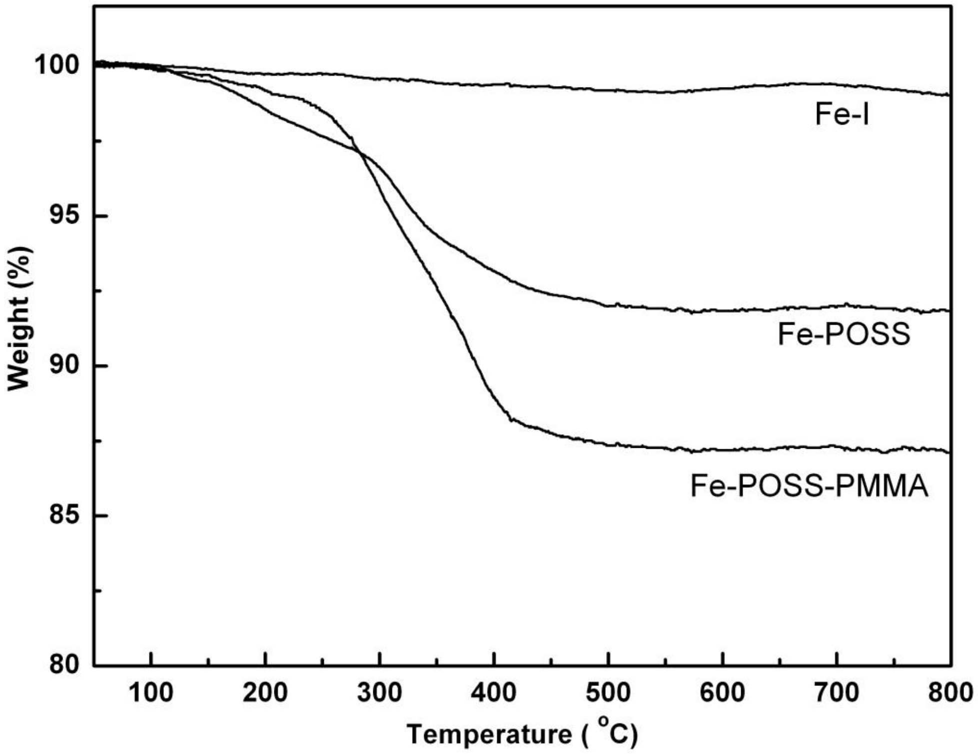

Figure 4.4 TGA curves of surface modified iron nanoparticles.

Figures 4.5(A), (B) and (C) show TEM images of the iron nanoparticles before and after functionalization. The commercially supplied iron particles were in the form of dry powder having grain size between 20-30 nm. Oleic acid and oleylamine were used as stabilizer to re-disperse the particle chunks in cyclohexane under ultrasonication. Due to strong magnetic effect and high density, it was very difficult to well re-disperse the dried iron nanoparticles even at the presence of surfactant. Most particles appeared in the form of smaller aggregates under TEM. Iron is electron-dense under TEM and the unmodified particles can thus be observed with very sharp edges (see Figure 4.5(A)). The initiator-grafted iron particles (Fe-I, Figure 4.5(B)) deposited without surfactant also appeared clear at the edges because the Br-MTESP layer was too thin to be seen under TEM. In contrast, the Fe-POSS-PMMA particles in Figure 3.5(C) appeared less sharp at their edges. There existed a translucent thin layer around the particles, which confirmed the grafting of organic/hybrid polymer species. The electron densities of PMMA and MPB-POSS polymers are between the iron core and the carbon background.

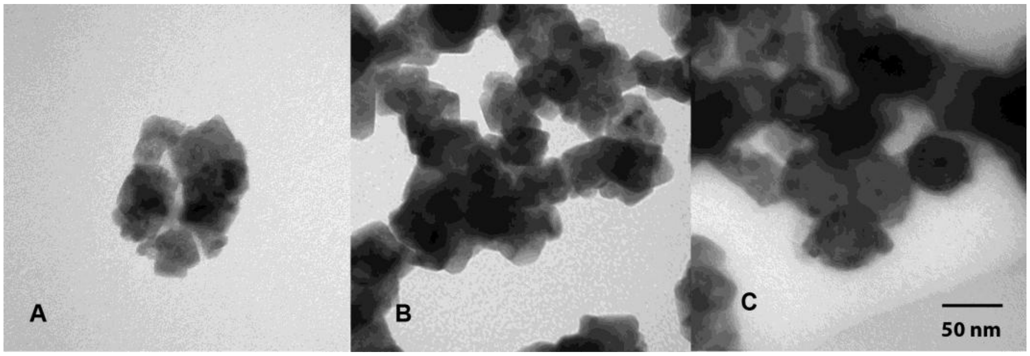

Figure 4.5 TEM images of the magnetic nanoparticles. (A) bare iron particles on carbon film; (B) initiator-grafted iron nanoparticles on carbon film; (C) Fe-

POSS-PMMA particles in PMMA thin film (60 nm thick prepared by ultramicrotomy).

4.4.3 Application of Magnetic Particles in PMMA Surface Modification

In application of the magnetic particles in PMMA casting, it was found that the stability of the magnetic particles dispersed in MMA was significantly improved after grafting with POSS-MMA block copolymer. Figure 4.6 shows four dispersions (1, 2, 3, 4) containing 0.1wt% of iron, Fe-initiator, Fe-POSS and Fe-POSS-PMMA particles, respectively. These dispersions were prepared by ultrasonication for 30 min. The iron particles started aggregation and were precipitated out immediately upon the stop of ultrasonication. The Fe-initiator and Fe-POSS particles also showed various degrees of aggregation after 20 min. In contrast, the Fe-POSS-PMMA dispersion (Sample 4 in Figure 4.6) appeared to be stable and no precipitation was observed. After 2 hours of shelf time, the iron and Fe-initiator particles (Samples 1 & 2) were mostly precipitated out with a clear MMA solution on the top of the vials. The precipitation of Fe-POSS particles (Sample 3) was slower, however there were little particles remaining in the MMA phase. The dispersion of Fe-POSS-PMMA system (Sample 4) was stable for at least 4 hours on bench with little particle precipitation.

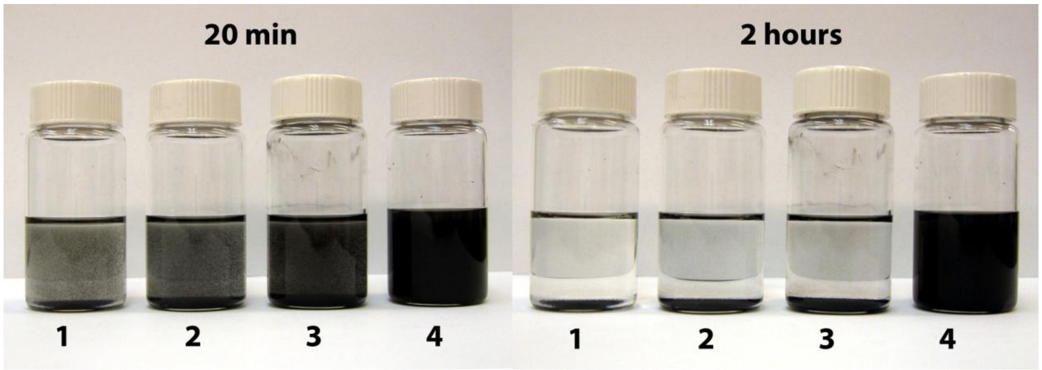

Figure 4.6 Dispersions containing 0.1wt% magnetic particles in MMA after 20 minutes and 2 hours. Sample 1, 2, 3 and 4 are pure iron particle, iron-initiator particle, iron-POSS particle and iron-POSS-PMMA particle, respectively.

The particle migration in the PMMA matrix was examined with PMMA sheets containing various amounts of magnetic additives. Small sized samples were embedded in an epoxy resin, cured and sectioned along cross-section by microtomy. Slices of about 300 nm thick were prepared and loaded onto glass slides for microscopic observation. The epoxy resin was stained with toluidiene blue O for distinction. Figure 4.7 shows the cross-sections of magnetically casted PMMA samples containing 0.04% (400 ppm), 0.1%, 0.5% and 1.0% Fe-POSS-PMMA particles. The side that faced the magnet was clearly in rich of the particles. The bulk samples prepared in this work were about 2 mm thick and the particle-rich layer had a thickness of about 100 µm. As shown in Figure 4.7, it was found that the particle concentration in the particle-rich layer was related to the initial loadings of Fe-POSS-PMMA in the MMA syrup (0.04% - 1%). Higher loadings of magnetic particles resulted in higher density of particles in the additive-rich layer, while the thickness of this layer remained unchanged. The maximum volume concentration of iron nanoparticles in the top-100 μm was found to be about 50% when 1% of Fe-POSS-PMMA was used. The 50% content in the top-layer appeared to be a saturated concentration for the Fe-POSS-PMMA particles in PMMA. Further increase in the particle loading to above 1% only increased the layer thickness but not the surface concentration. There were many factors that influenced the particle packing and assembly in the layer. It could be seen from the images in Figure 4.7 that the particles aggregated with an orientation parallel to the magnetic field (referred to Scheme 4.2). There were plenty spaces between particle aggregates perpendicular to the orientation. It is known that the magnetic force is resulted from the magnetic density gradient of the applied magnet. For a planar magnet, the magnetic density exists only in a certain directions. In this work, the magnetic force exerted on the nanoparticles was in quasi-one dimension, which brought the particles to the surface facing the magnet. On the direction perpendicular to the migration route, there was no magnetic gradient to further “squeeze” the aligned particles into a highly compacted layer.

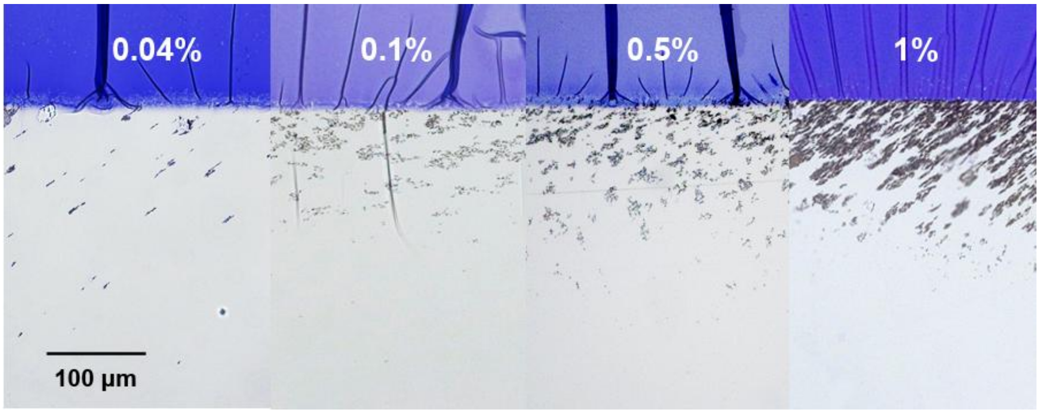

Figure 4.7 Microscopic images of a PMMA thin section (transparent) embedded in epoxy (blue). The black aggregates at the PMMA surface are the migrated magnetic nanoparticles.

The surface concentration of Fe-POSS-PMMA particles is expected to improve surface mechanical properties of the PMMA parts. It is known that nanosilica or POSS can be used as filler or reinforcement to increase the hardness of polymeric materials such as polycarbonate, polystyrene, natural rubber, etc. A CLEMEX microhardness system based on Vickers testing method was used to measure the hardness of the thin composite layers. A pyramid diamond indenter created an indentation on the sample surface with a loading force of 50 gram. Such a small force was chosen to ensure the indenter not to penetrate the magnetic particle reinforced layer (<100 μm). The hardness in Vickers Pyramid Number (HV) was calculated by HV= F/A, where F is the force applied to the indenter in kilogram and A is the area of indentation in square millimeter.

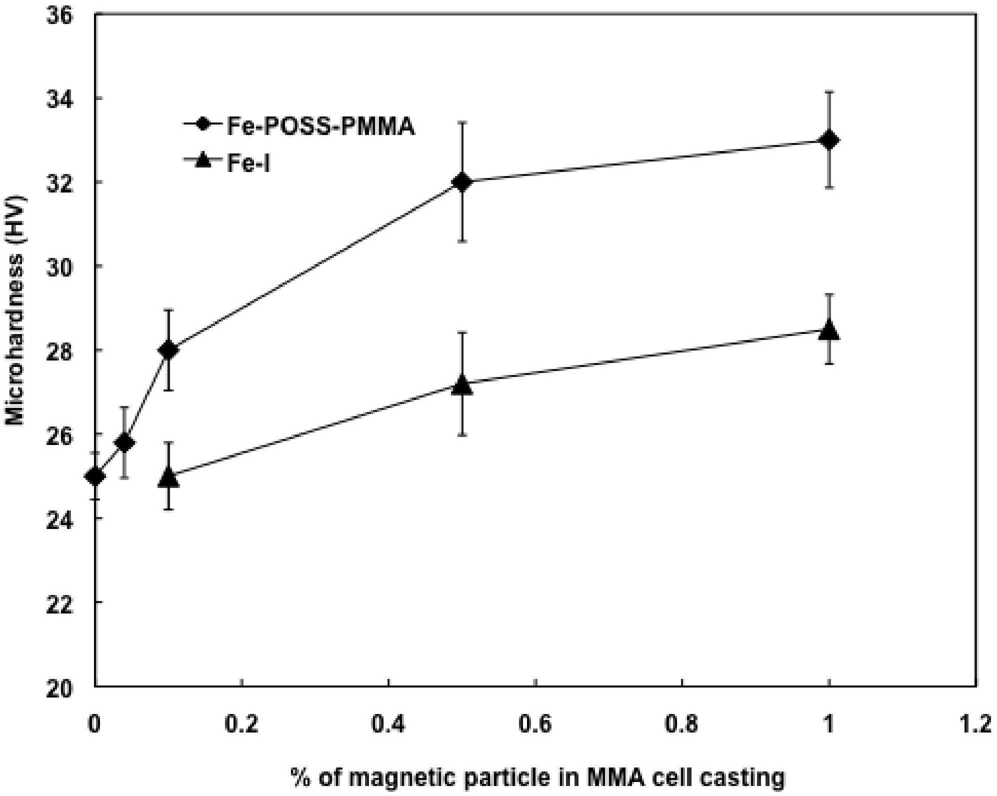

Figure 4.8 Microhardness of PMMA sample surfaces containing various amounts of Fe-POSS-PMMA and Fe-I prepared by cell casting.

Figure 4.8 shows the microhardness of PMMA samples magnetically casted with different amounts of magnetic particles. The Vicker’s hardness of PMMA blank sample was found to be 25 HV. Control experiments were also conducted by incorporating different amount of initiator-grafted iron particles (Fe-I) in MMA casting. Fe-I was used because it was better dispersed in MMA than the bare iron particle. As 0.1%, 0.5%, and 1% Fe-I was incorporated and magnetically migrated to the surface, the hardness of the particle-rich layer was found to increase only slightly from 25 HV to 28.5 HV. However, the PMMA samples containing 0.04%, 0.1%, 0.5% and 1% Fe-POSS-PMMA showed much higher hardness values of the particle-rich layers particularly with >0.5% particle loadings. As the additive loading increased from 0 to 0.5%, the hardness increased from 25 HV to 31 HV, which was about 24% of improvement. Further increase in the loading to 1% resulted in a slight increase of the hardness to about 33 HV. The microhardness results clearly demonstrated the effectiveness of Fe-POSS-PMMA additive in the surface modification of PMMA: that is, a small amount of the additive improved the surface hardness significantly.

4.5 Conclusions

Hybrid magnetic organo-silica nanoparticles grafted with POSS-MMA block copolymer were synthesized via surface-initiated ATRP. These particles were applied in a PMMA casting process for the modification of surface mechanical properties. After the polymer grafting, the nanoparticles were easily dispersed into MMA syrup with good dispersion stability. The modified particles were also characterized by FTIR and TEM-EDS, confirming the grafting of POSS-MMA copolymers. The particles were then used as additive in a very small amount in the PMMA casting that was carried out under a magnetic field. The particles in the syrup migrated to the sample surface during casting and formed a particle-rich layer about 100 μm in thickness. Increasing the particle loading in the casting solution from 0.04% to 1wt% increased in the particle concentration in the layer significantly. Adding 1wt% particle to the solution resulted in about 50% particle concentration in the surface layer upon the magnetic casting. The microhardness of the modified PMMA surfaces was improved by about 30% compared to the pure PMMA sample. This work demonstrated that the synthesized magnetic organo-silica particles could be used as smart additive in a localized surface modification of polymer parts during processing.

4.6 References

1. Li, G. Z.; Wang, L. C.; Ni, H. L.; Pittman, C. U. *J. Inorg. Organomet. Polym.* **2001,** 11, (3), 123-154.
2. Wu, X. R.; Sun, Y.; Xie, W. L.; Liu, Y. J.; Song, X. Y. *Dent. Mater.* **2010,** 26, (5), 456-462.
3. Vollenberg, P. H. T.; Heikens, D. *Polymer* **1989,** 30, (9), 1656-1662.
4. Petrovic, Z. S.; Javni, I.; Waddon, A.; Banhegyi, G. *J. Appl. Polym. Sci.* **2000,** 76, (2), 133-151.
5. Brown, D.; Marcadon, V.; Mele, P.; Alberola, N. D. *Macromolecules* **2008,** 41, (4), 1499-1511.
6. Tegou, E.; Bellas, V.; Gogolides, E.; Argitis, P.; Eon, D.; Cartry, G.; Cardinaud, C. *Chem. Mat.* **2004,** 16, (13), 2567-2577.

7. Ali, M. A.; Gonsalves, K. E.; Agrawal, A.; Jeyakumar, A.; Henderson, C. L. *Microelectron. Eng.* **2003,** 70, (1), 19-29.

8. Ali, M. A.; Gonsalves, K. E.; Golovkina, V.; Cerrina, F. *Microelectron. Eng.* **2003,** 65, (4), 454-462.

9. Eon, D.; Cartry, G.; Fernandez, V.; Cardinaud, C.; Tegou, E.; Bellas, V.; Argitis, P.; Gogolides, E. *J. Vac. Sci. Technol. B* **2004,** 22, (5), 2526-2532.

10. Mabry, J. M.; Vij, A.; Iacono, S. T.; Viers, B. D. *Angew. Chem.-Int. Edit.* **2008,** 47, (22), 4137-4140.

11. Koh, K.; Sugiyama, S.; Morinaga, T.; Ohno, K.; Tsujii, Y.; Fukuda, T.; Yamahiro, M.; Iijima, T.; Oikawa, H.; Watanabe, K.; Miyashita, T. *Macromolecules* **2005,** 38, (4), 1264-1270.

12. Wang, W. S.; Guo, Y. L.; Otaigbe, J. U. *Polymer* **2009,** 50, (24), 5749-5757.

13. Raghunath, J.; Georgiou, G.; Armitage, D.; Nazhat, S. N.; Sales, K. M.; Butler, P. E.; Seifalian, A. M. *J. Biomed. Mater. Res. Part A* **2009,** 91A, (3), 834-844.

14. Cui, L.; Chen, D. Y.; Zhu, L. *ACS Nano* **2008,** 2, (5), 921-927.

15. McCusker, C.; Carroll, J. B.; Rotello, V. M. *Chem. Commun.* **2005**, (8), 996-998.

16. Cordes, D. B.; Lickiss, P. D.; Rataboul, F. *Chem. Rev.* **2010,** 110, (4), 2081-2173.

17. Lichtenhan, J. D.; Otonari, Y. A.; Carr, M. J. *Macromolecules* **1995,** 28, (24), 8435-8437.
18. Pyun, J.; Matyjaszewski, K.; Wu, J.; Kim, G. M.; Chun, S. B.; Mather, P. T. *Polymer* **2003,** 44, (9), 2739-2750.
19. Bizet, S.; Galy, J.; Gerard, J. F. *Macromolecules* **2006,** 39, (7), 2574-2583.
20. Markovic, E.; Clarke, S.; Matisons, J.; Simon, G. P. *Macromolecules* **2008,** 41, (5), 1685-1692.
21. Chen, R. X.; Feng, W.; Zhu, S. P.; Botton, G.; Ong, B.; Wu, Y. L. *Polymer* **2006,** 47, (4), 1119-1123.
22. Oaten, M.; Choudhury, N. R. *Macromolecules* **2005,** 38, (15), 6392-6401.
23. Devaux, E.; Rochery, M.; Bourbigot, S. *Fire Mater.* **2002,** 26, (4-5), 149-154.
24. Hato, M. J.; Ray, S. S.; Luyt, A. S. *Macromol. Mater. Eng.* **2008,** 293, (9), 752-762.
25. Phillips, S. H.; Haddad, T. S.; Tomczak, S. J. *Curr. Opin. Solid State Mat. Sci.* **2004,** 8, (1), 21-29.
26. Huang, J. C.; He, C. B.; Xiao, Y.; Mya, K. Y.; Dai, J.; Siow, Y. P. *Polymer* **2003,** 44, (16), 4491-4499.
27. Sun, Y. B.; Ding, X. B.; Zheng, Z. H.; Cheng, X.; Hu, X. H.; Peng, Y. X. *Eur. Polym. J.* **2007,** 43, (3), 762-772.
28. Wang, Y.; Teng, X. W.; Wang, J. S.; Yang, H. *Nano Lett.* **2003,** 3, (6), 789-793.

29. Chen, R. X.; Madaughlin, S.; Botton, G.; Zhu, S. P. *Polymer* **2009,** 50, (18), 4293-4298.
30. Pyun, J.; Matyjaszewski, K. *Macromolecules* **2000,** 33, (1), 217-220.
31. Ramirez, C.; Rico, M.; Torres, A.; Barral, L.; Lopez, J.; Montero, B. *Eur. Polym. J.* **2008,** 44, (10), 3035-3045.
32. Husseman, M.; Malmstrom, E. E.; McNamara, M.; Mate, M.; Mecerreyes, D.; Benoit, D. G.; Hedrick, J. L.; Mansky, P.; Huang, E.; Russell, T. P.; Hawker, C. J. *Macromolecules* **1999,** 32, (5), 1424-1431.
33. Liu, Y.; Klep, V.; Zdyrko, B.; Luzinov, I. *Langmuir* **2005,** 21, (25), 11806-11813.
34. Liu, Y.; Klep, V.; Zdyrko, B.; Luzinov, I. *Langmuir* **2004,** 20, (16), 6710-6718.
35. Kobayashi, M.; Matsuno, R.; Otsuka, H.; Takahara, A. *Sci. Technol. Adv. Mater.* **2006,** 7, (7), 617-628.

Chapter 5 Controlled Chattering - A New "Cutting Edge" Technology for Nanofabrication

This chapter is reproduced based on the publication of: Gu H.; Zhang J.; Faucher S.; Zhu S., Controlled chattering - a New "Cutting Edge" Technology for Nanofabrication, *Nanotechnology*, **2010**, 21: 355302. Copyright © 2010 IOP Publishing Ltd.

Author contributions: Hongyan Gu performed all of the lab experiments, characterizations and manuscript preparation. Dr. Junwei Zhang assisted PMMA sample casting. Dr. Santiago Faucher participated in some discussion and manuscript revision. Dr. Shiping Zhu was the principle supervisor who supervised this work and participated in manuscript revision.

5.1 Abstract

Chatters are unwanted random defects on surfaces often generated in cutting samples via microtome for micrographic analysis. In this work, we demonstrate that chatters can actually be controlled for fabrication of uniform periodic wavy patterns on polymethylmethacrylate surfaces. This control in chattering is achieved based on an oscillation cutting mechanism. The pattern sizes ranging from 30 nm to a few micrometers are obtained by fine-tuning cutting speed and oscillating frequency. This simple one-step non-lithographic "cutting-edge" technology is simple and robust, with no chemical reactions and by-products involved and ease in scaling up for long-range and large-areas patterns.

5.2 Introduction

Periodic ordered structures having nano- to micrometer feature sizes are highly desirable in various nanotechnology areas such as photonic grating devices[1,2], biological patterning/sorting[3,4], microfluidic devices [5] and pattern transfer[6]. Photolithography and e-beam lithography have been the major methods for fabricating such kind of patterns since the 1980s. Although versatile in terms of complicated structures, these methods are limited by their high capital costs, selectivity of material types and inability to pattern curved and nonplanar surfaces[7-9]. Herein we introduce a controlled chattering method, by which uniform wavy patterns ranging from nano- to micrometer scale can be readily fabricated in one step using a microtome. Unlike conventional microtomy and machining, where smooth sections are desired, we modify the cutting procedure to evoke vibrations of the cutting tool that creates uniform wavy patterns on the substrate being cut. The patterns can be tuned in amplitude and wave period from 30 nm to micrometer scale by simply adjusting the cutting speed and oscillation frequency. In principle, this controlled chattering method is applicable to various types of materials with the proper set of viscoelastic properties. The current experiments were conducted on polymethyl methacrylate (PMMA) as a proof of concept. This method offers a facile route to construct wavelike patterns over a long range, on ordinary materials rather than photoresists and provides useful template for further fabrication of other nanostructures, which shows clear advantages over the conventional lithographic methods.

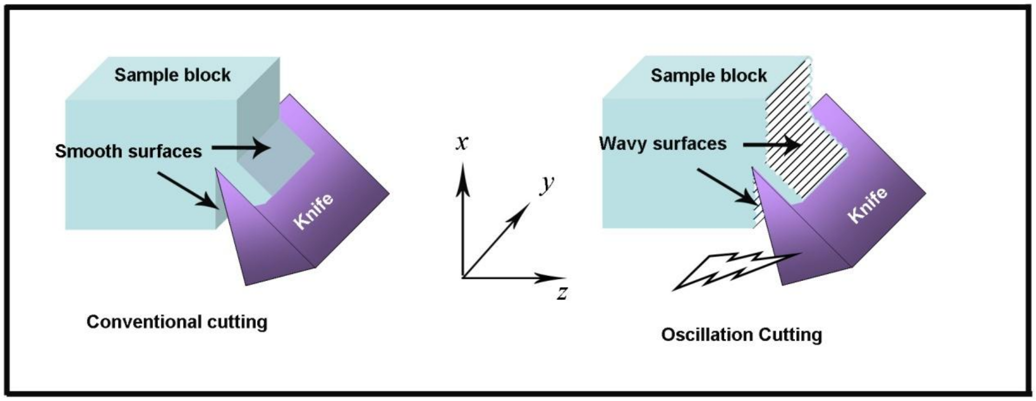

Scheme 5.1 Schematics of the conventional cutting process and the oscillating cutting process in microtome sectioning. The sample moves down in -x direction, the knife oscillates in y direction, and the cutting depth is in z direction.

The microtome has been used for decades in preparation of thin sections for optical and electron microscopy. It can be used to section a wide range of materials including metals, polymers, composites and biological samples, allowing for direct imaging of internal architectures of the samples[10]. In the conventional microtome sectioning process (Scheme 5.1, left), the cutting is conducted through a controlled mechanical advance (in the x direction) of the sample holder towards a stationary diamond knife. The depth of cut (section feed) was determined by the relative position of the sample surface plane to the edge of knife (in the z direction). During the down-stroke of the sample holder, the sample is forced against the edge of knife, resulting in a thin section being cut. When a thin section is prepared from a vitreous or inhomogeneous sample, or with improper cutting parameters, cutting artifacts could be occasionally generated[11-13]. The most common types of artifacts are chatters, compression, crevasses, and knife marks[11]. Chatters are the result of undesired mechanical vibrations during cutting, which induce variations in the section thickness or wavy structures on the workpiece[14,15]. Great efforts have been made to avoid chatters during specimen sectioning in order to attain “high quality” sections. It is known that the frequency of chatters is closely related to the source of vibration. For example, “low frequency chatters” are mostly due to the apparatus or inherent frequency of buildings. Higher vibration frequencies could be resulted from vibrations of instrument parts such as knife and specimen[16]. Sometimes, there are multi-vibration frequencies coexist in chattering, which make chatters difficult to be analyzed. A careful examination of literatures reveals that little attention has been paid to making use of the chattering mechanism and further developing it into a useful patterning method. The key to success is to find a way to control the chatters that, up to now, are considered to be random and uncontrollable. In this paper, we demonstrated a novel “cutting edge” technology based on a controlled oscillation cutting mechanism, which provides unprecedented control over chatters and can thus be used to fabricate uniform wavy patterns. This controlled chattering method is illustrated in Scheme 5.1 (right).

5.3 Experimental Section

5.3.1 Preparation of PMMA Block Samples

Narrow distribution polymethyl methacrylate (PMMA, M_W= 350,000 g/mol, Sigma-Aldrich) 1.5 g and 0.078 g of benzoyl peroxide (BPO) were dissolved in 8.5 g methyl methacrylate (MMA, 99%, Sigma-Aldrich). In preparing crosslinked PMMA samples, 0.1 g of Ethylene glycol dimethacrylate (EGDMA, 98%, Sigma-Aldrich) was also added to the solution. Inhibitor in MMA and EGDMA was removed by passing the monomers through an inhibitor remover column (Sigma-Aldrich). The polymer-monomer solution was then transferred into a glass mold with chamber dimension of 40mm×40mm×3mm. Note the pre-polymer was added to obtain proper viscosity for casting and also to reduce volatility during casting. The mold was then sealed with silicone tape and placed into an oven preheated to 70°C. The polymerization was carried out at 70°C for 5 hours, and then was held at 120°C for additional 3 hours for completion. After that, the mold was cooled in air and the PMMA board was leased and cut into 3 mm ×3 mm ×10 mm blocks for microtome sectioning.

5.3.2 Microtome Sectioning

Oscillating skiving was conducted on Leica UCT equipped with an oscillating diamond knife (DIATOME). Knife edge length: 3mm, knife angle:

35°, frequency: 25~45 kHz, amplitude: variable (0-30 V). Sample surface was pre-trimmed with razor blade into a 1mm×1mm area for sectioning. The clearance angle for sectioning was set to 6°. Sample feed was 60 nm for all samples and cutting speed was selected from 1-50 mm/s.

5.3.4 Transmission Electron Microscopy Imaging

JEOL 1200EX at an accelerating voltage of 80 kV was employed. The images were recorded by a CCD camera. Ribbons of PMMA sections were placed on 200-mesh EM copper grids and coated with a thin layer of carbon before observation. Epoxy sections were placed on the copper grids without carbon coating.

5.3.5 Atomic Force Microscopy

AFM images were taken using Veeco Digital Instruments Multimode Nanoscope III A equipped with Olympus AC160TS cantilever (Tip size <10 nm) at tapping mode.

5.3.6 Diffraction Experiment

An optical apparatus was set up with a 532 nm green laser as the light source, a collimator, an adjustable stage to hold the sample block, a screen and a digital camera to record the diffraction patterns. The laser beam was collimated to 1 mm in diameter and was directed to the patterned PMMA sample surface. The angle of incidence was adjusted to obtain the maximum diffraction orders and sharp diffraction patterns. The formed reflection diffraction pattern on the reflection screen was captured by a camera.

5.4 Results and Discussion

We used an oscillating knife (DIATOME®, 35°, Ultra sonic) in ultramicrotome to section polymer samples for fabrication of wavelike patterns with the controlled chattering method. Sectioning was undertaken at high cutting speeds and with high vibration amplitudes. The knife was forced to oscillate or chatter as it skives in a controlled manner. The oscillating diamond knife of DIATOME® was originally designed to reduce compression for sectioning biological and rigid polymer samples[12]. Driven by a piezo transducer with an ultrasonic frequency (25-45 kHz), this oscillation cutting process was similar to sawing and thus could significantly reduce the degree of compression at low cutting speeds (typically <1 mm/s)[16]. It should be noted that the sawing direction (i.e., the knife oscillation direction, y, in Scheme 5.1) is perpendicular to the cutting direction (x, opposite to the sample moving direction). However, when a high cutting speed (2-50 mm/s) was applied, it was observed that the oscillation actually induced controlled "chatters" generating wavy patterns with a uniform wavelength.

5.4.1 Controlled Chattering on PMMA

Our first controlled chattering work was conducted on PMMA samples casted by bulk polymerization of MMA in the presence of about 10% PMMA pre-polymer in glass molds (see supplementary information). The use of the pre-polymer was to adjust the solution viscosity for minimizing evaporation during molding and preparing final samples free of bubbles. The cast samples were then cut into 3mm×3mm×10mm blocks with one end trimmed down to a cross sectional area of about 1mm×1mm for microtome sectioning. Typically, it took less than one second to section a slice in controlled chattering. The section feed was set to 60 nm, and the input voltage on the oscillation knife was set to the maximum (29.9 V) for all the experiments in this study. Two oscillating frequencies (25 kHz and 40 kHz) were used to investigate the frequency effect on chatter patterns. At slow cutting speeds ≤1 mm/s, the PMMA samples prepared by the oscillating cutting were found to have smooth surfaces and there were no visible patterns under TEM observation. However when the polymer samples were cut at faster speeds (>2 mm/s) with the oscillation frequencies of 25 kHz and 40 kHz, the thin sections appeared to have uniform wavy patterns in the oscillation direction (y) and perpendicular to the cutting direction (x). Shown in Figure 5.1A-F are some representative TEM images of the PMMA sections prepared by the controlled chattering method at various cutting speeds and frequencies.

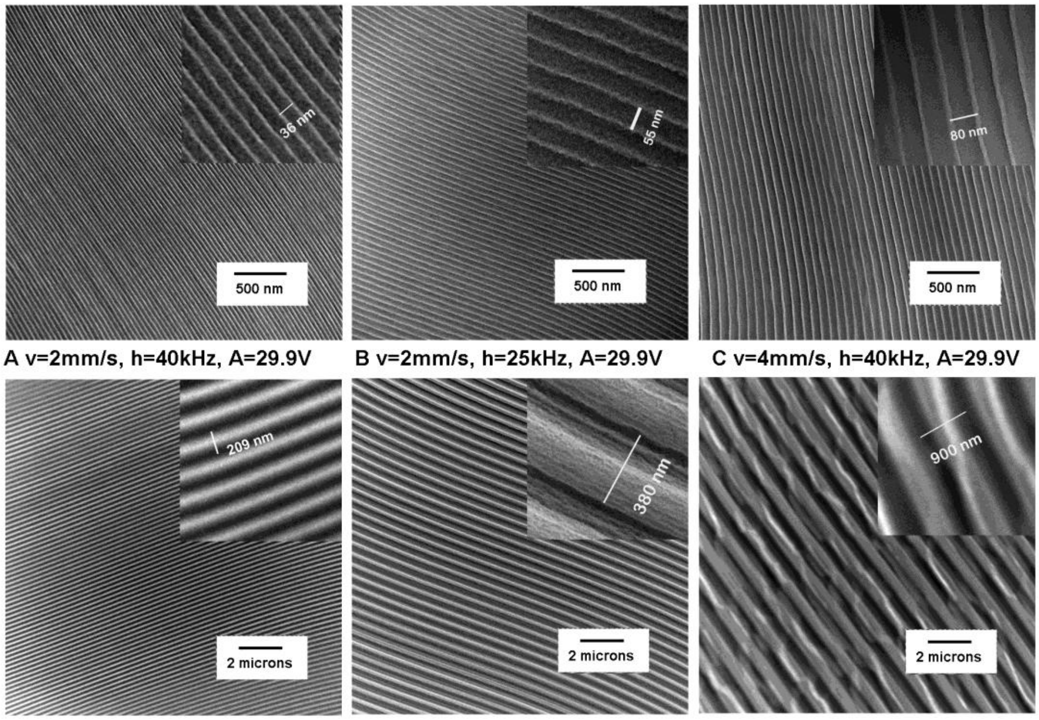

A v=2mm/s, h=40kHz, A=29.9V
B v=2mm/s, h=25kHz, A=29.9V
C v=4mm/s, h=40kHz, A=29.9V
D v=8mm/s, h=25kHz, A=29.9V
E v=16mm/s, h=25kHz, A=29.9V
F v=30mm/s, h=25kHz, A=29.9V

Figure 5.1 Representative TEM images of the PMMA sections prepared by controlled chattering, with the cutting speed (v), oscillating frequency (h) and amplitude (A) shown below each image. The cutting feed in all the experiments was set to 60 nm.

The samples shown in Figure 5.1B, 5.1D, 5.1E and 5.1F were cut at the same oscillation frequency of 25 kHz, but at different cutting speeds ranging from 2 mm/s to 30 mm/s. The sizes of wavy patterns (wavelength of wavy structures) were from 55 nm to 900 nm, which is proportional to the corresponding cutting speeds. In contrary, the samples shown Figure 5.1A and 5.1B were cut at the same cutting speed of 2 mm/s but different oscillation frequencies. When the oscillation frequency was set to 40 kHz, close to the upper-limit of the operating facility, the controlled chattering created wavy patterns of 36 nm in size. Further reducing the oscillation frequency to 25 kHz (the lower limit of the available facility) resulted in larger patterns with 55 nm in size at the same cutting speed. Although the range of the oscillation frequencies available for selection does not allow for a systematic study on the effect of oscillation frequency on pattern size, our results clearly showed a decrease in the pattern size as increased oscillation frequency. What is remarkable here is that both applied cutting speed and oscillation provide precise control over chattering such that uniform patterns are generated. Our controlled chattering experiments on the PMMA samples showed that wavy patterns are formed only if the cutting speed exceeds a minimum value for a given vibration frequency. It appears there is an onset speed in the controlled chattering operation below which no patterns can be obtained. This onset value may depend on the type of materials used. One the other hand, it appears there is also an upper limit speed in the controlled chattering, above which discontinuous pattern structures were formed[14]. As shown in Figure 5.1F, there are many defects in the patterns of the PMMA sample cut at 30 mm/s speed and 25 kHz frequency, with the structures twisted and torn in the cutting direction, and even severe discontinuities. This may be attributed to the weak rupture strain of the PMMA materials[14]. Below the rupture strain, the patterns are intact. When the cutting speed was increased to 30 mm/s, the shear strain on the shear plane (xy plane) over passed the PMMA rupture strain, yielding the discontinuous patterns.

5.4.2 Controlled Chattering on Crosslinked PMMA

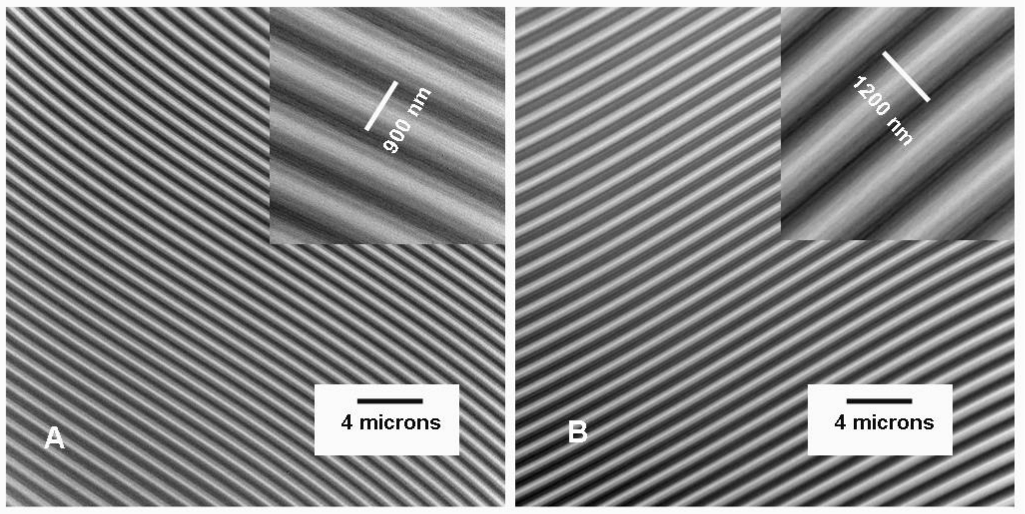

Figure 5.2 Surface patterns generated by oscillating cutting of crosslinked PMMA samples (1wt% EGDMA) at the cutting speeds of 30 mm/s (A) and 50 mm/s (B). The oscillation frequency in both runs was set to 25 kHz, the input voltage of the oscillation knife was 29.9 V and the cutting feed was 60 nm.

We prepared crosslinked PMMA samples to increase the rupture strength of the samples to be cut at high cutting speeds. The crosslinked PMMA samples were prepared from the MMA monomer solution containing 1wt% ethylene glycol dimethacrylate (EGDMA). EGDMA is a bi-functional vinyl monomer that forms a network structure through inter-chain crosslinking. The crosslinking significantly enhanced the rupture strength of the PMMA samples. As shown in

Figure 5.2A, intact wavy patterns with an average feature size of 900 nm were obtained from controlled chattering of the crosslinked PMMA samples with 30 mm/s cutting speed and 25 kHz oscillating frequency. The operation parameters in Figure 5.1F and Figure 5.2A were all the same, except for that Sample 1F was linear PMMA and Sample 2A was crosslinked. It is evident that the crosslinking made a significant improvement in the pattern quality especially at high cutting speeds. Increase the cutting speed to 50 mm/s at the same frequency resulted in even larger wavy structures of 1200 nm in size, and an improved morphology of wavy patterns as shown in Figure 5.2B.

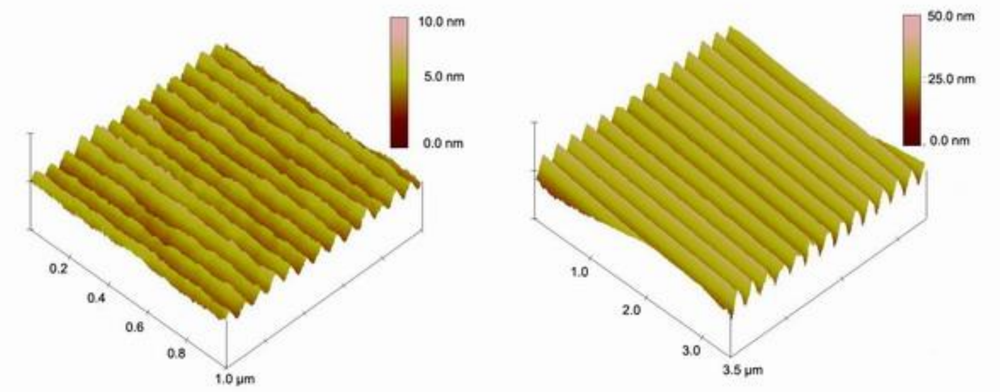

A. v= 4mm/s, h = 40 kHz, A=29.9V

B. v= 8 mm/s, h=25 kHz, A=29.9V

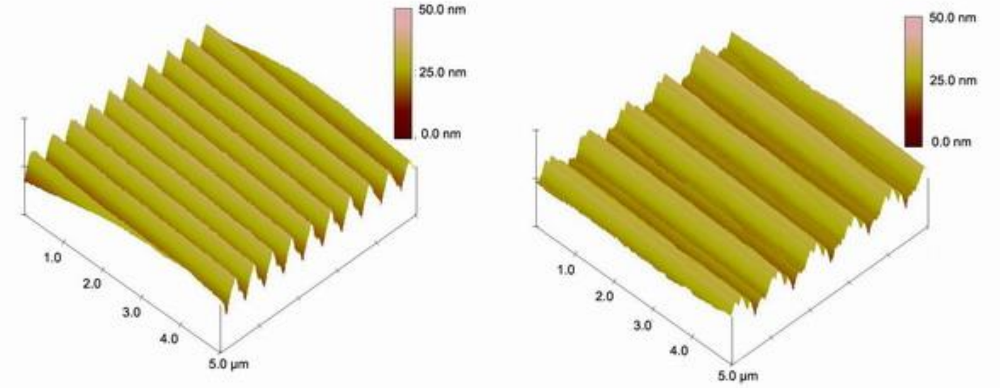

C. v= 16 mm/s, h=25 kHz, A=29.9V

D. v= 30mm/s, h=25kHz, A=29.9V

Figure 5.3 Representative AFM images of the PMMA sample blocks following controlled chattering with different cutting parameters.

5.4.3 AFM Investigation

A cutting process creates two surfaces, and thus far we have focused primarily on the thin section cut from the sample block. Figure 5.3 shows the surface topolography of some sectioned PMMA blocks observed by Atomic Force Microscopy (AFM). The samples correspond to the thin sections in Figure 5.1.

Although the patterns on the block surfaces appeared similar to those on their corresponding thin sections, the pattern wavelengths measured by AFM were found to be larger than those by TEM. Upon cutting, the thin sections were subjected to compression along the cutting direction[11]. The thin slices were found to be 10 to 40% shorter than the original block from which they were cut. This shortening in length was always close to the pattern wavelength reduction on the thin section. For example, when the PMMA sample was sectioned at v= 8 mm/s, h= 25 kHz and A= 29.9 V, the thin section in the cutting direction was shortened about 20%. The pattern wavelength on the block surface was 255 nm by AFM (Figure 5.3B) and that on the thin sections was about 209 nm by TEM (Figure 5.1 D). The agreement between the AFM and TEM results further confirms that the wave patterns observed in the thin sections were not an artifact of mechanical compression.

5.4.4 Diffraction Results

It is known that periodic surface structures with lateral dimensions in the range of 1-10 μm, have diffraction effects on visible light. The quality of the pattern structures can be examined by the diffraction maxima reflected from the surface. In optical applications, this is a typical phenomenon for diffraction gratings[17]. In our experiments, a green laser beam with the wavelength of 532 nm and the angle of incidence of 45° to the block surface was applied. Two crosslinked PMMA samples sectioned by the controlled chattering method were examined in the diffraction experiments. The diffraction patterns of the green laser beam on both sample surfaces are shown in Figure 5.4, where the spots at "0" represent the specular reflection of the incident light, and the spots at ±1, ±2 were the first and second order diffraction patterns. The diffraction patterns in Figure 5.4 can be analyzed using the diffraction equation: $d(\sin\theta_i + \sin\theta_m) = m\lambda$, where d is the space of periodic structures (wavelength of the wavy structures here), θ_i is the angle of incident light, θ_m is the diffraction angle at which the diffraction maxima display, and m is an integer representing the order of diffraction [18]. Since Sample A in Figure 5.2 has a space of about 1.2 μm in wavy structures, there were specular reflection (0 order) and first order diffractions (±1 order) shown on the reflection wall. Sample B has wavy structures of about 2 μm in space, the diffraction pattern showed 0 order diffraction and ±1, ±2 diffractions. The clear diffraction patterns demonstrated the uniformity of surface patterns prepared by the controlled chattering method in a macro-scale.

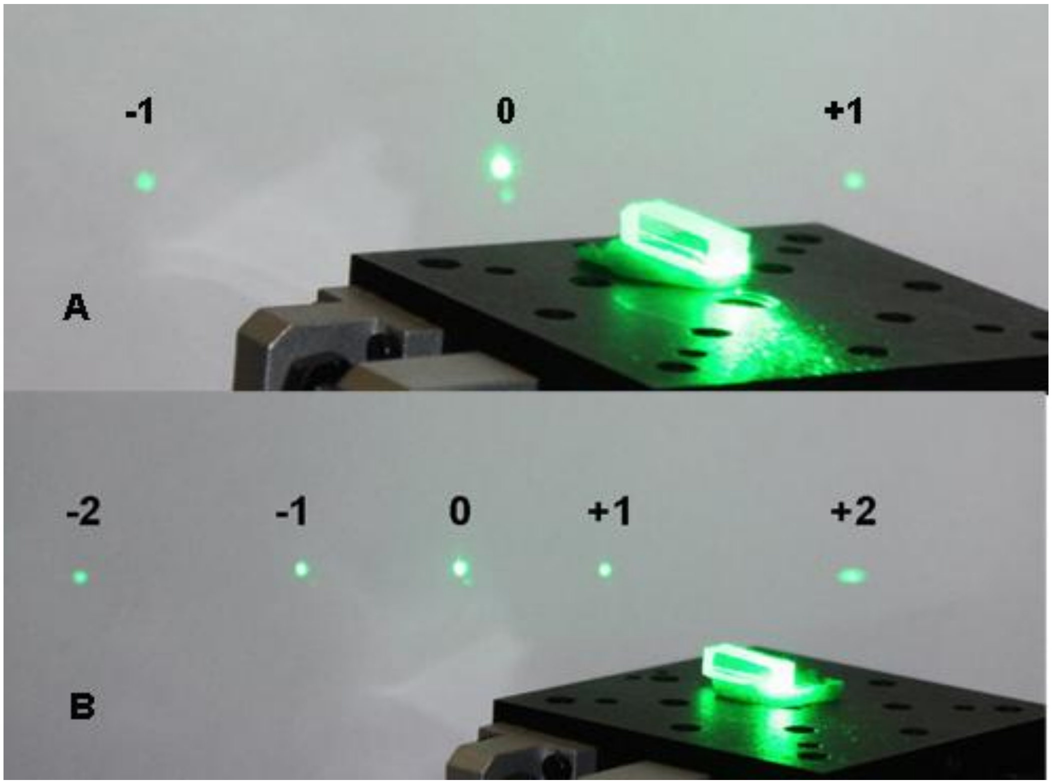

Figure 5.4 Reflective diffraction patterns of a green laser beam (532 nm) from patterned PMMA surfaces prepared by controlled chattering. (A) 0 and ±1 order diffractions of the PMMA sample surface cut at *v*= 30 mm/s, *h*= 25 kHz, and *A*= 29.9 V; (B) 0, ±1 and ±2 order diffractions of the PMMA sample surface cut at *v*= 50 mm/s, *h*= 25 kHz and *A*= 29.9 V. Note: the corresponding TEM images of the thin sections cut from these two blocks were shown in Figure 5.2.

5.5 Conclusions

This work reports for the first time a novel "cutting-edge" technology, termed as controlled chattering, based on an oscillation cutting mechanism.

Chatters are unwanted random artifacts that are often found in preparing samples by microtome for electronic microscopic analyses and that great efforts have been made to eliminate. However, we found that using an oscillating knife in ultramicrotome we can obtain uniform wavy patterns in one step. The feature size of the patterns can be fine tuned from 30 nm to a few micrometers by controlling the cutting speed and oscillating frequency. The controlled chattering method is perhaps the simplest method among the existing lithographic or non-lithographic methods for fabricating simple periodic wavy structures. It also has clear advantages in patterning diverse materials other than photoresists, on planar and nonplanar substrates, and in creating pattern sizes over a wider range. It is a truly “green” method that involves no chemical reactions and byproducts. The pattern structures can be made in long range and large area by scaling up the cutting equipment. We believe this simple and robust one-step “cutting-edge” technology hold great promise in various applications.

5.6 References

1. Xia, Y. N.; Kim, E.; Zhao, X. M.; Rogers, J. A.; Prentiss, M.; Whitesides, G. M. *Science* **1996,** 273, (5273), 347-349.

2. Zhao, X. M.; Stoddart, A.; Smith, S. P.; Kim, E.; Xia, Y.; Prentiss, M.; Whitesides, G. M. *Adv. Mater.* **1996,** 8, (5), 420-424.

3. Grainger, D. W. *Nat. Nanotechnol.* **2009,** 4, (9), 543-544.

4. Kershner, R. J.; Bozano, L. D.; Micheel, C. M.; Hung, A. M.; Fornof, A. R.; Cha, J. N.; Rettner, C. T.; Bersani, M.; Frommer, J.; Rothemund, P. W. K.; Wallraff, G. M. *Nat. Nanotechnol.* **2009,** 4, (9), 557-561.

5. Chen, D. L.; Gerdts, C. J.; Ismagilov, R. F. *J. Am. Chem. Soc.* **2005,** 127, (27), 9672-9673.

6. Kim, S. O.; Solak, H. H.; Stoykovich, M. P.; Ferrier, N. J.; de Pablo, J. J.; Nealey, P. F. *Nature* **2003,** 424, (6947), 411-414.

7. Quake, S. R.; Scherer, A. *Science* **2000,** 290, (5496), 1536-1540.

8. Gates, B. D.; Xu, Q. B.; Stewart, M.; Ryan, D.; Willson, C. G.; Whitesides, G. M. *Chem. Rev.* **2005,** 105, (4), 1171-1196.

9. Perl, A.; Reinhoudt, D. N.; Huskens, J. *Adv. Mater.* **2009,** 21, (22), 2257-2268.

10. Glauert, A. M. *Practical methods in electron microscopy. American Elsevier publishing Co. Inc.: New York.* **1984**.

11. Al-Amoudi, A.; Studer, D.; Dubochet, J. *J. Struct. Biol.* **2005,** 150, (1), 109-121.

12. Giraud-Guille, M. M. *Tissue and Cell* **1986,** 18, (4), 603-620.

13. Studer, D.; Gnaegi, H. *J. Microsc.-Oxf.* **2000,** 197, 94-100.

14. Kobayashi, A. *Machining of plastics. McGraw-Hill Book Company, New York.* **1967,** 14-20.

15. Wiercigroch, M.; Budak, E. *Philos. Trans. R. Soc. Lond. Ser. A-Math. Phys. Eng. Sci.* **2001,** 359, (1781), 663-693.

16. Al-Amoudi, A.; Dubochet, J.; Gnaegi, H.; Luthi, W.; Studer, D. *J. Microsc.-Oxf.* **2003,** 212, 26-33.

17. Benton, S. A.; Bove, V. M. *Holographic imaging, John Wiley & Sons, Inc., Hoboken* **2008**, 45-52.

18. Smith, F. G.; King, T. A. *Optics and photonics: an introduction, John Wiley & Sons, Ltd, Chichester.* **2000,** 191.

Chapter 6 Controlled Chattering on PMMA and Epoxy: Effect of Crosslinking and Cutting Speed on Pattern Formation

This chapter is reproduced based on the article of Gu H, Faucher S, Zhu S. Controlled Chattering on PMMA and Epoxy: Effect of Crosslinking and Cutting Speed on Pattern Formation, *Polymer* **2011**, 52(9): 2025-2031. Copyright © 2011 Elsevier Ltd.

Author Contributions: Hongyan Gu performed the lab experiments, characterization and manuscript preparation. Dr. Santiago Faucher participated in some discussions of this work. Dr. Shiping Zhu supervised this work and participated in paper revision.

6.1 Abstract

Controlled chattering is a cutting process with forced oscillation on the cutting tool, which creates wavy patterns on a variety of polymer surfaces with periods tunable from nano- to micrometer. It was found that the quality of surface finish after high-speed cutting was significantly improved when linear polymer chains are crosslinked. The pattern size (period) on thin sections is determined by the degree of crosslinking, which is dependent on the material’s hardness and elastic properties. Controlled chattering has also been successfully conducted on epoxy samples and the relationship between cutting speed and pattern structure is established.

6.2 Introduction

The ability to engineer long-range ordered nanostructures, especially with well-controlled spatial arrangement is highly desirable in the applications of nanoelectronics[1], optoelectronics[2,3], biotechnology[4,5], and nanodevices[6]. Nowadays, there are numerous numbers of technologies developed to prototype patterned nanostructures[7-10]. Conventional lithographic method such as photolithography is able to fabricate patterned structures with lateral dimension in the sub-wavelength range. However, this approach needs to be conducted in a clean room condition and is only applicable to a limited set of materials such as photoresists[11]. In comparison, surface patterning by self-assembly of copolymers is capable of producing patterns down to nano-scale and on a larger variety of materials. However this approach is limited to a small pattern area, in which grain boundaries are in the micrometer scale[12]. Surface patterning based on evaporative self-assembly of nonvolatile solutes (e.g. coffee rings, fingering patterns, and polygonal network structures) is another nonlithographic approach to create a diversity of ordered structures[13,14]. It offers fast and large-scale production but is challenging to achieve good control over pattern uniformity. Other patterning methods, mainly based on soft-lithography, require pattern transfer and involve multi-step procedures[15,16]. Recently, we have proposed and demonstrated a new non-lithography patterning method based on cutting, i.e., Controlled Chattering[17]. In such a process, chatters are invoked intentionally by applying an oscillating cutting tool such as ultramicrotome during surface finishing. These chatters formed on the new surfaces appear highly uniform in structure and are tunable through controlling cutting speed and oscillation frequency. The controlled chattering method offers a convenient and cost effective approach to fabricate periodic wavy patterns on a variety of materials with proper viscoelastic properties.

The method of controlled chattering on polymethylmathacrylate (PMMA) samples was reported in our previous article[17]. It was found that the size of patterns was directly related to cutting speed within a certain range. Above the speed limit, the structure of surface patterns became very rough, and the cut thin sections appeared to be distorted or broken. This was mainly attributed to the low rupture strength of PMMA, which failed to sustain the shearing force exerted by the cutting tool during high-speed cutting. It is hypothesized in this work that the incorporation of a crosslinking agent to the PMMA material would improve the quality of surface finishing in controlled chattering, as the crosslinking provides anchor points to form polymeric network structure and thus the toughness of the material is enhanced. Since the mechanical properties of polymer materials can be readily altered by incorporation of crosslinkers or fillers, it is fundamentally important to study the effect of crosslinking on the structure of patterns fabricated by controlled chattering. Also studied in this work is Spurrs' epoxy[18], another type of crosslinked polymer materials, which is often used as an embedding material for microtome sectioning. The mechanical properties of Spurrs' epoxy are tuned to facilitate sectioning and sample protection. The applicability of controlled chattering on epoxies further extends its potential application to a larger variety of fields. In this paper, we report the controlled chattering on crosslinked polymer samples including Spurrs' epoxy and PMMA with different amount of crosslinkers. The structure of patterns on both block surface and thin film are examined by TEM and AFM.

6.3 Experimental Section

6.3.1 Sample Preparation

PMMA samples were prepared in the following steps: (1) Monomer syrup containing 8.5 g methyl methacrylate (MMA, 99%, Aldrich), 1.5 g polymethyl methacrylate (PMMA, M_W = 350,000 g/mol, Aldrich), 0.078g benzoyl peroxide (BPO, 97%, Aldrich) was prepared in advance. The pre-polymer was added to obtain proper viscosity for casting and also to reduce volatility during casting. (2) The above monomer syrup was mixed with desired amount of ethylene glycol dimethacrylate (EGDMA, 98%, Aldrich), and was injected into a glass cell-casting mold (50 mm × 50 mm × 3 mm). (3) The filled casting mold was placed into an oven preheated to 70°C. The polymerization was carried out at 70°C for 5 hours, and then was held at 120°C for additional 3 hours for completion. (4) Finally, the mold was cooled in air and the PMMA board was released and cut into small blocks for microtome sectioning. Epoxy samples were prepared following to the literature[18].

6.3.2 Controlled Chattering Operation

The oscillating sectioning was conducted on a Leica UCT ultramicrotome equipped with an oscillating diamond knife (DIATOME®, knife edge length: 3mm, knife angle: 35°, frequency: 25~45 kHz, amplitude: variable from 0-30 V). The cutting speed was controlled from 2 mm/s to 80 mm/s. The sample surface was pre-trimmed with a razor blade into a 1 mm ×1 mm area for sectioning. The clearance angle for sectioning was set to 6°. The section feed was 60 nm and input voltage for pizo transducer was 29.9V for all the sectioning in this work.

6.3.3 Transmission Electron Microscope (TEM)

TEM microscope was conducted on JEOL 1200EX at an accelerating voltage of 80 kV. The images were recorded with a CCD camera. Ribbons of PMMA sections were placed on 200-mesh EM copper grids with post carbon coating.

6.3.4 Atomic Force Microscope (AFM)

AFM images were taken on the Veeco Dimension Icon Atomic Force Microscope equipped with Veeco TESPA probe (Tip radius: 8 nm) on tapping mode.

6.3.5 Mechanical Properties Tests

The microhardness measurements of the polymer samples were conducted on a CLEMEX microhardness system equipped with a pyramid tipped diamond indenter. The hardness was tested based on the Vickers hardness testing method at a loading force of 50 g. The hardness unit was in Vickers Pyramid Number (HV), which is equivalent to kilogram force/square millimeter. The tensile tests of the polymer samples were conducted on an INSTRON 4411 instrument at 25°C and 50% humidity. The loading force limit was 5 KN and the crosshead speed was 1 mm/min. The displacement was measured by an extensometer. The PMMA samples were casted in glass molds (75 mm×75 mm×1.5 mm) and the epoxy samples were casted in Teflon molds. The dimensions of the dumbell shaped specimens were machined according to ASTM D638. The cross section of specimens in the gauge length was about 5 mm× 1.5 mm. A minimum of 5 specimens were prepared and tested for every batch.

6.4. Results and Discussion

6.4.1 Controlled Chattering on Crosslinked PMMA Samples

It is known that the incorporation of a crosslinking agent into linear polymers could improve various materials' properties such as modulus of elasticity, chemical resistance, glass transition temperature, stiffness, hardness and so on. The crosslinkers provide anchor points for the linear polymer chains, which could restrain excessive movement of the chains and maintain properties of the polymers in a dynamic process[17]. During high-speed cutting, it is hypothesized that crosslinked polymers can yield higher quality surface structures than linear polymers. Moreover, the degree of crosslinking affects the mechanical properties of polymer and thus might give different results of controlled chattering. In this work, the bifunctional comonomer ethylene glycol dimethacrylate (EGDMA) was used to crosslink PMMA chains. Five different

EGDMA concentration levels were added to the MMA syrup for casting: 0.5%, 1%, 2%, 3% and 4% based on the total weight. In selection of the cutting parameters, we found that higher cutting speed generated larger wavy patterns and the effects of materials properties on the pattern size are more significant at lower cutting speeds. A cutting speed of 30-80 mm/s (at 25 kHz) generated sub- or micrometer sized patterns that were proven to be useful in diffraction gratings. Furthermore, we found that there existed a critical speed at 30 mm/s (25 kHz oscillation frequency) with the uncrosslinked PMMA samples, above which the section started to break. The cutting parameters of 30 mm/s speed and 25 kHz frequency were therefore chosen in this study of crosslinking effect on pattern formation.

Figure 6.1 shows the representative TEM images of the PMMA thin sections having various amounts of EGDMA. Without crosslinking, the pattern structure of the linear PMMA surface appeared broken and twisted when sectioned at this speed (Fig. 1(A)). It was difficult to define the pattern size of the broken PMMA thin films since the structures were not uniform. However, for the samples containing 0.5% to 4wt% EGDMA, the wavy pattern morphologies were significantly improved under the same preparation conditions. It was noticed that the pattern sizes of the crosslinked PMMA thin sections varied with the degree of crosslinking. For example, in Fig. 6.1(B), 6.1(C) and 6.1(D), where the samples contained 0.5%, 1% 2% and 3% EGDMA (based on weight), the average pattern sizes were 775, 813, 850, 871 nm, respectively. As the amount of crosslinker was further increased to 4%, the average pattern size on PMMA thin sections was slightly decreased to 843 nm.

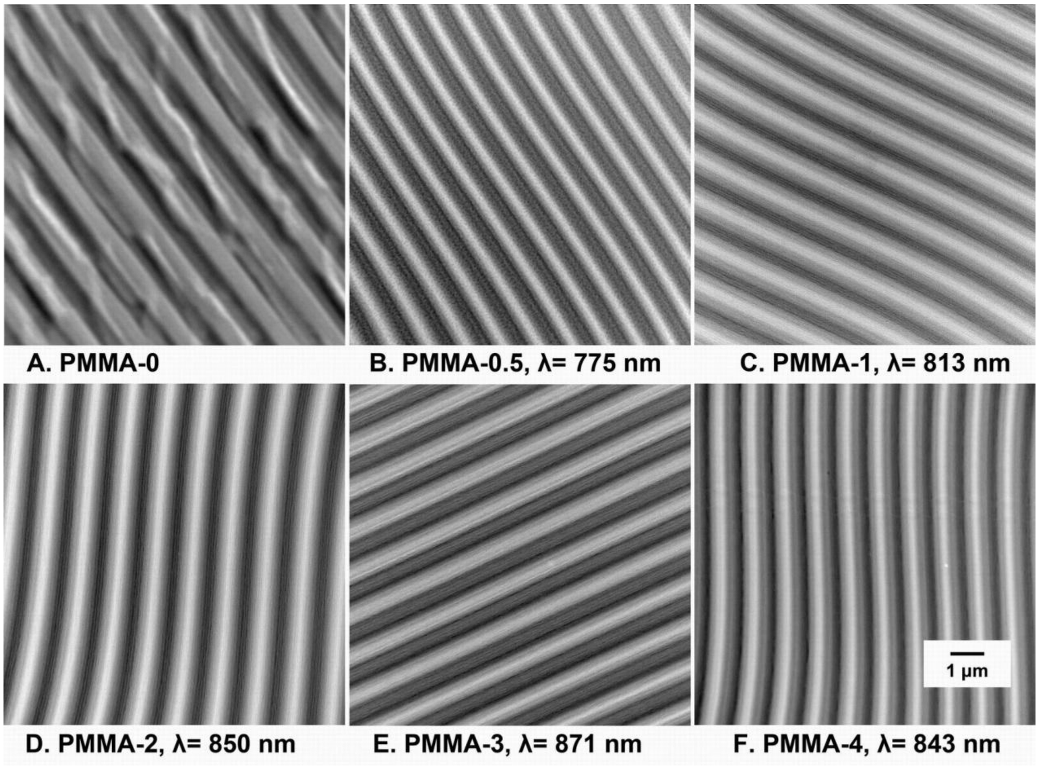

Figure 6.1 TEM images of PMMA thin sections containing different amount of crosslinking agent EGDMA. The numbers in PMMA-n denote the weight percent of EGDMA incorporated in the PMMA formulation. All the sections were prepared by controlled chattering at a cutting speed of 30 mm/s and an oscillation frequency of 25 kHz.

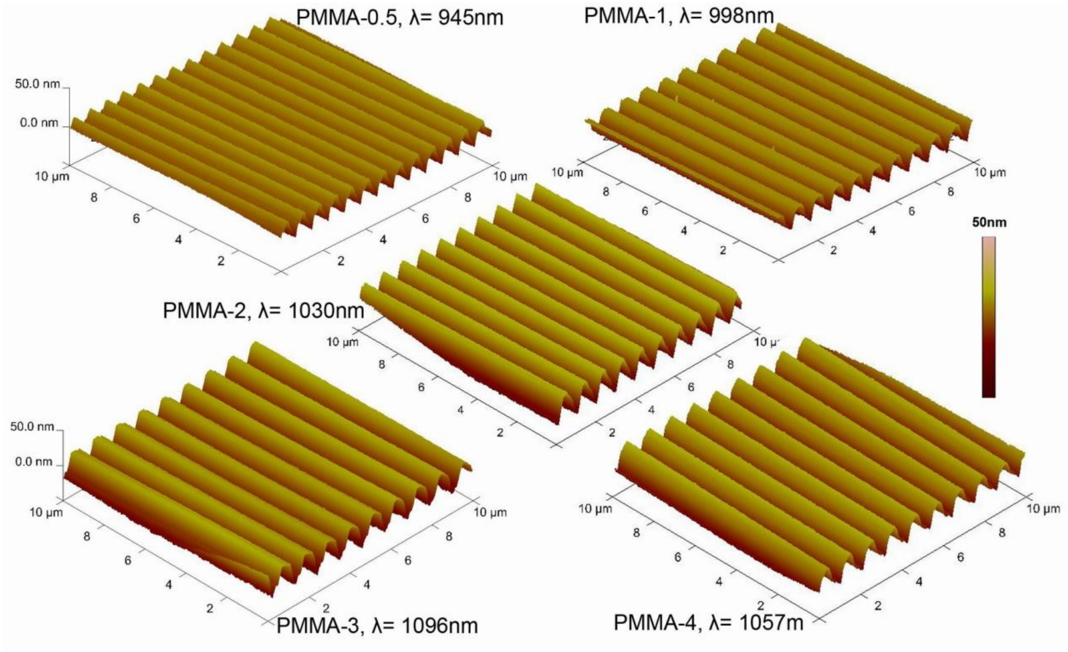

Figure 6.2 3D AFM images of crosslinked PMMA block surfaces and their average pattern sizes (λ). The number n in PMMA-n denotes the weight percent of EGDMA incorporated in the PMMA formulation. The cutting speed is 30 mm/s and the oscillating frequency is 25 kHz.

An oscillation cutting process creates two new surfaces in every cut, one on the newly formed thin section, and the other on the sample block. The surface structures of the sample blocks were examined by AFM. Representative 3D images are shown in Figure 6.2. In general, the patterns found on the blocks were similar to those on their corresponding thin sections from the same cut, but their sizes were different. Shown in Fig. 6.2 are the patterns generated on the block surfaces of the PMMA-0.5, PMMA-1, PMMA-2, PMMA-3 and PMMA-4 measured by AFM. The average sizes of the patterns are 945, 998, 1030, 1096 and 1057 nm, respectively. However on the thin sections cut from these blocks (Figure 6.1), the average pattern sizes were 775, 813, 850, 871 and 843 nm, respectively. It is known that when sectioning plastic specimens, the length of chips could be shortened as a result of compression introduced during cutting. This shortening along the cutting direction also causes compression of wavy patterns on thin sections. The degree of compression on the thin section was about 18% - 20% for all the crosslinked PMMA samples containing 0.5% - 4% EGDMA. It is evident that the degree of compression was not significantly affected by the degree of crosslinking at a fixed cutting condition. Therefore, the pattern size on the crosslinked PMMA thin section can be considered to be proportional to that of the block surface. It is hypothesized that the different amount of crosslinker altered the mechanical property of PMMA and thus resulted in a different chattering mechanism on the block surface. The difference in chattering mechanism eventually yielded the different pattern sizes.

The formation of wavy surfaces during controlled chattering involves the separation of bulk material along the knife-edge as well as compression and tension causing deformation of the material on the new surface. To obtain a well-defined surface structure, materials should have sufficient resistance to deformation during machining. We firstly measured the Vickers hardness of the crosslinked PMMA samples on a CLEMEX micronhardness testing system. The hardness is a measurement of the resistance of material to permanent shape change under an applied force and is calculated based on load over surface area of the indentation. The unit HV is equivalent to kilogram force/square millimeter. Hardness results of crosslinked PMMA were plotted together with the pattern sizes measured on thin films and block surfaces versus the amount of EGDMA in Figure 6.3. Generally, the harness data are consistent with the pattern sizes that showed the increased trend as a function of EGDMA concentration up to 3%, however there is a slight drop both in microhardness and pattern size when the crosslinker-degree was increased from 3% to 4%.

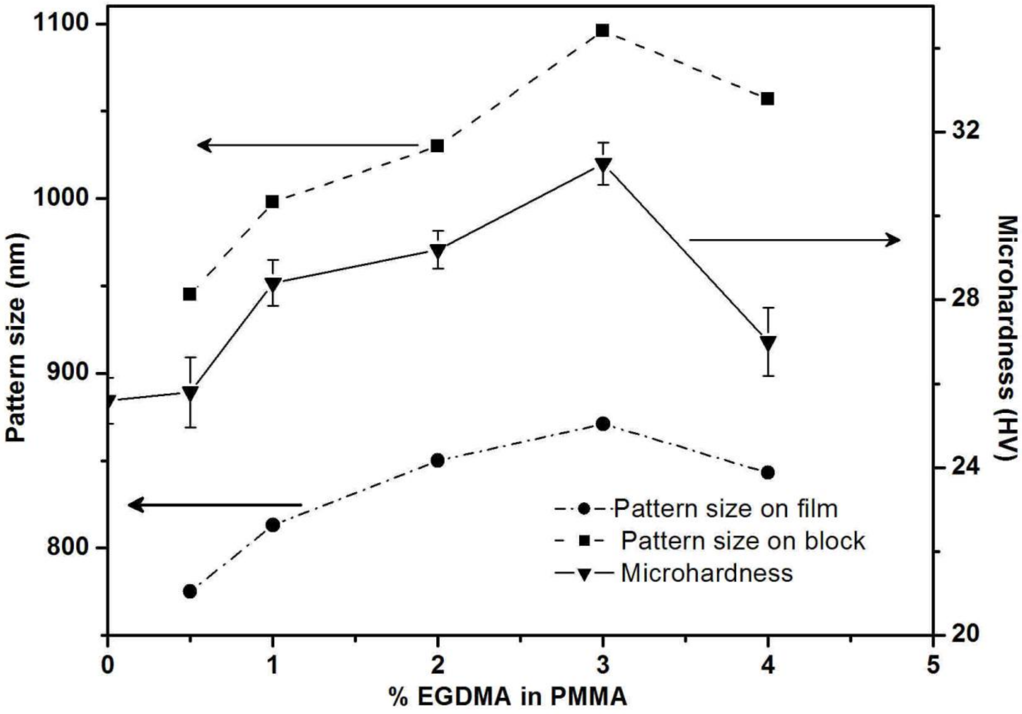

Figure 6.3 Pattern size (on thin film and block surface) and microhardness of crosslinked PMMA samples with various amount of crosslinker.

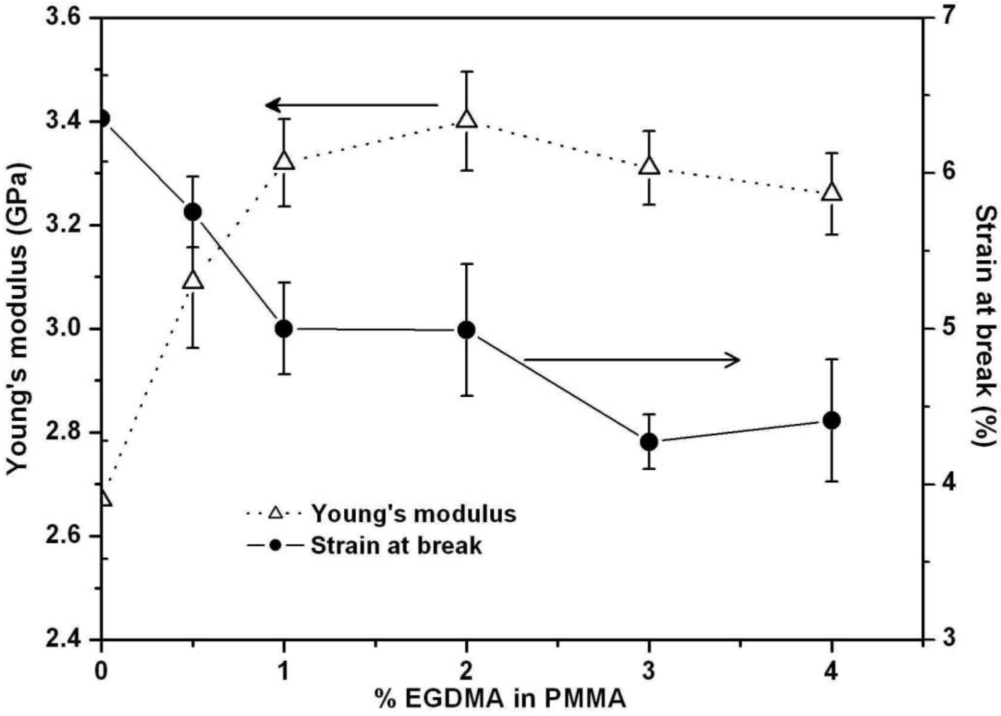

Figure 6.4 Values of Young's modulus (GPa) and strain at break versus the amount of crosslinking agent in PMMA (%).

Besides the hardness tests, tensile experiments were also conducted to investigate the tensile properties of the crosslinked PMMA and the effect on the controlled chattering. Since Young's modulus represents the stiffness of material in the elastic region, it is an important parameter in resisting deformation of the material, and is highly related to the outcome of surface finish. When chattered at 30 mm/s speed and 25 kHz frequency, the PMMA sample sections appeared broken. It indicates that the high impact stress generated at 30 mm/s exceeded the ultimate strength of the material, leading to discontinuous chips. However, the incorporation of 0.5% crosslinking agent resulted in a significant improvement of the surface pattern structures (Figure 6.1(A) and (B)). The Young's modulus of PMMA-0.5 was about 3.09 GPa as shown in Figure 4, while it was only 2.67 GPa for the uncrosslinked PMMA. It is known that with moderate degree of crosslinking, the chain mobility is reduced through forming a network structure[19]. Therefore, the modulus of the materials is increased. In this study, the Young's modulus of PMMA increased with increasing EGDMA concentration until 2%. Further increase of crosslinking agent above this amount did not improve its Young's modulus. It actually experienced a slight decrease when EGDMA was over 3%. Although the amount of decrease was not significant as compared to experiment error of the modulus measurement, it was generally accepted that with increasing degree of crosslinking in the network, the heterogeneity of network also increases[20-22]. As a result, the polymer becomes more brittle, and shows lower the resistance to impact forces[23]. Our result agreed with that reported by Deb and coworkers, in which Young's modulus of PMMA crosslinked by EGDMA (0, 2%, 5%, 10%) initiated with 0.75% of BPO was studied[24].

In tensile experiment, strain value at the break point (break strain) represents maximum deformation of the materials under maximum stress. In machining, it could also be used in the analysis for degree of material deformation after disruptive processing. Our result showed that the thin sections prepared by controlled chattering were subjected to compression that led to reduced pattern sizes on the thin sections. It is anticipated that the block surfaces were subjected to similar compressive forces as the thin sections and thus the pattern size on the block surface could be related to the ultimate strain of the material. As shown in Figure 6.4 (filled dots), the strain values at break point of PMMA decreased steadily with increasing crosslinking degree from 0 to 2% and reached a plateau when the crosslinking degree was over 3%. Similar to the tensile modulus, the decreased break strain of crosslinked PMMA is due to the reduced flexibility of polymer network and the material becomes more brittle. The effect of crosslinking on the ultimate strain was apparent at low degree (below 2%) and became less significant when the crosslinking degree was between 2%- 4%.

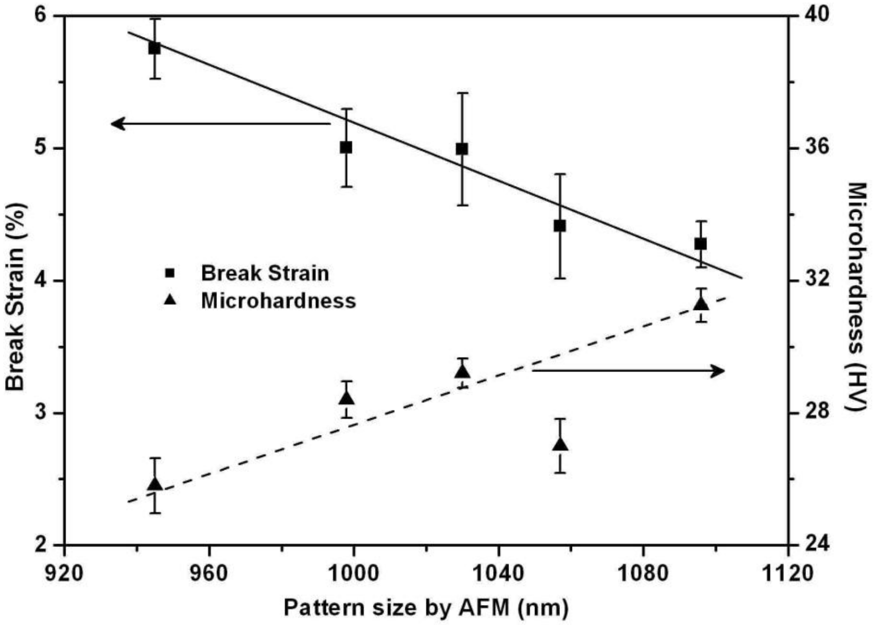

Figure 6.5 Strain values at break (%, squares) and microhardness (HV, triangles) of crosslinked PMMA samples versus pattern size on block surfaces measured by AFM.

In Figure 6.5, the break strain (squares) and the hardness (triangles) of crosslinked PMMA were plotted against the pattern size on block surface. In general, the break strain showed a good linear fit to the pattern size with the slope of about 0.01nm^{-1}. The hardness data of 0.5% - 3% EGDMA also exhibited a very good linear relationship with the pattern size on block surface, except for the big drop of PMMA-4. These curves indicate that larger pattern size can be obtained by sectioning harder and less elastic materials. Figure 6.5 provides a rough estimation to the pattern size with a known break strain in a certain region.

6.4.2 Controlled Chattering on Epoxy Samples

Aside from the study on PMMA samples, the controlled chattering experiments were also conducted with Spurrs' epoxy samples. Spurrs' epoxy is a well-known embedding medium for microtome sectioning[18]. It is generally a soft material as compared to acrylic polymers. The Vickers hardness of Spurrs' epoxy was 15 HV measured by the microhardness system. The hardness of the Spurrs' epoxy was tuned to this level for easy trimming and high quality sectioning. Under certain cutting conditions (e.g., speed, feed, clearance angle, surface shape), Spurrs' epoxy was a perfect material for generating smooth surface finishes. However, once an oscillation cutting of high speed was applied, Spurrs' epoxy also chattered. Figure 6.6 shows some TEM images of the wavy patterns on Spurrs' epoxy sections cut at different speeds with a section feed of 60 nm and an oscillation frequency of 25 kHz. Different from the work on linear PMMA[17], there was no pattern found on the epoxy thin sections at 2 mm/s speed of cut. When the cutting speed was increased to 4 mm/s and over, the epoxy sample started chattering. Further increase of the cutting speed resulted in larger patterns. The onset of cutting speed for chattering Spurrs' epoxy (≥4 mm/s) was higher than that for linear PMMA (≥2 mm/s) at the same oscillation frequency. This may be attributed to the highly crosslinked structure of epoxy, which gives a higher shearing stress resistance than physically entangled linear PMMA chains[25]. On the other hand, it was found that the patterns generated at higher cutting speeds (8-80 mm/s) were more uniform and profound. The range of 10- 80 mm/s was optimal for the selected cutting feed and oscillation frequency. A point worth mentioning is that in a conventional microtomy, chatters are usually more severe at lower cutting speeds but become milder at increased cutting speeds[26], and chatters are not observable in the range of highest cutting speeds. However, in our study the chattering phenomenon seems to function in the opposite way: higher cutting speed yielding larger and deeper pattern. The underlying mechanism can be complicated but a fact is clear: in the conventional microtomy, the source of chattering is not controlled and mostly mild, thus it could be suppressed by high cutting speed. On the contrary, in the controlled chattering, a vibrating source is applied by an external device and vibrates with a high-energy output (29.9 V).

As shown in Figure 6.6, the pattern size on the epoxy thin sections increased monotonously with the increase of cutting speed. As the cutting speed increased from 4 to 50 mm/s, the pattern size on the thin sections increased an order of magnitude from 119 to 1375 nm. If the materials mechanical property can be improved to sustain higher shearing force and the oscillation frequency can be adjusted over a larger range (below 25 kHz or beyond 40 kHz), it is possible for further extension of patterning size to a larger range.

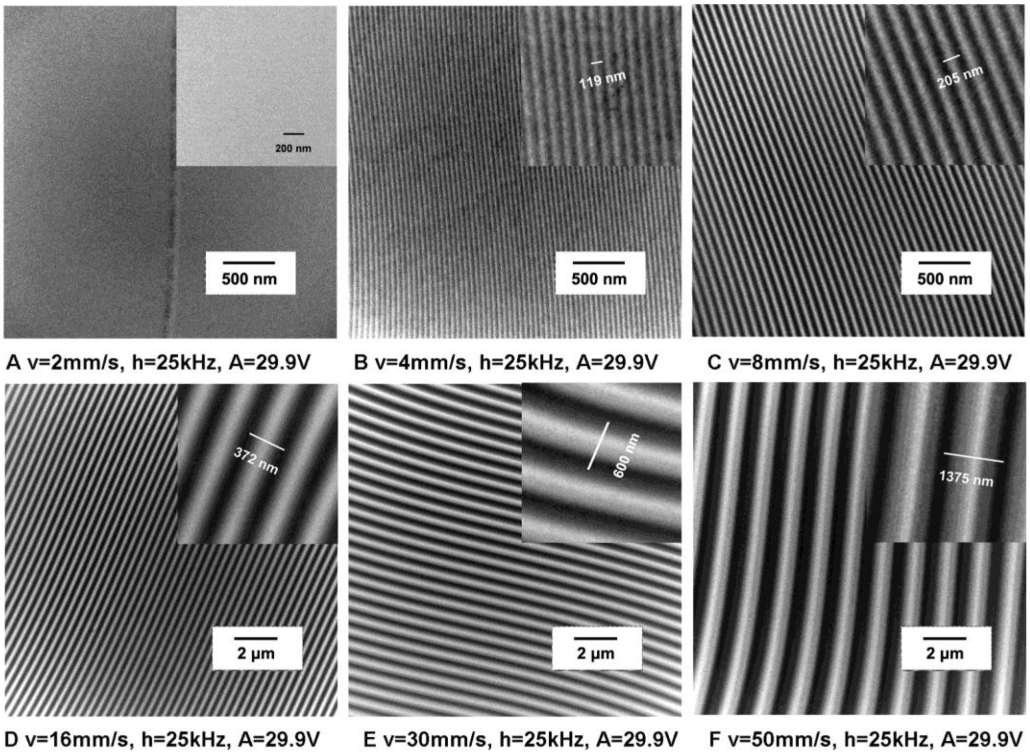

A v=2mm/s, h=25kHz, A=29.9V
B v=4mm/s, h=25kHz, A=29.9V
C v=8mm/s, h=25kHz, A=29.9V
D v=16mm/s, h=25kHz, A=29.9V
E v=30mm/s, h=25kHz, A=29.9V
F v=50mm/s, h=25kHz, A=29.9V

Figure 6.6 Representative TEM images of Spurrs' epoxy sections prepared by oscillating cutting. Cutting speed (*v*), oscillating frequency (*h*) and amplitude (*A*) are shown under each image.

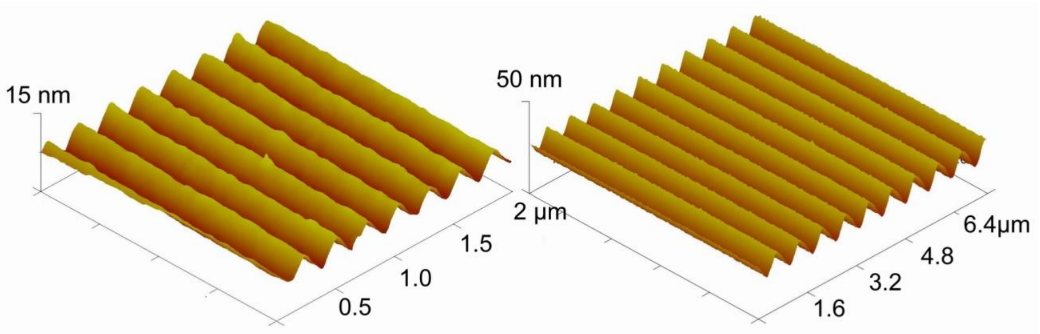

A. *v*= 8mm/s, *h*=25kHz B. *v*= 25mm/s, *h*= 25kHz

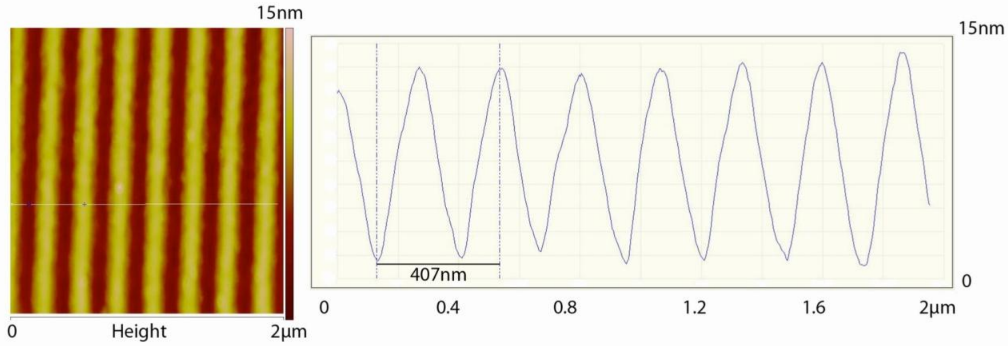

C. 2D height image and profile of the surface structure of sample A.

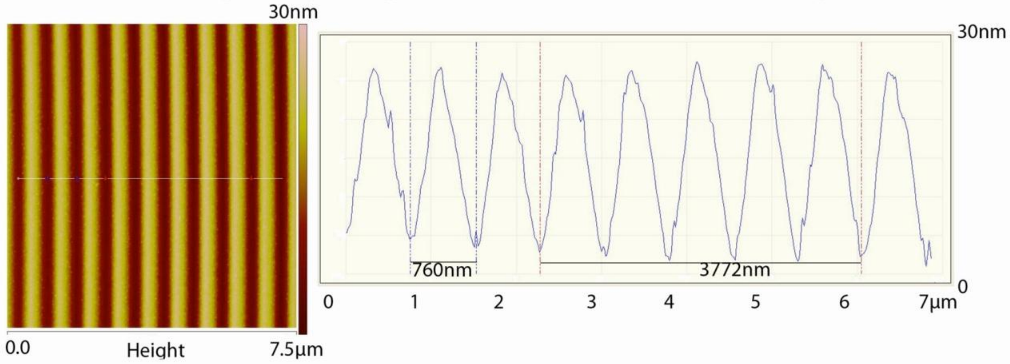

D. 2D height image and profile of the surface structure of sample B.

Figure 6.7 Representative 3D and 2D AFM images of epoxy sample surfaces prepared by controlled chattering with different cutting parameters.

The patterns on the epoxy block surfaces were also measured by AFM. Figure 6.7 shows that high-quality wavy patterns with uniform structure were generated on the block surfaces. The pattern size on the block surfaces corresponded to that of the thin sections and increased with the increased cutting speed (for a given oscillating frequency). Figure 8 shows a linear relationship between the pattern size and the cutting speed. On the other hand, the depth of patterns (amplitude) generated at higher cutting speeds also appeared to be larger, but the influence was moderate or limited. For example, in Fig. 6.7(C), the depth of the wavy structure was about 10 nm at the cutting speed of 8 mm/s (pattern size: 407 nm). In Fig. 5.7(D), the depth was about 20 nm at the cutting speed of 25 mm/s (pattern size: 760 nm). Further increase of the cutting speed resulted in very little increase in the pattern depth. The largest wavy structure on the epoxy was prepared at 80 mm/s cutting speed (25 kHz oscillation frequency) and the pattern depth was 25 nm.

6.4.3 Effect of Cutting Speed on Pattern Formation

The pattern sizes on the thin sections and block surfaces measured by TEM and AFM were plotted against the cutting speed in Figure 6.8. Both data showed linear dependence on the cutting speed. The slope of the block surface pattern was 36.9×10^{-6} s from the AFM data and that of thin sections from the TEM microscopy was 27.9×10^{-6} s. The pattern sizes obtained from PMMA-1 were included in Figure 6.8 for comparison. Similarly, the pattern size on PMMA thin films and block surfaces also showed a linear dependence on the cutting speed at 25 kHz oscillation frequency. The slope of the linear fit for the patterns on PMMA block surface was 34.5 $\times 10^{-6}$ s and that for thin film was 26.2×10^{-6} s. That is, the effect of cutting speed on chattering PMMA-1 is very similar to that of Spurrs' epoxy. It should be noted that the effect of cutting speed on pattern spanned a range of three orders of magnitude and the effect of mechanical properties discussed in the previous section was in small percents. Although the Vickers hardness, Young's modulus and break strain of Spurrs epoxy were 15 HV, 2.18 GPa and 2.31% respectively, different from those of PMMA, the pattern size experienced only small changes and its dependence on cutting speed was not significantly affected.

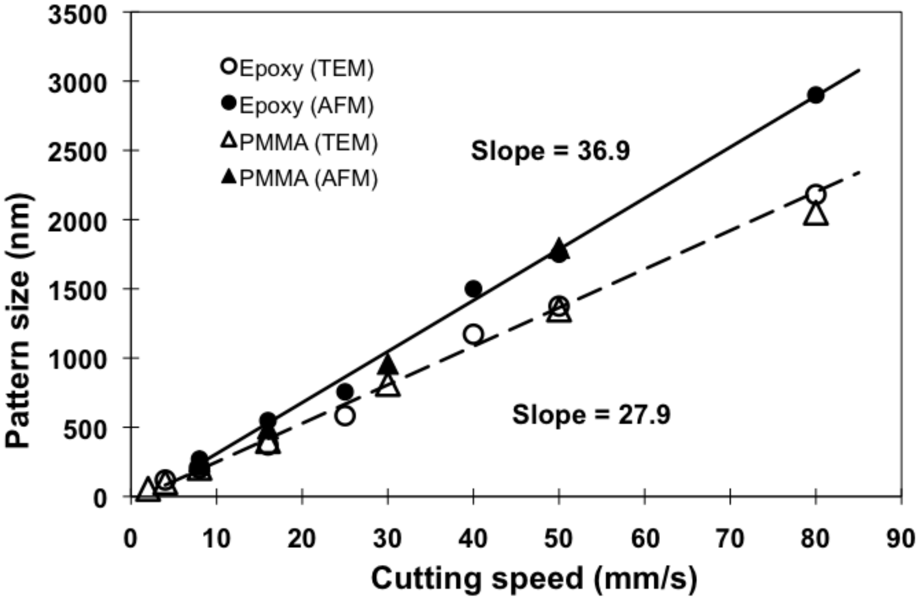

Figure 6.8 Pattern size on epoxy (filled circles) and PMMA (filled triangles) block surfaces measured by AFM and pattern size on epoxy (empty circles) and PMMA (empty triangles) thin measured by TEM. Oscillation frequency was 25 kHz. The points are experimental data and the lines are linear fitting curves.

In an attempt to relate the TEM and AFM data to cutting speed, the compression effect in machining is considered. Ideally, in a “free of compression” condition, the thin sections and their corresponding block surfaces should have the same value. However, in practice, it is almost impossible to totally eliminate the compression. The shortening of epoxy sections after cutting was found to be between 20-28% in this work with an average value of 24%. Based on the model of Almound et al., the degree of compression (C) can be estimated by:

$$C = 1-\cos(\alpha+\alpha_c) \qquad (1)$$

where α is the knife angle and α_c is the clearance angle[26]. In this study, $\alpha = 35°$ and $\alpha_c = 5\sim10°$. The compression therefore was estimated between 23% and 29% based on Eq. (1). The experimental compression result was in good agreement with the theoretical prediction. Based on the plot shown in Figure 6.8, we can roughly predict and control the pattern size on the block surface (s_b) through controlling the cutting speed (v), based on

$$s_b\ (\text{nm}) = \text{slope} \times v\ (\text{mm/s}) \qquad (2)$$

where the slope is 36.9 (s) for Spurr’s epoxy and 34.5 (s) for PMMA-1. It should be noted that the employment of Eq. (2) is under the condition of the oscillation frequency of 25 kHz and the section feed of 60 nm. Varying either oscillation frequency or section feed will result in a change in the cutting speed dependence of the pattern size. Combining Eq. (1) with Eq. (2) yields Eq. (3) that allows us to estimate the pattern size on the thin sections (s_s),

$$s_s\ (\text{nm}) = \text{slope} \times \cos(\alpha+\alpha_c)\ v\ (\text{mm/s}) \qquad (3)$$

To further investigate the effect of cutting parameters on the surface patterning in controlled chattering, the oscillation knife with a larger range of frequency is required.

6.5 Conclusions

A variety of long-range and large-area uniform wavy patterns at nano- to micrometer levels were fabricated by the developed controlled chattering technology from representative thermoset and thermoplastic polymers. The polymers used for demonstration included polymethyl methacrylate (PMMA) modified by ethylene glycol dimethacrylate (EGDMA) as crosslinker, as well as Spurrs' epoxy. In the study of crosslinked PMMA samples, the pattern size was found to be dependent on the degree of crosslinking at a set of fixed cutting parameters. At low crosslinking levels (≤3wt% of EGDMA), increasing EGDMA resulted in an increase in the pattern size on both of the PMMA thin film and block surface. However, the pattern size showed a slight decrease with further increase in the EGDMA amount to 4wt%. The tensile tests showed that the pattern size was linearly dependent on the break strain of the crosslinked PMMA as well as the hardness of the material in the low crosslinking range. In studying the effect of cutting speed on pattern size, it was found that for both PMMA (1% EGDMA) and Spurrs' epoxy samples, the pattern size on the block surfaces was linearly proportional to the cutting speed at a fixed frequency of oscillation. The pattern size on the thin sections was reduced, with the percentage of reduction in agreement with the shortening of section length. The pattern size on the thin sections was correlated to that on the block surfaces and it could be estimated from the latter data with the given knife and clearance angles.

6.6 References

1. Jacobs, H. O.; Whitesides, G. M. *Science* **2001,** 291, (5509), 1763-1766.
2. Xia, Y. N.; Kim, E.; Zhao, X. M.; Rogers, J. A.; Prentiss, M.; Whitesides, G. M. *Science* **1996,** 273, (5273), 347-349.
3. Zhao, X. M.; Stoddart, A.; Smith, S. P.; Kim, E.; Xia, Y.; Prentiss, M.; Whitesides, G. M. *Adv. Mater.* **1996,** 8, (5), 420-424.
4. Grainger, D. W. *Nat. Nanotechnol.* **2009,** 4, (9), 543-544.
5. Kershner, R. J.; Bozano, L. D.; Micheel, C. M.; Hung, A. M.; Fornof, A. R.; Cha, J. N.; Rettner, C. T.; Bersani, M.; Frommer, J.; Rothemund, P. W. K.; Wallraff, G. M. *Nat. Nanotechnol.* **2009,** 4, (9), 557-561.
6. Kim, S. O.; Solak, H. H.; Stoykovich, M. P.; Ferrier, N. J.; de Pablo, J. J.; Nealey, P. F. *Nature* **2003,** 424, (6947), 411-414.
7. Quake, S. R.; Scherer, A. *Science* **2000,** 290, (5496), 1536-1540.
8. Gates, B. D.; Xu, Q. B.; Stewart, M.; Ryan, D.; Willson, C. G.; Whitesides, G. M. *Chem. Rev.* **2005,** 105, (4), 1171-1196.
9. Xia, Y. N.; Whitesides, G. M. *Annu. Rev. Mater. Sci.* **1998,** 28, 153-184.
10. Perl, A.; Reinhoudt, D. N.; Huskens, J. *Adv. Mater.* **2009,** 21, (22), 2257-2268.

11. Itani, T.; Wakamiya, W.; Cashmore, J.; Gower, M. *Microelectron. Eng.* **2003,** 67-8, 39-46.
12. Templin, M.; Franck, A.; DuChesne, A.; Leist, H.; Zhang, Y. M.; Ulrich, R.; Schadler, V.; Wiesner, U. *Science* **1997,** 278, (5344), 1795-1798.
13. Hong, S. W.; Xia, J. F.; Lin, Z. Q. *Adv. Mater.* **2007,** 19, (10), 1413-1417.
14. Hong, S. W.; Byun, M.; Lin, Z. Q. *Angew. Chem.-Int. Edit.* **2009,** 48, (3), 512-516.
15. Gates, B. D.; Xu, Q. B.; Love, J. C.; Wolfe, D. B.; Whitesides, G. M. *Ann. Rev. Mater. Res.* **2004,** 34, 339-372.
16. Qin, D.; Xia, Y. N.; Whitesides, G. M. *Nat. Protoc.* 5, (3), 491-502.
17. Gu, H. Y.; Zhang, J. W.; Faucher, S.; Zhu, S. P. *Nanotechnology* **2010,** 21, (35), 355302.
18. Spurr, A. R. *Journal of Ultrastructure Research* **1969,** 26, 31-43.
19. Cook, W. D.; Moopnar, M. *Biomaterials* **1990,** 11, (4), 272-276.
20. Zhu, S.; Tian, Y.; Hamielec, A. E.; Eaton, D. R. *Polymer* **1990,** 31, (1), 154-159.
21. Zhu, S.; Tian, Y.; Hamielec, A. E.; Eaton, D. R. *Polymer* **1990,** 31, (9), 1726-1734.
22. Zhu, S.; Hamielec, A. E. *Macromolecules* **1992,** 25, (20), 5457-5464.
23. Atkinson, J. R.; Brinson, G. *Metals Forum* **1984,** 7, (3), 131-145.
24. Deb, S.; Vazquez, B.; Bonfield, W. *J. Biomed. Mater. Res.* **1997,** 37, (4), 465-473.

25. Kobayashi, A. *Machining of plastics. McGraw-Hill Book Company, New York.* **1967,** 14-20.

26. Al-Amoudi, A.; Studer, D.; Dubochet, J. *J. Struct. Biol.* **2005,** 150, (1), 109-121.

Chapter 7 A One-step Approach for the Fabrication of Polymer and Metal Nanowires

This chapter is reproduced based on the publication of Gu H. and Zhu S. A one-step approach for the fabrication of polymer and metal nanowires. *Nanotechnology* **2011**, 22, 265355. Copyright © Institute of Physics and IOP Publishing Limited 2007 - 2011.

Author Contributions: Hongyan Gu performed the lab experiments, characterizations and manuscript preparation. Dr. Shiping Zhu supervised this work and participated in manuscript revision.

7.1 Abstract

The fabrication of one-dimensional (1D) polymer and metal nanowires were obtained in a one-step mechanical approach. This approach is based on a controlled chattering process at the cutting edge of an oscillating diamond knife to conduct wavy cutting. Consecutive shallow wavy cuttings at different phases yield uniform ultra-long nanowire products with controlled lateral dimensions in the range of sub-100 nanometers to micrometers. The morphologies and lateral dimensions of the nanowires can be tuned through phase alignment, cutting depth and cutting speed; as demonstrated in this paper through examples of its application to polymethyl methacrylate, aluminum and copper. This facile one-step "cutting-edge" method is robust, clean, involves no chemicals, and can be readily scaled up with precision machining for long-range and large-area fabrications.

7.2 Introduction

One-dimensional (1D) nanomaterials are the "building blocks" for the development of nano-scale devices and circuits, and have applications in photonics, sensors, electronics, and other nano-photovoltaic parts. In fundamental research, 1D nanomaterials are also of great interest for studying extraordinary physical or electrical properties under confinement[1-3]. State-of-the-art strategies of 1D nanostructure fabrication can be mainly divided into two categories, bottom-up or top-down routes[4,5]. Bottom-up routes include directed self-assembly[4,6], chemical vapor deposition[7,8], electro-spinning[9-11], or other template based approaches[12-15]; and are capable of producing unusual heterogeneous nanostructures with lateral dimensions down to a few nanometers' in scale. Since the template removal procedure can be tedious and costly for most template-involved techniques, the "no-template" self-assembly approach is more favorable in terms of simplicity. However, some of the "no-template" self-assembly approach, such as conjugated polymer growing in one direction[16, 17], is still at an early stage of its development and the control of morphologies is challenging. Another limitation for bottom-up routes is that the wires produced by this means are usually short (≤100 µm). Top-down techniques have been highly developed in the recent years and the limit of dimension has been significantly reduced to < 20 nm[18]. The major technique for controlled 1D structure fabrication in this category is the chemical etching approach[19], which is primarily suitable for elemental semiconductor materials. Top-down technologies normally require multiple-step operations, involving lithography, thin film deposition/removal and chemical or ion etching[20-22]. It has become a general nanofabrication method that is able to achieve high throughput as well as precise control on a variety of materials. However, the wide applicability of this category is usually realized at high costs incurred from additional procedures such as functionalization of mold/substrate or use of specific deposition facilities. For successful future large-scale applications, we believe that simplicity, bulk production and universal application in a variety of materials are the key factors.

Our recent study on ultramicrotomy has lead to the development of a new nanofabrication technology - “Controlled Chattering”[23]. This technique was inspired by the “chattering” mechanism typically found in an unstable cutting process; where the vibration of cutting tool or work piece leads to unexpected wavy surfaces. Since those vibrations are not controlled, the wavy structures are normally random. Numerous efforts were made in the past to avoid such unwanted chatters. However, by applying a modified diamond knife attached to a piezo transducer, we found that wavy patterns with uniform and tunable sizes could be fabricated through simple cutting. The size of the patterns was tunable from nano- to micrometer scale by controlling the cutting speed and oscillation frequency.

In our previous study, it was found that for patterns with different sizes, the amplitude of wavy structures also varied from a few nanometers to tens of nanometers[24]. In microtomy, depth of cut can be referred to “section feed”. The section feed is controllable from a few nanometers to micrometers and is determined by incremental advancing of sample holder towards knife (perpendicular to cutting direction) before each cut. In fact, the ultramicrotome is so delicately designed that each step of increment can be as small as 1 nm[25]. When sections are prepared for different microscopic facilities, the section feed is normally between 50 nm-500 nm. We used 60 nm section feed for most of the experiments in our previous study. Occasionally, we observed that the diamond knife cut discontinuous chips. The cracks on the chips appeared straight and were normally located at valleys of the wavy structures. It suggested that the vibrating knife under certain conditions was not able to cut deep enough to form a uniform section. On the other hand, it implies that there is a possibility of cutting 1D nanostructures from these wavy surfaces by careful adjustment of the cutting parameters. Such a process should be akin to a combination of chattering and trimming, in which the edge of knife gets in contact with the wavy surface periodically.

In this paper, we report the proof of concept and demonstrate that by adjusting the phase alignment of two concessive wavy cuttings or controlling the depth of cut-to-amplitude ratio of wavy structures, 1D nanostructures can be successfully fabricated by using a simple mechanical method such as controlled chattering. This mechanical method does not involve any chemical reactions, template preparation/removal or other costly post-treatment methods. The nanowires (nanorods and nanoribbons) fabricated in this work can easily achieve lengths up to a millimeter. Concurrently, this method can be readily scaled up through precision machining for even longer-range fabrications.

7.3 Experimental Section

7.3.1 Materials

A PMMA sample containing 1wt% of ethylene glycol dimethacrylate (EGDMA) was casted as described before[23]. Copper (99.999%) and aluminum (99.99%) bars were purchased from Sigma-Aldrich.

7.3.2 Controlled Chattering Operation

The controlled chattering experiments were conducted on a Leica UCT ultramicrotome equipped with an oscillating diamond knife (DIATOME®, knife edge: 3 mm, knife angle: 35°, frequency: 25~45 kHz, amplitude: variable from 0-30 V). The cutting speed was set to 30mm/s and 8mm/s for sectioning PMMA samples and metals, respectively. The sample surface was pre-trimmed with a razor blade into a 1 mm ×1 mm to 2 mm ×1 mm (width ×length) area for sectioning. The clearance angle for sectioning was set to 6°. The input voltage for piezo transducer was 29.9 V, and the oscillation frequency was 40 kHz for all the sectioning in this work. Ribbons of PMMA and metal sections were picked up from collecting boat of the microtome, and were placed on Formvar coated 200-mesh copper grids. PMMA sections on Formvar supported copper grids were coated with a thin layer of carbon before TEM imaging.

7.3.3 Transmission Electron Microscopy

The Transmission Electron Microscopy (TEM) observations were conducted on JEOL 1200EX at an accelerating voltage of 80 kV. The images were recorded with a CCD camera at various magnifications.

7.3.4 Atomic Force Microscopy

Atomic Force Microscopy (AFM) images were taken on the Veeco Dimension Icon Atomic Force Microscope equipped with Veeco TESPA probe (Tip radius: 8 nm) on the tapping mode.

7.4 Results and Discussion

7.4.1 Effect of Phase Alignment on Nanostructure Formation

The successful operation of controlled chattering on polymeric materials such as PMMA and epoxy has been reported previously for the fabrication of wavy nanopatterns.[23] In this work, a PMMA sample crosslinked with 1wt% of EGDMA was used as the first example to fabricate 1D nanostructures by controlled chattering. The controlled chattering conducted on the crosslinked PMMA was: section feed = 60 nm, cutting speed = 50 mm/s and oscillation frequency = 40 kHz. The resultant PMMA surface was examined by AFM and a 3D image is shown in Figure 7.1. According to AFM measurements, the wavy structures created on the PMMA block surface were about 1.14 μm in wavelength and 56 nm in amplitude. A consecutive controlled chattering sectioning in parallel generated a thin wavy film that was demonstrated in our previous practice on PMMA at 25 kHz oscillation frequency. Under such a condition, the thin film is expected to have uniform thickness and can be as thin as the given cutting depth. A schematic illustration is shown in Figure 7.2(A), where the dark blue region represents the sample block and the light blue region is the newly cut chip (film-like structure), and the black line between is the trajectory of the wavy cut.

Our hypothesis was that if the wave phase of a concessive cut is misaligned with the previous cut typically in 0-1/4 or 3/4-1 wavelength, and the section feed is less than the amplitude of the wavy structure; the knife-edge is expected to generate separated ribbon-like structures rather than continuous chips (Figure 7.2(B)). The term “ribbon-like” denotes that the edge thickness of the structure is smaller than the middle. Furthermore, by using a similar shallow-cutting process with cutting depth smaller than wave amplitude, separated rod-like wires can be generated if the misalignment of two concessive wavy cuts is about 1/2 of a wavelength (Figure 7.2(C)).

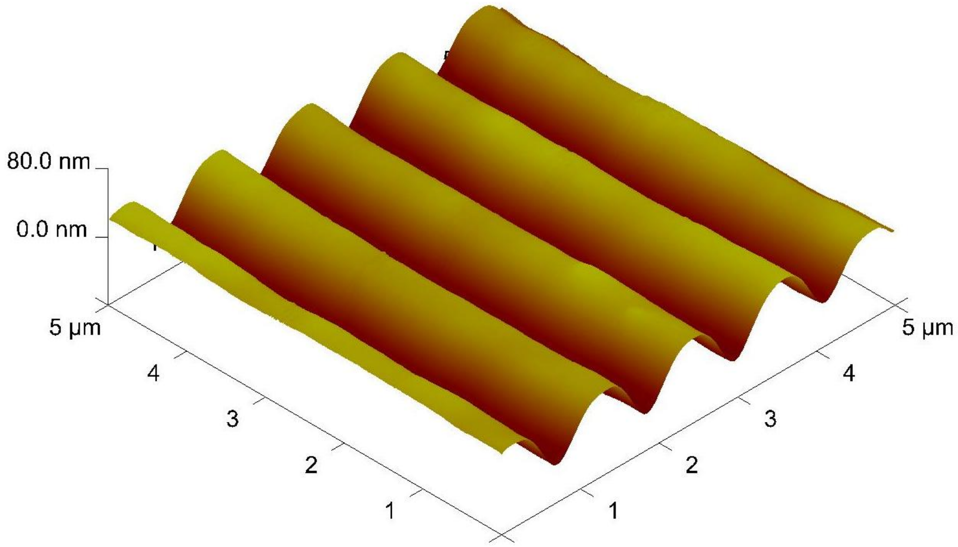

Figure 7.1 3D-AFM image of a PMMA wavy surface prepared by controlled chattering at 50 mm/s cutting speed, 40 kHz oscillation frequency and 29.9 V input. Wavy structure dimensions: wavelength= 1.14 μm, amplitude= 56 nm.

The chip structures corresponding to Figure 7.2 (A, B and C) were observed in the sections of PMMA chattered at 50 mm/s speed and 40 kHz with a cutting feed of 60 nm. Representative TEM images are shown in Figure 7.2(D, E and F). The wavelength of wavy structures in Figure 7.2(D) was 750 nm by TEM, which was about 34% smaller than that of the block surface (1.14 μm). The large reduction in wavelength of the thin section reveals that the compression in such a high-speed high-frequency cutting was considerably large[26]. In our previous experiments at 25 kHz oscillation frequency, the evidence of 1D structure formation was not found in controlled chattering. The operation at higher oscillation frequency appeared to be more prone to generate separated 1D structures. In sectioning crosslinked PMMA samples, when the oscillation frequency was raised from 25 kHz to 40 kHz at a cutting speed of 50mm/s and a section feed of 60 nm, discontinuous chips started to be generated. As shown in Figure 7.2(E), nanoribbons were generated when sectioning PMMA sample at the oscillation frequency of 40 kHz. The width of the nanoribbons was measured 750 nm in average, which was about the same size of the compressed wavy structure and was also 34% less than the wavelength on the original block. Depending on the degree of wavy phase alignment, 1D chips with different structures were also generated. Figure 7.2(F) shows the rod-like nanowire structures cut from the same PMMA sample with oppositely aligned phases in the concessive oscillation cuts. The average width of nanorods was 720 nm under TEM. It should be pointed out that there is no function available yet with the current microtome facilities to precisely tune the phase alignment. The phase alignment in this work was achieved by a trial-and-error approach.

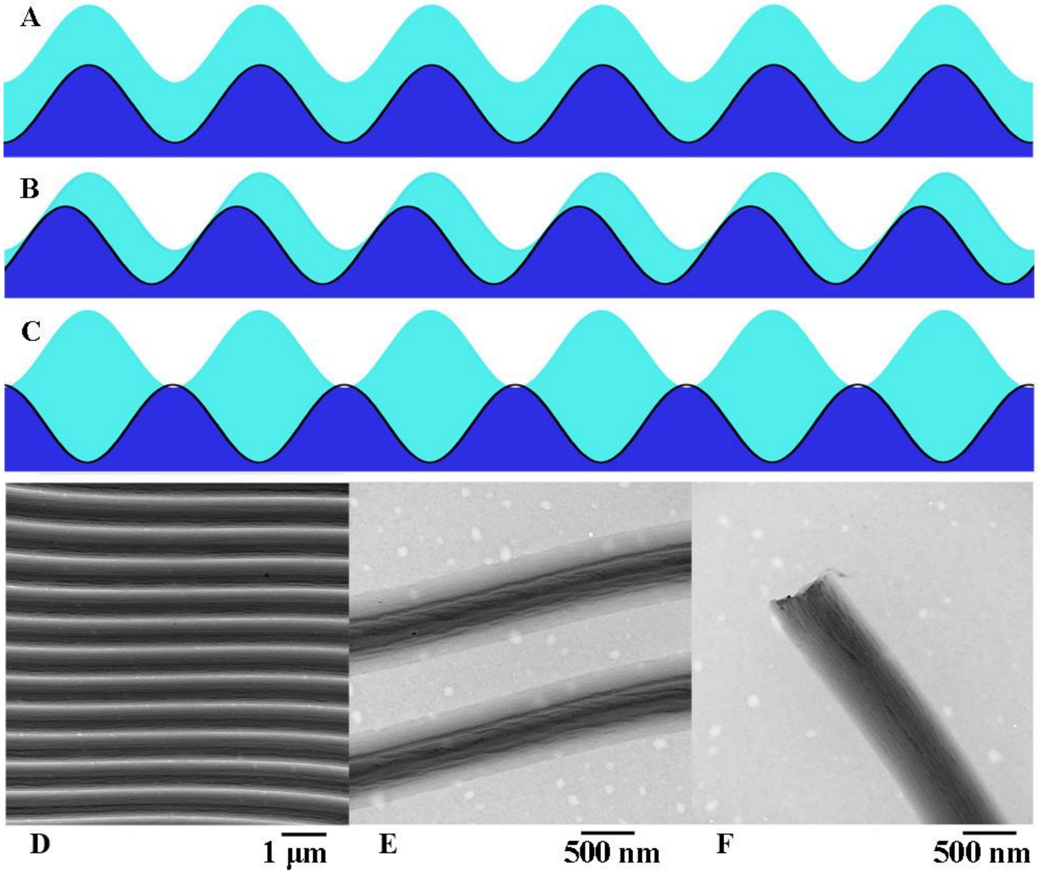

Figure 7.2 Schematic and TEM images showing various PMMA structures can be formed in Controlled Chattering. (A) two parallel cuts with a perfect wave phase alignment generate a uniform wavy thin film (light blue area). (B) a small offset in the cutting phase alignment generates nanoribbons. (C) two oppositely aligned cuts of controlled chattering generate nanorods. (D) TEM images of the PMMA wavy film surface. (E) ribbon-like structure of PMMA. (F) rod-like structure of PMMA. Cutting parameters are: section feed 60 nm, cutting speed 80 mm/s cutting, oscillation frequency 40 kHz for (D)- (F).

7.4.2 Effect Cutting Depth and Cutting Speed on Nanostructure formation

In addition to the phase alignment, there are other parameters that affect the structure of chips cut from controlled chattering. The section feed determines the depth of a knife cut into the work piece. A large section feed assures continuous chips while a small feed (shallow cut) generates discontinuous chips. In a shallow cut, the feed also affects the size of 1D structures: the shallower the cut, the thinner the wires. The size (wavelength and amplitude) of original wavy structures on block surface determines the maximum width of 1D structures. Since the knife cuts only a portion of the material off from the wavy surface, the width of nanowires must be smaller than the wavelength of the original waves. Furthermore, a surface with larger wave, both in wavelength and amplitude, is more likely to get a partial cut at a certain depth, generating separated wires. It also allows for a wider selection of the cutting depth. Our previous work showed that the wavelength on block surface could be fine tuned in the range of tens of nanometers to micrometers through varying the cutting speed. The 1D structure size can therefore also be correlated to the applied cutting speed.

Chattering experiments at different cutting depths and cutting speeds were conducted with PMMA blocks. In the first two runs, the cutting speed and oscillation frequency were fixed. The section feeds were 20 nm and 60 nm, respectively. The cutting mechanism is illustrated in Figure 7.3(A) and (B). The amplitude and wavelength on the original block surface were 56 nm and 1140 nm. When the section feed was set to 20 nm, the nanowires had an average width of 235 nm (Figure 7.3(D)). That is, under such conditions, the diamond knife cuts only about 20% of the original wavy structure from the block surface. When the section feed was increased to 60 nm, which was close to the amplitude of the original structure, the width of nanowires was increased to 720 nm (Figure 7.3(E)), approximately 63% of the wavelength of the original structure. Although when the cutting feed was set to 60 nm, which was slightly larger than the amplitude of wavy structures (56 nm), the actual section depth did not maintain. This deviation could be caused by the compression in the high-speed cutting as well as elastic deformations of the materials. It could possibly explain the partial cut of nanowires at 60 nm’s feed. In the other two experiments, the section feed and oscillation frequency were fixed to 60nm and 40 kHz, while the cutting speed was varied from 50 mm/s to 80 mm/s. The lower speed generated a wavy pattern of 1140 nm in wavelength on the block surface while the higher speed gave 1820 nm. Figures 7.3(E) and 7.3(F) show TEM images of the 1D structures. The width of PMMA microwires was 720 nm in Figure 7.3(E) and 1150 nm in Figure 7.3(F). The wavy patterns having larger wavelength and amplitude yielded thicker and wider 1D wires at a given section depth.

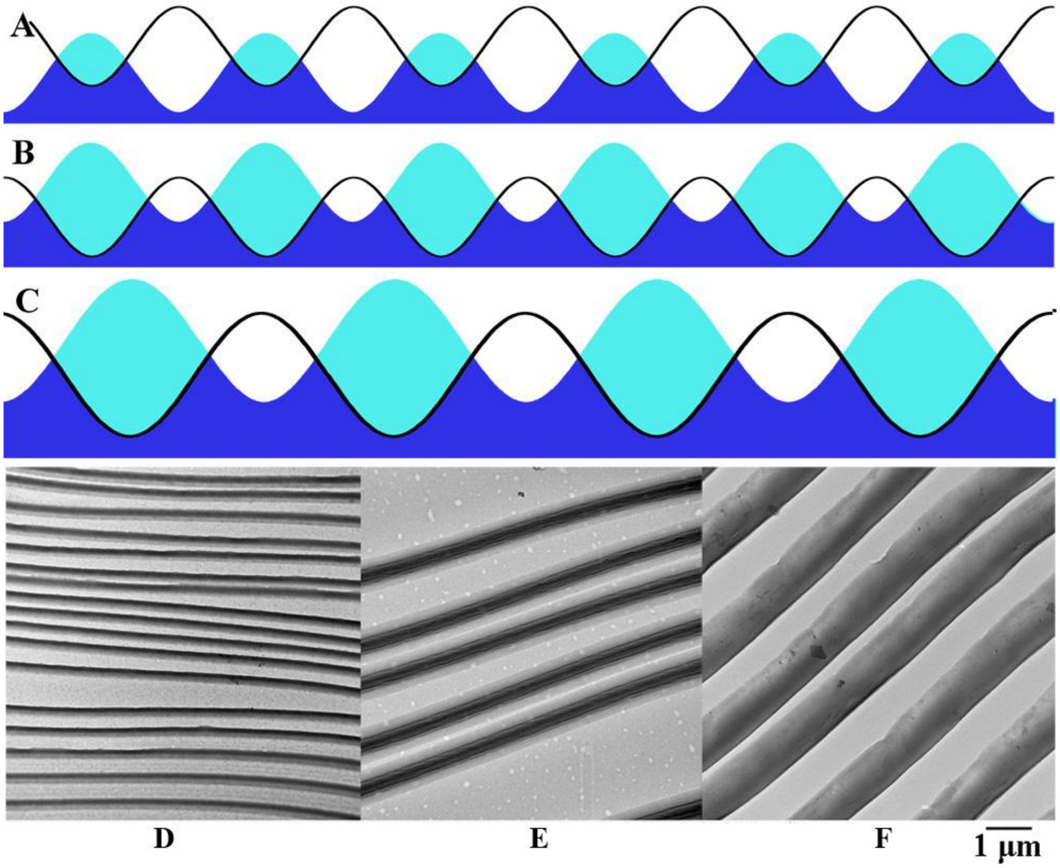

Figure 7.3 Schematic cross sections of the wavy sample surfaces (light blue area), the new oscillating cutting trajectory, and the resulted surface after controlled chattering (A)-(C). The size of nanowires can be adjusted by adjusting the cut depth. (A) a shallow cut generates small nanowires; (B) a deeper cut yields bigger nanowires. (C) larger surface structures allows for larger wires being cut. And TEM images of PMMA nano- or microwires prepared by controlled chattering at different parameters. (D) section feed 20 nm and cutting speed 50 mm/s; (E) section feed 60 nm and cutting speed 50 mm/s; (F) section feed 60 nm and cutting speed 80mm/s.

7.4.3 Application of Controlled Chattering on Metals

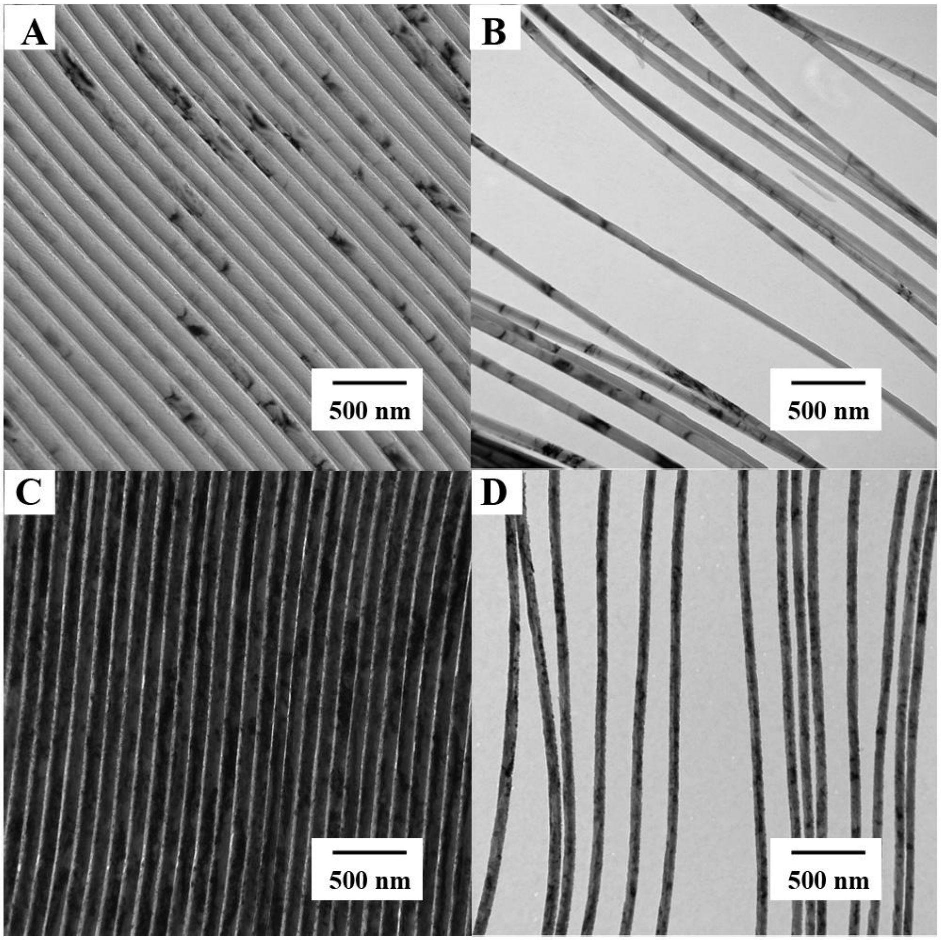

Figure 7.4 TEM images of aluminum and copper sectioned by controlled chattering. (A) aluminum wavy film; (B) aluminum nanowires; (C) copper wavy film; (D) copper nanowires. Cutting parameters are: section feed 20 nm, cutting speed 8 mm/s and oscillation frequency of 40 kHz.

Another exciting development in this controlled chattering is its applicability in the fabrication of metal nanowires. Realizing that conductive nanowires are highly demanded for applications in miniaturized electronics and lab-on-chip devices, we also extended the controlled chattering to some conductive metals such as aluminum and copper. These two metals were chosen because firstly they have the medium softness suitable for machining; secondly, they are among the most-often used conductive materials in the electronics industry. We used a cutting speed of 8 mm/s and an oscillation frequency of 40 kHz for the first trial. It should be noted that the cutting speed used for metals are lower than that for polymers. This was to reduce tool wear during metal machining thus maintain a good condition of the diamond knife. Also, we were aimed to downsize wire thickness for which smaller cutting speeds or section feed should be used. The section feed was set to 20 nm, at the same level of the wavy structure on the block surface. Representative TEM images of aluminum and copper wavy films and their nanowires prepared by the controlled chattering method are shown in Figure 7.4. The wavy structure of the aluminum thin film was about 155 nm in wavelength (Figure 7.4(A)), and the width of nanowires was about 80nm in average (Figure 7.4(B)). The differences in pattern sizes on aluminum and copper chattered at the same parameters could be attributed to their different mechanical properties such as hardness, stiffness, ductility, etc, which will be further investigated in our future study. In comparison, the wavelength of wavy film and the width of nanowires chattered from a copper block under the same condition were more similar, which were about 80 nm and 70 nm, respectively. As demonstrated in the previous section for PMMA, the size of metal wires could also be controlled through adjusting cutting parameters or depth (please see Appendix B.). Since the slowest applicable cutting speed for controlled chattering is limited, given an oscillator that provides a higher oscillation frequency, we believe it is possible to further reduce the nanowire size to < 50 nm.

In terms of productivity, it is worth mentioning that the controlled chattering by a microtome facility is highly automated and can be carried out in a continuous mode provided the conditions are well maintained. The time-consuming step is the preparation of samples that must be pre-polished, manually trimmed into a regular shape and aligned to the fixed knife. This takes about 20 - 40 min for an experienced operator. However, once the sample is aligned, operation of the automated cutting, e.g. on a 2 mm×2 mm surface, takes less than 1 sec. For continuous and repeated cutting, the time for batch preparation would be less significant.

7.5 Conclusions

In conclusion, we demonstrated the fabrication of polymer and metal nanowires by a one-step “cutting-edge” method based on the controlled chattering. The experiments were carried out with an ultramicrotome facility that offers extraordinary precision control and reproducibility. This facile fabrication process can be completed in minimal time and involved no chemicals and no template preparation/removal. The experiments on PMMA, aluminum and copper were successfully conducted for the proof of concept. The dimension of wires could be tuned from sub-100 nm to micrometers under different operation parameters. The key parameters for the control of wire size included section feed, cutting speed and oscillation frequency. It is anticipated that this method would allow for the fabrication of ultra-long nanowires up to a few millimeters or higher, given an adequately large microtome knife. It has many advantages over existing technologies for its simplicity in operation, low cost of facility, no chemical reaction or pollution, easy control over size, long-range and large area structures, and general applicability to a variety of materials.

7.6 References

1. Tian, M. L.; Wang, J.; Zhang, Q.; Kumar, N.; Mallouk, T. E.; Chan, M. H. W. *Nano Lett.* **2009,** 9, (9), 3196-3202.
2. Wang, J.; Singh, M.; Tian, M.; Kumar, N.; Liu, B. Z.; Shi, C.; Jain, J. K.; Samarth, N.; Mallouk, T. E.; Chan, M. H. W. *Nat. Phys.* **2010,** 6, (5), 389-394.
3. Zhao, X. Y.; Wei, C. M.; Yang, L.; Chou, M. Y. *Phys. Rev. Lett.* **2004,** 92, (23), 236805-1-4.
4. Schenning, A.; Meijer, E. W. *Chem. Commun.* **2005**, (26), 3245-3258.

5. Baca, A. J.; Ahn, J. H.; Sun, Y. G.; Meitl, M. A.; Menard, E.; Kim, H. S.; Choi, W. M.; Kim, D. H.; Huang, Y.; Rogers, J. A. *Angew. Chem.-Int. Edit.* **2008,** 47, (30), 5524-5542.
6. Hoeben, F. J. M.; Jonkheijm, P.; Meijer, E. W.; Schenning, A. *Chem. Rev.* **2005,** 105, (4), 1491-1546.
7. Wagner, R. S.; Ellis, W. C. *Appl. Phys. Lett.* **1964,** 4. , 89-90.
8. Hanrath, T.; Korgel, B. A. *J. Am. Chem. Soc.* **2002,** 124, (7), 1424-1429.
9. Pinto, N. J.; Johnson, A. T.; MacDiarmid, A. G.; Mueller, C. H.; Theofylaktos, N.; Robinson, D. C.; Miranda, F. A. *Appl. Phys. Lett.* **2003,** 83, (20), 4244-4246.
10. MacDiarmid, A. G.; Jones, W. E.; Norris, I. D.; Gao, J.; Johnson, A. T.; Pinto, N. J.; Hone, J.; Han, B.; Ko, F. K.; Okuzaki, H.; Llaguno, M. *Synth. Met.* **2001,** 119, (1-3), 27-30.
11. Li, D.; Xia, Y. N. *Nano Lett.* **2003,** 3, (4), 555-560.
12. Virji, S.; Fowler, J. D.; Baker, C. O.; Huang, J. X.; Kaner, R. B.; Weiller, B. H. *Small* **2005,** 1, (6), 624-627.
13. Virji, S.; Kaner, R. B.; Weiller, B. H. *Chem. Mat.* **2005,** 17, (5), 1256-1260.
14. Nuraje, N.; Su, K.; Yang, N. L.; Matsui, H. *ACS Nano* **2008,** 2, (3), 502-506.
15. Lee, K. B.; Lee, S. M.; Cheon, J. *Adv. Mater.* **2001,** 13, (7), 517-520.

16. Tran, H. D.; Wang, Y.; D'Arcy, J. M.; Kaner, R. B. *ACS Nano* **2008,** 2, (9), 1841-1848.

17. Huang, J. X.; Kaner, R. B. *J. Am. Chem. Soc.* **2004,** 126, (3), 851-855.

18. Melosh, N. A.; Boukai, A.; Diana, F.; Gerardot, B.; Badolato, A.; Petroff, P. M.; Heath, J. R. *Science* **2003,** 300, (5616), 112-115.

19. Baca, A. J.; Meitl, M. A.; Ko, H. C.; Mack, S.; Kim, H. S.; Dong, J. Y.; Ferreira, P. M.; Rogers, J. A. *Adv. Funct. Mater.* **2007,** 17, (16), 3051-3062.

20. Edelstein, A. S.; Cammarata, R. C. Nanomaterials: synthesis, properties and applications, 2nd edition (Institute of Physics Publishing, Bristol, UK **1998**.

21. Ko, H. C.; Baca, A. J.; Rogers, J. A. *Nano Lett.* **2006,** 6, (10), 2318-2324.

22. Jung, G. Y.; Johnston-Halperin, E.; Wu, W.; Yu, Z. N.; Wang, S. Y.; Tong, W. M.; Li, Z. Y.; Green, J. E.; Sheriff, B. A.; Boukai, A.; Bunimovich, Y.; Heath, J. R.; Williams, R. S. *Nano Lett.* **2006,** 6, (3), 351-354.

23. Gu, H. Y.; Zhang, J. W.; Faucher, S.; Zhu, S. P. *Nanotechnology* **2010,** 21, (35), 355302.

24. Gu, H. Y.; Faucher, S.; Zhu, S. P. *Polymer* **2011,** 52, (9), 2525-2031.

25. Xu, Q. B.; Rioux, R. M.; Dickey, M. D.; Whitesides, G. M. *Accounts Chem. Res.* **2008,** 41, (12), 1566-1577.

26. Al-Amoudi, A.; Studer, D.; Dubochet, J. *J. Struct. Biol.* **2005,** 150, (1), 109-121.

Chapter 8 Contributions, Perspectives and Recommendations for Future Work

8.1 Major Contributions

This work detailed in this thesis has provided significant contributions to the development of polymer surface engineering, and specifically towards surface chemistry and topography design. This includes the development and demonstration of two new technologies, *surfadditives for in-mold surface modification* and *controlled chattering* for *surface patterning*. Both technologies are based on unconventional approaches and involve a single step. They do not require high capital cost facilities, and are highly versatile and easily implemented. They are also very promising when considering scaling up for large-scale applications.

8.1.1 Copolymer Surfadditive for Polymer Surface Chemistry Modification

In Chapter 3, block copolymers having the "head-neck-body" structure were synthesized and applied as surfadditives for surface modification and functionalization. Fluorinated segments and triethoxy silane functional groups were incorporated as a “head” or “neck” of the surfadditive molecule. This type of surfadditives targeted applications in the molding of acrylic plastics so that a PMMA “body” was constructed to achieve strong adhesion. The surface migration of such surfadditive molecules was due to the low surface energy of fluorinated “head” or “neck”. After migration, the triethoxy silane segments attached to fluorinated segments were also brought to the surface of the polymer composite, providing functionality for further modification or crosslinking. Conventionally, tri-block copolymers were synthesized in multiple steps by chain extension; however, we prepared block copolymer surfadditives in a one-pot process via ATRP. Although chain extension in multi-steps provides better control of chemical composition than in a one-pot process, it is inherently more costly. Our approach appears to be an economic alternative where satisfactory results could be obtained at a much lower cost. In the application of surfadditives in PMMA injection molding, an optimal operation temperature of 180°C was found and the effect of surfadditive loading on surface modification was studied. In the cell casting process, the surface migration results obtained from different molds (fluorinated polymer and glass) and different molecular structures were compared.

8.1.2 Magnetic Surfadditive for Surface Hardness Modification

The second type of surfadditives, based on magnetic particles, was designed in part to solve the low migration rate problem of polymeric surfadditives. It was found that the diffusion of polymeric chains in a polymer melt was very slow. To have sufficient surface coverage of such molecules, the process time must be in the order of tens of hours, which is not realistic for industrial operations. In comparison, the magnetic surfadditive appears promising since it could be effectively manipulated by a magnetic field. In order to develop a type of surfadditive that can be used to increase the scratch resistance of acrylic plastics, we prepared magnetic nanoparticles consisting of an iron core and a hybrid shell that contains nanosilica cages (POSS) and PMMA brushes. The hybrid material was grafted by surface-initiated ATRP. The PMMA segments were introduced to increase the compatibility of particles with the bulk matrix. As expected, the migration efficiency of magnetic surfadditive was significantly enhanced as compared to the fluorinated copolymer. With only 1wt% of magnetic surfadditive in the casting of PMMA board under a magnetic field, the concentration of particles was increased about 50 times in a 100 μm surface layer. This particle-enriched layer showed a 30% hardness improvement based on micro-indentation tests. This part of the thesis work demonstrated the feasibility of using functional magnetic particles as additives to modify a polymer surface, which has not been reported by others.

8.1.3 Surface Topography Modification by Controlled Chattering

The second major contribution of this thesis is the invention and application of controlled chattering technology in the polymer surface topography engineering. In Chapter 5, the mechanism of controlled chattering was introduced for the first time. Proof of concept experiments were conducted on PMMA samples using an oscillating diamond knife in ultramicrotomy. It was found that by applying fast cutting speed ranging from 2-80 mm/s, and oscillation frequency between 25-45 kHz, uniform wavy patterns with feature sizes from nano to micrometer scale could be fabricated in one step. Using current technologies of nanofabrication based on lithography or self-assembly it is challenging to fabricate patterns over a long range (2 orders of magnitude) and in large scale. However, controlled chattering is able to tune pattern size over 3 orders of magnitude and is readily scalable. Moreover, since this patterning method is based on physical sectioning, it is a clean process without any chemical reactions or by products.

In Chapter 6, the controlled chattering mechanism was further investigated in depth by studying the effect of crosslinking and cutting speed on the pattern formation. Two types of polymers with different mechanical properties, i.e. PMMA and epoxy, were used. PMMA is a typical thermoplastic material with linear chain structure, while epoxy is a widely used thermosetting polymer with crosslinked structures. In sectioning linear PMMA samples, it was found that the thin sections produced at high cutting speed (30 mm/s and 25 kHz oscillation frequency) appeared twisted and broken, therefore patterns could not be retained. However, by applying a crosslinking agent to PMMA, the quality of wavy patterns was significantly improved even at higher cutting speed. In this chapter, the effect of crosslinking degree on pattern size was systematically studied. The results showed that a mild crosslinking degree (0.5-3%) increased the Young's modulus and decreased the rupture strain of PMMA; therefore, larger wavy patterns were created on the section and block surfaces. However, higher crosslinking degree (3-4%) did not further alter these mechanical properties significantly; therefore, the size of patterns was little affected. The controlled chattering results on PMMA samples were compared to those on epoxy samples. Very similar linear relationships of the pattern size to the cutting speed were observed. For both types of materials, the patterns on thin sections were found compressed along the cutting direction. Although it was difficult to totally eliminate compression, it was feasible to estimate the degree of compression based on the knife angle and cutting clearance angle. Therefore, by measuring the pattern size on the block surface (or thin section surface), the pattern size on thin section surface (or block surface) could be estimated.

8.1.4 Fabrication of Nanowire Structures by Controlled Chattering

Another useful application of controlled chattering, demonstrated in this thesis, was the fabrication of ultra-long nanowires from wavy-patterned surfaces. By conducting shallow cutting (relative to the amplitude of wavy structures on the block surface) and careful alignment of oscillation phases between two concessive cuts, ribbon-like or rod-like structures made of a variety of materials were generated. To the best of our knowledge, this is the simplest and fastest approach thus far to fabricate nanowire structures. In Chapter 7, experimental results on crosslinked PMMA, aluminum and copper were presented and discussed. The effect of phase alignment, cutting depth and cutting speed on nanowire formation as well as size control were studied. The feasibility of preparing metal nanowires was considered particularly important since conductive nanowires are in high demand in microdevice fabrication. Besides this, controlled chattering has another advantage over existing methods, which is the ability to fabricate nanowires with ultrahigh aspect ratio. For example, the copper nanowires fabricated at 8 mm/s cutting speed, 40kHz frequency and 25 nm depth, were about 70nm in width and 2mm in length. That is, the aspect ratio is about 2.8×10^4. In fact, the length of nanowires is determined by the size of the oscillation knife. It is expected that with the availability of a large oscillation knife, further increase of aspect ratios is possible.

8.2 Perspectives and Suggestions to Future Work

8.2.1 Other Functional Surfadditives for Specified Surface Modification

The successful application of multifunctional surfadditives suggests a new approach for polymer surface modification that can be finished in mold. Since

ATRP is tolerant to a variety of monomers, surfadditives with various functional groups could be synthesized and used for a diversity of property modification; for example, monomers containing ethylene oxide (EO) pendent groups such as oligoethylene glycol methacrylate (OEGMA) can be incorporated for applications where a biocompatible surface is desired;[1-3] hydrophilic monomers combined with fluorinated monomer can be synthesized and used to construct hydrophilicity "switchable" surfaces.[4-7] Azobenzenes undergo reversible photo induced isomerization rapidly at different wavelengths of light and this mechanism was successfully used to create surface patterns under the manipulation of light[8]. Recently, it was also reported that azobenzene grafted PMMA surfaces presented some properties of controlled cell adhesion[9]. The methods of attaching azobenzenes to polymer substrates in these studies were mainly based on coating or grafting. It is expected that by synthesizing azobenzene based surfadditives, the modification of polymer surface for such purposes could be also achieved. Furthermore, the surfadditive approach would be more advantageous towards industrialization as it can be applied to large-sized products and the pieces that have complex geometries, and does not involve costly operations.

8.2.2 Theoretical Studies of Migration Processes

Besides a new molecular design concept, there are also many fundamental questions remaining unresolved. For example, the surface energy driven migration of surfadditives is only qualitatively studied. It is known that the rate of polymer migration is dependent on its molecular weight, molecular structure, temperature, bulk properties, etc. however, it is not clear that how these factors determine the migration. To study this, polymers with more precisely controlled molecular weight or structure need to be prepared, for instance, in multi-step procedures. Following this, theoretical modeling as well as reliable experimental measurements will become feasible. Overall, the major limitation for the application of such polymeric surfadditives is their long time for migration (hours or even longer), being unsuitable for transient processing procedures such as injection or extrusion molding.

8.2.3 Obstacles of Using Magnetic Surfadditives

The incorporation of magnetic nanoparticles in the surfadditive resolved the slow migration issue existing in polymeric surfadditives, and the migration could be essentially finished instantly. However, the segregation of particles on the surface significantly affected optical properties of the bulk material. It was found that 0.1% of magnetic particles was enough to form a black layer on the bulk surface after surface migration. No matter how small the nanoparticles prior to migration, they eventually concentrated at specified area and aggregated into micrometer-sized chunks. These chunks significantly affected the transmission/diffraction of visible light, thus affecting the optical property of the bulk material. Due to the segregation nature of magnetic particles, it is not recommended to use magnetic surfadditives in materials of which optical properties are important.

8.2.4 Investigation of Cutting Parameters Affecting Controlled Chattering

The controlled chattering technology appears to be straightforward and mechanically simple. However, the mechanism involved in the pattern formation on the specimen surface is yet to be better understood. Whether the amplitude of wavy structure is a direct copy from the vibration of the knife-edge, or if it is also affected by material mechanical property is not clear. Among the possible cutting parameters, only the effect of cutting speed on pattern formation was systematically studied. The effect of cutting depth as well as oscillation frequency on pattern formation was not systematically investigated. Since the cutting depth is significantly affected by the elasticity of the materials to be cut, the true depth of cut could not to be accurately measured without a precision monitoring facility. On the other hand, the commercial oscillating diamond knife used in this study is only tunable from 25 to 45 kHz, which does not allow us to conduct sufficient study on this factor. It would be ideal if a new oscillation knife can be made with frequency tunable in a wider range, e.g. 1-100 kHz. Using such a knife, a quantitative study of the oscillation effect on pattern size might be feasible.

8.2.5 Extension of Controlled Chattering to Other Types of Materials

Chattering experiments have been successfully conducted on PMMA, epoxy and even soft metals such as aluminum and copper. Theoretically, this method should be applicable to any kind of materials that is suitable for precision machining. Therefore, a wider range of materials, including polycarbonate, polyester, polystyrene, semi-conductive and conductive polymers, can be tested. For some elastic materials such as PDMS, polyethylene, ABS, etc., it is not feasible to conduct precision cutting at room temperature because of the large deformation under compression. However, a cryo-sectioning facility might offer a solution since the specimens could be sectioned at the frozen state.

8.2.6 Challenging the Limits of Nanowire Length and Width

A remaining challenge in the nanowire fabrication technologies is to achieve high aspect ratio. Controlled chattering technology appears to be advantageous and have lots of room for further progresses. One approach is to develop larger knifes, therefore larger specimens can be sectioned. It is known that the length of nanowires fabricated by controlled chattering is determined by the width of the cutting tool. Ideally, a defect-free knife is able to cut nanowires with length equal to the width of the specimen (the part in contact with the knife). Therefore, the availability of high quality, large-sized knife is crucial for the fabrication of ultra long nanowires. On the other hand, high aspect ratio could also be achieved by reducing the thickness (width) of the wires. The size of the nanowires can be reduced by reducing cutting depth, cutting speed or a more sophisticated phase adjustment. It is expected to be difficult to get the lateral dimension in the sub 10 nm scale on polymer samples since the size of polymer chain is of about a few nanometers. However, this practice might be feasible if conducted on inorganic materials such as aluminum, copper, silver, gold etc. In fact, the ability to fabricate ultrathin nanowires down to a few nanometers' scale could lead to new advanced materials with unique properties. For instance, some semiconducting or conductive materials with dimensions in the sub 10 nm scale showed quantum mechanical effects[10,11], such as enhanced thermoelectric properties[12,13] or other peculiar electrical properties[14,15]. The key issues to achieve this are: using a more advanced oscillation knife with perfect knife edge and allowing for higher oscillation frequency, precision control of cutting parameters, and a careful selection of a material with the corresponding proper mechanical properties.

8.3 References

1. Lutz, J. F. *J. Polym. Sci. Pol. Chem.* **2008,** 46, (11), 3459-3470.
2. Feng, W.; Zhu, S. P.; Ishihara, K.; Brash, J. L. *Biointerphases* **2006,** 1, (1), 50-60.
3. Eisa, T.; Sefton, M. V. *Biomaterials* **1993,** 14, (10), 755-761.

4. Motornov, M.; Sheparovych, R.; Lupitskyy, R.; MacWilliams, E.; Minko, S. *Adv. Mater.* **2008,** 20, (1), 200-205.
5. Uhlmann, P.; Ionov, L.; Houbenov, N.; Nitschke, M.; Grundke, K.; Motornov, M.; Minko, S.; Stamm, M. *Prog. Org. Coat.* **2006,** 55, (2), 168-174.
6. Gras, S. L.; Mahmud, T.; Rosengarten, G.; Mitchell, A.; Kalantar-Zadeh, K. *ChemPhysChem* **2007,** 8, (14), 2036-2050.
7. Xin, B. W.; Hao, J. C. *Chem. Soc. Rev.* 39, (2), 769-782.
8. Yager, K. G.; Barrett, C. J. *Macromolecules* **2006,** 39, (26), 9320-9326.
9. Liu, D. B.; Xie, Y. Y.; Shao, H. W.; Jiang, X. Y. *Angew. Chem.-Int. Edit.* **2009,** 48, (24), 4406-4408.
10. Chen, G.; Dresselhaus, M. S.; Dresselhaus, G.; Fleurial, J. P.; Caillat, T. *Int. Mater. Rev.* **2003,** 48, (1), 45-66.
11. Yang, P. D. *MRS Bull.* **2005,** 30, (2), 85-91.
12. Hochbaum, A. I.; Chen, R. K.; Delgado, R. D.; Liang, W. J.; Garnett, E. C.; Najarian, M.; Majumdar, A.; Yang, P. D. *Nature* **2008,** 451, (7175), 163-U5.
13. Dresselhaus, M. S.; Chen, G.; Tang, M. Y.; Yang, R. G.; Lee, H.; Wang, D. Z.; Ren, Z. F.; Fleurial, J. P.; Gogna, P. *Adv. Mater.* **2007,** 19, (8), 1043-1053.
14. Yanson, A. I.; Bollinger, G. R.; van den Brom, H. E.; Agrait, N.; van Ruitenbeek, J. M. *Nature* **1998,** 395, (6704), 783-785.
15. Wang, Z. L.; Song, J. H. *Science* **2006,** 312, (5771), 242-246.

Appendix A: Diffusion of Semi-flexible Polyelectrolyte through Nanochannels

This chapter is reproduced based on the article of Gu H.; Faucher S.; Zhu S. Diffusion of Semi-flexible Polyelectrolyte through Nanochannels. *AIChE Journal*, **2010**, 56, (7), 1684-1692. Copyright © 2009 American Institute of Chemical Engineers.

Author Contributions: Hongyan Gu performed the lab experiments and data analysis. Dr. Santiago Faucher participated in some discussions and manuscript revision. Dr. Shiping Zhu supervised this work and participated in manuscript revision.

A.1 Abstract

The diffusion of sodium polystyrene sulfonate through polycarbonate nanochanels was studied in salt-free dilute aqueous solution. A stronger molecular weight dependence of diffusion was observed compared to free diffusion in dilute solution. Scaling exponentials relating polymer size to diffusivity were between Flory's theory ($D_{eff} \propto N^{-0.6}$) and Rouse's model ($D_{eff} \propto N^{-1}$), revealing a crossover regime from 3-D diffusion to 1-D diffusion. Diffusion was less hindered for the polyelectrolyte (D_{eff}/D_0), than for a rigid sphere, when the polymer/channel size ratio exceeded 0.2. This is attributed to elongated chains with reduced frictional hindrance. Simulation of the confined diffusion based on an elongated cigar model gave $D \propto N^{-1}R_t^{2/3}$ while the experimental results agree with $D \propto N^{-0.94}R_t^{2/3}$. For charged polyelectrolytes, the transition to 1-D diffusion therefore begins before the polymer radius of gyration exceeds the channel size contrary to model assumptions. We attribute this to the charged nature of the polyelectrolytes causing extended chain conformations.

A.2 Introduction

Polymer diffusion in a confined geometry has been an appealing topic for both experimental and theoretical studies given its practical importance in the fields of molecular separation, catalysis, and bio-electrophoresis[1-10]. In the last few decades, hindered diffusion of colloids or flexible polymers in synthetic membranes has been studied[11-12]. These studies attempted to analyze hindrance in terms of effective partition of polymers as well as increased drag coefficient inside channels. In these works, most solutes are modeled as either rigid spheres or Gaussian chains and sometimes as porous spheres to derive numerical expressions modeling the diffusion behaviour[13]. These models have proven true for the diffusion of spherical solutes, some flexible and linear polymers as well as branched polymers. However, these theories have seldom been applied to describe and model the diffusion of charged polyectrolytes. In the few cases where polyelectrolyte diffusion has been studied, the mediums used are typically salted causing shielding of electrostatic charges on the chain backbone and therefore diffusion behavior that is artificially akin to that of flexible polymer chains. Although complex, no experimental studies have examined the confined diffusion of highly charged polyelectrolytes with scaling theory and compared the theoretical models in a crossover region from 3-D to 1-D diffusion.

Unlike neutral polymers, polyelectrolytes dissociate in aqueous solution to form polyions and numerous counterions. In the presence of adequate electrolyte salt (e.g. NaCl), the counterions screen the charges of the polyion. However, with low or zero-salt concentration, the polyions are known to behave as wormlike (or semi-flexible) chains because of the electrostatic repulsion between charges along the chains[14-17]. Therefore, charged polyelectrolyte chains are more extended than neutral flexible polymer chains. Usually, a wormlike chain is characterized by its contour length L, being the length along the chain contour and the persistence length l_p, a length scale for measuring polymer bending rigidity. The concept of persistence length was first introduced by Kratky and Porod, as a direct measure of local conformation for a linear polymer chain in small-angle scattering experiments[18,19]. Later, it was further developed in relation to ionic strength to describe bending rigidity of semi-flexible polyelectrolyte. A longer persistence length is indicative of a relatively stiffer chain.

The static size of polyelectrolyte chain is directly related to its persistence length. In a bulk solution, where no confinement is present, a wormlike swollen chain has a radius of $R_f \approx N^{3/5} a \left(l_p / a \right)^{1/5}$ according to Flory's theory[5], where a is the size of monomeric unit and N is the degree of polymerization. Its free diffusivity thus scales as: $D_0 \propto N^{-3/5} a^{-1} \left(a / l_p \right)^{-1/5}$ once one incorporates the prior equation into the Einstein equation ($D_0 \propto k_B T / R_f$) relating the rate of diffusion of a rigid sphere to its size. Given a fixed persistence length, this model therefore predicts that the diffusivity of polymer chain is inversely proportional to its chain length (N, or alternatively molecular weight) to the power of 0.6.

In narrow channels, the chains are also free to coil so long as the channel radius R_t is larger than the coil size. But if the coil size exceeds channel size, the polymer chain must elongate to pass through the channel. de Gennes *et al*.[1,5] presented an elongated cigar model for the diffusion of polyelectrolyte chains in a cylindrical tube when the tube diameter is larger than the polymer persistence length ($2R_t > l_p$). The polymer chain is viewed as a connected sequence of blobs having a radius of b (Figure A.1a, $b = R_t$). The diffusion coefficient of the blob chain (or elongated cigar) inside tube is estimated to be: $D_{blob} \propto (aN)^{-1}(R_t / a)^{2/3}(a / l_p)^{1/3}$. For constant a and l_p, the diffusivity D_{blob} is proportional to $N^{-1}R_t^{2/3}$. The blob model is based on the assumption that the tube is filled with an extended polymer when the tube size is equal to the blob size. de Gennes' model therefore predicts that the diffusivity is inversely proportional to the number of repeat units in the polymer chain (or alternatively molecular weight).

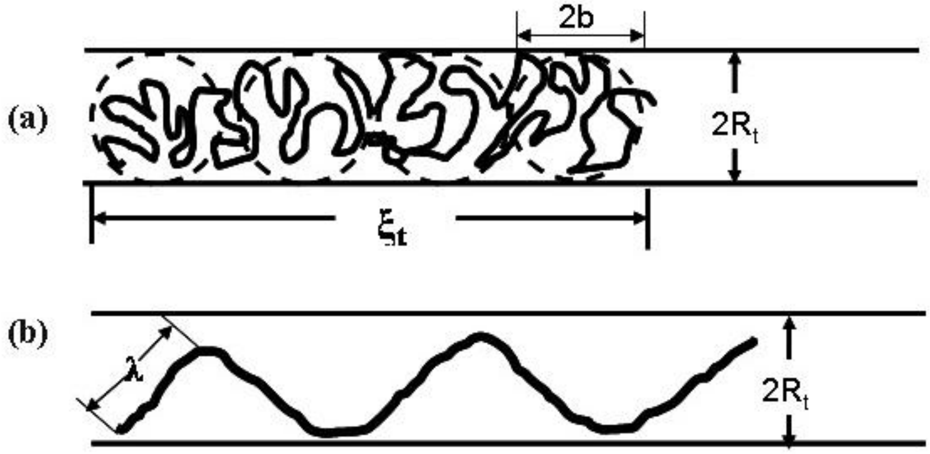

Figure A. 1 Conformation of a single polymer chain trapped into a cylindrical tube with tube diameter = $2R_t$. (a) blob model: an elongated polymer chain inside a small tube is simulated as a series of blobs where b is the radius of blob, ξ_t is the axial extension of polymer chain inside the tube. (b) Odijk model: a highly confined polymer chain inside a small tube is schemed as a more extended chain with a characteristic reflecting length of λ.

For stronger confinements where the persistence length is larger than the tube size ($2R_t < l_p$), back-folding of a polymer chain is energetically unfavorable. The chain then presents a "reflecting" conformation[18]. In this case, a length scale of $\lambda \approx \left(2R_t\right)^{2/3} l_p^{1/3}$ was introduced by Odijk to study chain dynamics. Below this length scale, the chain segment is treated as rigid rod and the whole chain can be considered as a sequence of rigid links (Figure 1b). Based on the Odijk model, the diffusivity was derived as: $D_{Odijk} \propto N^{-1} \ln(R_t / w)$, where w is the width of the rod[19,20]. Both Odijk's and de Gennes' models for confined systems therefore estimate the diffusivity to scale with the inverse of polymer molecular weight. These models therefore are in sharp contrast to those modeling diffusion behavior in a bulk system where the diffusivity is proportional to $N^{-0.6}$.

The Odijk and de Gennes models describe isolated, elongated polymer chain dynamics in a tube. While these scenarios are interesting theoretically, they are difficult to verify experimentally. However, in cases where polymer chains are moderately confined and in a crossover regime between bulk and confined diffusion, experimental validation of these models may be possible. In this work, we experimentally investigate the diffusion of charged sodium polystyrene sulfonate (PSS) chains through cylindrical nanochannels in dilute salt-free solution for the first time. The effects of polyelectrolyte chain length and channel size on the diffusion are examined and compared with different theoretical models. The radii of the nanochannels used in this study are comparable or larger than the hydrodynamic radii of the PSS coils with no more than one order of magnitude in difference. While theoretical models rely on channel size to define confined polymer chain dimensions in order to study polymer dynamics in confined spaces, the study of crossover behavior in confined spaces is experimentally feasible. This work provides new experimental evidence for the early transition between 3-D and 1-D diffusion for highly charged polyelectrolyte not previously explored.

A.3 Experimental Section

A.3.1 Materials

Sodium polystyrene sulfonate (PSS) standards prepared by sulfonation of polystyrene standards were purchased from Polymer Standards Service-USA Inc. The degree of sulfonation ranges from 85% to 90% as reported by the manufacturer. The weight average molecular weights of these polymers are listed in Table A.1. The polydispersivity indexes (M_w/M_n) of the parent polystyrene standards are lower than 1.04. Sodium benzoate (Fluka, 99.5%) was used as received. Solutions were prepared with filtered de-ionized Water from a Milli-Q water purification unit. Track etched polycarbonate (PC) membranes with uniform parallel cylindrical pores were sourced from Sterlitech Corp with the membrane sizes also listed in Table A.1.

A.3.2 Membrane Characterization

(1) Scanning electron microscopy (SEM): SEM (JEOL JSM-7000F SEM) was used to characterize the pore sizes and uniformity of the nanochannels. Track etched PC membranes were coated with gold by vacuum deposition before imaging. Two representative SEM photographs of the track etched PC membrane are shown in Figure A.2. From the images, it is evident that the pore size distribution and pore density are uniform. The pores are aligned normal to the membrane surface, so that the pore length (*l*) is considered to be equivalent to the membrane thickness.

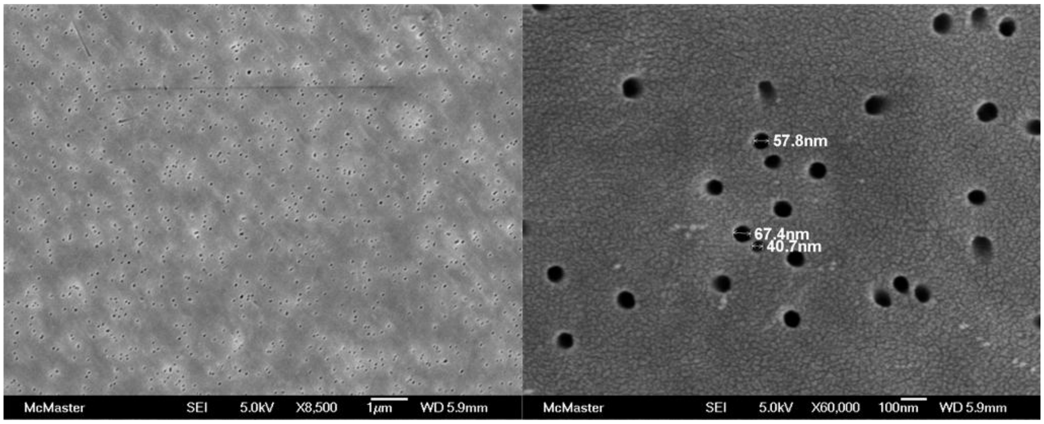

Figure A. 2 Examples of PC membrane micrographs by SEM (average $R_t \approx 27$ nm).

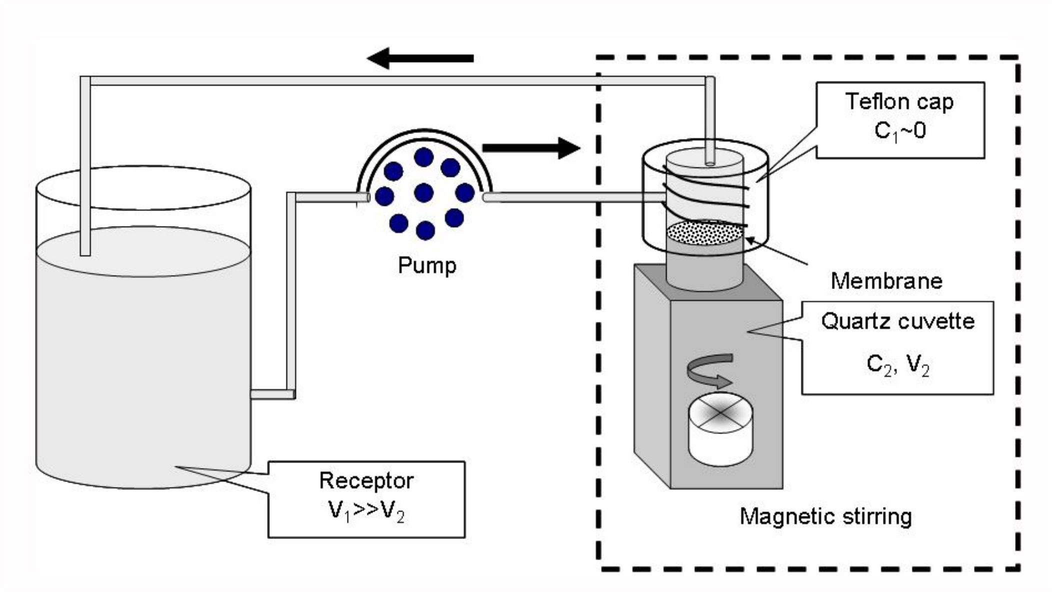

Scheme A. 1 On-line diffusion experiment setup based on a UV-spectrometer method. c_1, c_2 denotes the solute concentration in the receptor and donor chamber, and V_1, V_2 are the volumes of receptor and donor chamber. Apparatus are not to scale.

(2) Small solute diffusion experiments: The diffusion of sodium benzoate through the PC membranes was measured using the diffusion apparatus, shown in Scheme A.1, to determine porosity of the membranes prior to their use for the study of polymeric diffusion. Since the molecular size of sodium benzoate is much smaller than the membrane pore size ($R_H/R_t < 0.01$), hydrodynamic hindrance from the membrane can be neglected. The free diffusion coefficient of sodium benzoate is $D_{benzoate} = 8.63\times10^{-6}$ cm^2/s as reported in the literature[24]. Taking this value as the effective diffusion coefficient of benzoate, the membrane porosity can be calculated using mass transfer equation (Equation 1). The porosity results of three different membrane samples are listed in Table A.1.

Table A. 1 Characteristics of PSS standards and channel properties of polycarbonate membranes in this study

M_w (kg/mol)	R_H [a] (nm)	R_g [b] (nm)	R_H/R_t		
			R_t [c] = 16 nm P [d] = 0.96%	R_t = 27 nm P = 1.32%	R_t = 40 nm P = 4.1%
6.53	1.9	2.9	0.12	0.07	0.05
15.0	3.1	4.9	0.19	0.11	0.08
32.9	5.1	7.9	0.32	0.19	0.13
63.9	7.6	11.8	0.48	0.28	0.19
145	12.4	19.5	0.78	0.46	0.31

Note: [a] Hydrodynamic radius of polyelectrolyte was calculated based on Stokes-Einstein equation: $R_H = k_B T / 6\pi\eta D_0$, where k_B is Boltzmann's constant, T is the absolute temperature, η is the viscosity of water and D_0 is the free diffusivity of the solute[25]. [b] Radius of gyration was calculated by $R_g \cong 0.0829 k_B T / \eta D_0$ [25]. [c] Radius of nanochannel was averaged by SEM images. [d] Porosities, i.e. the ratio of effective diffusion area over membrane surface area, was measured by small solute diffusion experiments, using the same apparatus shown in Scheme A.1.

A.3.3 Diffusion Experiments

The diffusion experiments were conducted in a custom fabricated diffusion cell at room temperature (23 ºC). The cell was made by incorporation of a custom fabricated Teflon cap to a UV quartz cuvette (Scheme A.1). The cap was designed to seal the cuvette and simultaneously fix the track etched PC membrane to its top. In so doing, the quartz cuvette became the donor chamber while the Teflon cap served as part of the receiving chamber side of the diffusion apparatus. In this way, the solute concentration in the donor chamber could be measured on-line without invasive sampling using a UV spectrophotometer. The donor chamber was stirred by magnetic stirring and the receptor side refreshed through a re-circulating water circuit pumping fluid at a rate of 0.8 ml/min. The experimental time depended greatly on the ratio of polymer size to pore size and ranged from 5 hours to 60 hours as this ratio increased. Each experiment was repeated 3 to 4 times to obtain an average diffusivity.

A.3.4 Estimate of Diffusion Coefficient

For membrane transport at pseudo-steady state, a mass balance equation across the membrane is given by:

$$\frac{dn}{dt} = kA(c_2 - c_1) \tag{1}$$

Where dn/dt is the flux of solute transfer in moles/s, k is the total mass transfer coefficient, and A_s is the membrane area. With the initial conditions of $c_1 = 0$ and $c_2 = c_{2,0}$ at $t = 0$ and approximating $c_1 \approx 0$ during the length of the experiment ($V_1 >> V_2$), integrating Equation (1) yields:

$$\ln \frac{\Delta c_t}{\Delta c_0} = -\frac{kA}{V_2} t \tag{2}$$

where V_2 is the volume of donor chamber, t is the duration of measurement (typically between 5 and 60 hours), and Δc_t and Δc_o are the solute concentration difference between two chambers at time t and the beginning respectively. The inverse of mass transfer coefficient ($1/k$) is the mass transfer resistance, which is composed of the membrane resistance (l/pD_{eff}), the entrance/exit effects ($\pi R_t/4pD_0$) and the boundary layer resistance (δ/D_0) on both sides of the membrane. The following approximation was derived by Malone and Anderson:[26]

$$\frac{1}{k} = \frac{l}{D_{eff}\, p} + \frac{\pi R_t / 2}{D_0 p} + \frac{2\delta}{D_0} \tag{3}$$

Where D_{eff} is the effective diffusion coefficient inside pores, p is membrane porosity, and δ is the boundary layer thickness on each side of the membrane. The entrance/exit effect adds two equivalent transfer length of $\pi R_t/4$ to the total path in pores. Since the channel length used here is 6 µm, and the pore radii range from 16 to 40 nm, the maximum end effect to membrane transport is less than 1 %. Considering the effective diffusivities of PSS in membranes were much smaller than the bulk diffusivities, the end effect to membrane transfer resistance is negligible.

On the other hand, the boundary layer thickness δ is correlated with bulk diffusivity at a fixed stirring rate based on Colton and Smith's prediction[27]:

$$\delta \propto D_0^{1/3} \tag{4}$$

Thus equation (3) and (4) implies the boundary layer resistance becomes more significant for small, fast diffusing solutes transport through membrane.[9] In the worst case when the smallest PSS (M_W =6530 g/mol) diffuse through the largest pores (R_t =40 nm), the maximum boundary layer effect was about 20% of the total resistance. Our results were also compared with literature measurement on the same type of track-etch membrane with similar pore sizes[28,29]. The membrane boundary layer effect can also be estimated by analytical method[30], given that the membrane used here has very low porosity and the diffusion experiments were conducted under sufficient stirring.

A.4 Results and Discussion

Table A.2 summarizes our experimental results. The diffusion coefficient of sodium polystyrene sulfonate inside the track etched polycarbonate membrane nanochannels clearly decreased with increasing polymer molecular weight, M_W, and increased with increasing nanochannel radius, R_t. The polymer's free diffusion coefficient in the diluted bulk solution, D_0, was obtained through extrapolation of the diffusion data of highly charged PSS to infinite dilution by Tanahatoe and Kuil[31]. The effective diffusion coefficient of the polyelectrolyte through the nanochannel, D_{eff}, was measured by the UV diffusion cell in a dilute solution with the polyelectrolyte concentration less than 1/10 of the overlap concentration of each polymer, typically in the range of $c_2 = 0.5 \sim 1.0$ g/L.

Table A. 2 Summary of PSS diffusion coefficient data in PCTE membranes

M_W kg/mol	$D_0 \times 10^{-7}$ cm^2/s	$R_t = 16$ nm		$R_t = 27$ nm		$R_t = 40$ nm	
		$D_{eff} \times$ $10^{-7} cm^2/s$	D_{eff}/D_0	$D_{eff} \times$ $10^{-7} cm^2/s$	D_{eff}/D_0	$D_{eff} \times$ $10^{-7} cm^2/s$	D_{eff}/D_0
6.53	12.9	6.81	0.53	9.23	0.725	11.56	0.89
15.0	7.84	3.55	0.45	4.99	0.64	6.127	0.78
32.9	4.84	1.52	0.31	2.56	0.53	3.35	0.69
63.9	3.23	0.81	0.25	1.45	0.45	2.12	0.66
145	1.96	0.29	0.15	0.45	0.24	0.75	0.38

A.4.1 Dependence of Diffusion Coefficient on Polymer Molecular Weight

The diffusion coefficient is predicted to be proportional to $N^{-0.6}$ for a molecule following a self-avoiding random walk in a good solvent (N is the number of repeat units in the polymer chain, and N is proportional to M_W). While the direct diffusion measurement of charged polyelectrolyte at infinitely low concentrations and in salt free solution is challenging, Tanahatoe and Kuil [31] analyzed their diffusion data in a salt system and showed the molar mass dependence of diffusion $D_0 \propto N^{-0.61}$, which is in agreement with polymer free diffusion theory.

However, in our work, the presence of nanochannels caused a stronger dependence of diffusion on molecular weight. As observed in Figure A.3, the slope of the best fit provides a power law index of the molecular weight dependence for each set of experiments with a fixed pore size. As the nanochannel size decreased from 40 nm to 16 nm, the exponent on molecular weight relating it to diffusion decreased from -0.85 to -1, owing to the increased constraints from the channel wall ($D \propto M^{-0.85}$ to M^{-1}). In the smallest channel size (R_t = 16 nm), where the polymer/pore size ratio (R_H/R_t) ranged from 0.12 to 0.5, the molecular weight dependence of diffusion was very close to that predicted by de Gennes ($D \propto M^{-1}$) for highly confined chains ($R_H/R_t < 2$).

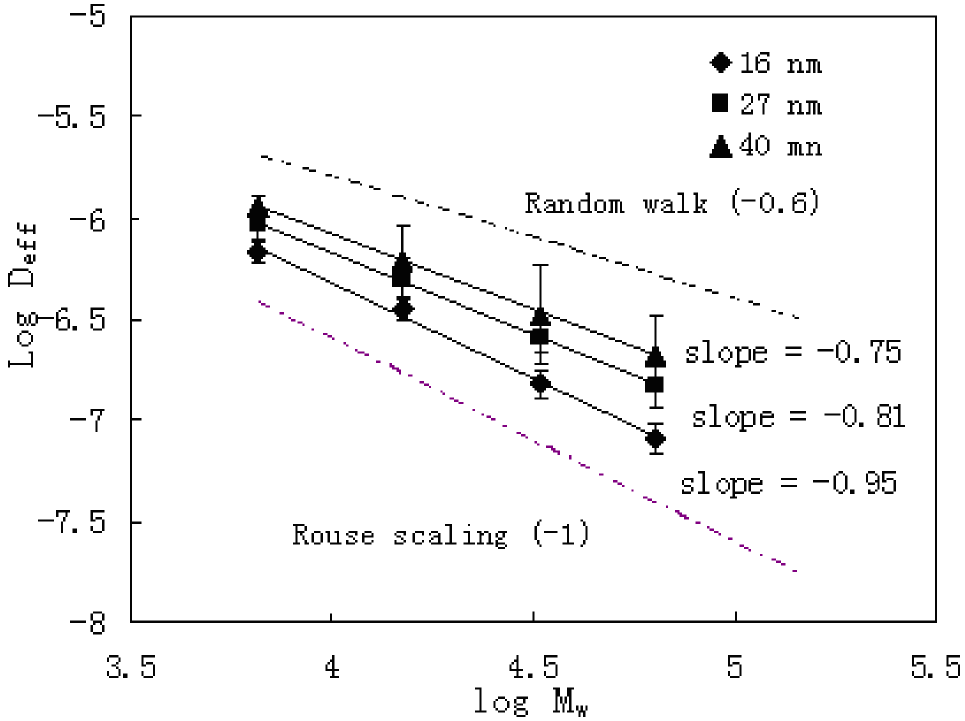

Figure A. 3 Effective diffusivity as a function of molecular weight (M_w) for varying nanochannel sizes in a logarithm scale. The dashed line (slope of -0.6) and dash-dot line (slope of -1.0) represent the expected slope for free diffusion (3-D, Flory) of polymer chains in a good solvent and for constrained diffusion of polymers in channels (1-D, de Gennes, Rouse, and Pincus) respectively.

The trend we observed for the polyelectrolytes through the precisely perforated polycarbonate membranes is comparable to that for polystyrene diffusion through non-structured porous glass. Guo *et al.*[32] reported that the diffusion of polystyrene through porous glass was inversely proportional to molecular weight when the polymer/pore size ratio (R_H/R_t) was between 0.2 and

0.5. When $R_H/R_t > 0.6$, a stronger molecular weight dependence ($D \propto M^{-v}$, $v > 1$) was observed. In their work, however, the pore structure in the porous glass was highly inter-connected and tortuous making it difficult to determine the diffusion path length and pore size. To address this, they developed a correction based on "cavity and bottleneck models" to give an average value. In contrast, our approach did not require this correction since the nanochannels were well defined. The nanochannels in the PC membranes were isolated fine cylindrical tubes with high uniformity and therefore the influence of geometrical defects was not expected. Nevertheless, Guo's work provided interesting data describing a behavior akin to that we observed in this work for a fine structure now commercially available.

The data in Figure A.3 suggest a transition from 3-D diffusion to 1-D diffusion, taking place in the range of medium confinements ($0.1 < R_H/R_t < 0.5$). It should be pointed out that de Gennes' 1-D elongated cigar model postulated the blob size equal to the tube size and the confined chain aligned in the axis of the tube (Figure A.1a). In such a scenario, one would expect that the confined polymer chain has a R_H much larger than the tube size R_t. This appears not to be the case in our work since we observed the behavior described by de Gennes for $R_H/R_t \approx 1$ to occur at $R_H/R_t \approx 0.1$.

Pincus modeled the dynamics of an isolated and stretched chain in a good solvent under external force (hydrodynamic fluctuations, velocity gradients, or electrical fields, etc.) instead of the geometrical confinement.[33,34] Based on scaling theory, Pincus applied a tensile force *f* to the end of polymer chain. The stretched chain was represented as a sequence of blobs with the blob size

$$b_{Pincus} = k_B T / f \tag{5}$$

In contrast to de Gennes' confined chain, the stretched chain allowed for lateral fluctuations within a small range, but this difference did not affect the scaling law of chain dynamics. Therefore, the simulated dynamics of both chains were similar except for their numeric coefficients[1]. That is, if the confined chain in a narrow tube in de Gennes' theory is replaced by Pincus' elongated chain with smaller blob sizes, using the Kirkwood calculation method to determine chain mobility, the diffusion coefficient inside tubes scales analogously as $D \propto N^{-1}$. Both de Gennes and Pincus scalings are based on the assumption that cooperative motion of the segments due to hydrodynamic interaction is negligible, which result in a "free draining" motion style in consistent with the Rouse diffusion model ($D_{Rouse} = k_B TB / N$ or $D_{Rouse} \propto N^{-1}$, where B is the monomer mobility in solution)[35]. One should note that the scaling of diffusivity with chain length isolates hydrodynamic interactions but the channel size is also a combined effect which is related to the conformation of the chain and the drag on segments. In the following section, we will analyze diffusion data in different approach accounting for both polymer and channel size effect.

A.4.2 Comparison with Rigid Sphere Model

In many engineering situations, the diffusion of polymers in porous membrane or small channels is characterized in terms of diffusion hindrance, which is defined as the ratio of effective diffusion coefficient over free diffusion in solution (D_{eff}/D_0). The diffusion hindrance is considered as a product of partition coefficient and hydrodynamic interaction between chain and wall[11]. In this manner, Renkin modeled the diffusing solute as a rigid sphere that is geometrically constrained by the centre line of a confining cylindrical pore[7]:

$$\frac{D_{eff}}{D_0} = (1-\frac{R_H}{R_t})^2 \times [1-2.1(\frac{R_H}{R_t})+2.1(\frac{R_H}{R_t})^3-0.95(\frac{R_H}{R_t})^5] \qquad (6)$$

The first term in the product represents the reduction of effective diffusion area when the solute has a finite size, as a result of steric exclusion from the pore wall. In other words, the effective diffusion channel is smaller in its cross section than the entire channel, because the center of particle (or centre of mass) can only pass through an area with a radius of (R_t-R_H)[36]. In an deal case, this term is approximately equal to the partition coefficient of a spherical solute in a cylindrical channel. The partition coefficient is defined as the ratio of polymer concentration inside a porous media over the concentration outside of it when the system reaches an equilibrium[12]. The second term in the product is the friction factor between solute and pore wall, theoretically derived by Faxen[37,38]. This equation was extensively verified by confined diffusion experiments of urea, glucose, antipyrine, sucrose, in porous membranes, typically when $R_H/R_t < 0.32$. In addition, subsequent studies on the diffusion of linear polymers in track etched membranes or other porous membranes were also reported for testing the theory with the polymer/pore size ratios up to 0.8[9,10,39-41]. A very good review paper by Deen compared the existing theoretical models with some spherical solute diffusion experiments in membranes having cylindrical pores[11]. In most of these studies, flexible linear polymer chains were adequately large to be treated as hydrodynamic particles or porous rigid spheres, given a characteristic size of R_g or R_H.

Figure A.4 shows that D_{eff}/D_0 decreased as the polymer/pore size ratio R_H/R_t increased. This is expected since there was a reduced partition of solute inside the nanochannels as compared to the bulk condition. At higher $\mathrm{R_H/R_t}$ ratios, the effective diffusion of PSS was significantly faster than the predicted. If we eliminate the hydrodynamic friction effect in the model (i.e., the second term in the product in Equation (6), the predicted partition coefficient (the dashed curve in Figure A.4) is close to the experimental data. The frictional hindrance from the channel wall on the polymer is therefore noted but its effect is smaller than that predicted by a rigid sphere model.

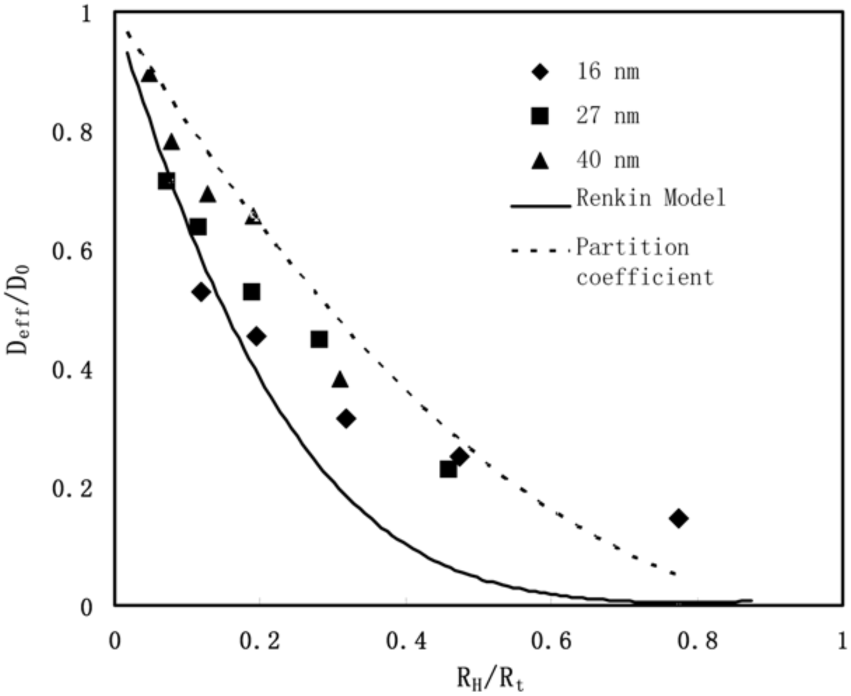

Figure A. 4 Plot of the effective-to-free diffusivity ratio as a function of polymer-to-pore size ratio. Solid curve represents Renkin's model. Dashed curve is the reduced partition coefficient of spherical solute inside the cylindrical channel as a function of the polymer/pore size ratio estimated by $(1-R_H/R_t)^2$.

A similar deviation from the Renkin model was reported by Deen et al.[29] for the hindered diffusion of dextran and ficoll polymer through PC membranes. Dextran is a linear polysaccharide while ficoll is a crosslinked copolymer of sucrose and epichlorohydrin. Both polymers were selected with a series of molecular weights having similar hydrodynamic radius, with the polymer/pore size ratio ranging from 0.2 to 0.8. It was found that within the same PC microchannels, linear dextran diffusion was faster than that predicted by the rigid sphere model while ficoll diffused remarkably slower than the predicted. It was postulated that the deformation of linear chains inside the pores could potentially reduce the frictional hindrance from the wall thus allowing for faster diffusion rates than rigid spherical molecules (ficoll).

The measurement of the size effect on diffusion inherently depends on the method used for measuring polymer configuration (R_H). Our calculation of PSS molecule size was based on the Stokes-Einstein equation, which is the equivalent hydrodynamic radius of a spherical solute having the same diffusion coefficient. This definition is extensively used for coiled polymer diffusion in unbounded solutions. However, it is not a true radius defining the boundary of a polymer chain. Particularly, for polymer chains possessing irregular or elongated configuration, the radius dimension is just a characteristic length scale related to its mobility. In order to gain perspective on the rigidity of polyelectrolytes in regards to diffusion hindrance, we examined the literature data related to persistence length, Debye screen length, and contour length scale[17,21,22,31]. The PSS chain length information is summarized in Table A.3 and analyzed below.

Table A. 3 Molecular weight *(M_W)*, number of repeat units *(N)*, and contour length *(L)* of the sodium polystyrene sulfonate (PSS) standards without added salt in dilute solution.

PSS standards.	Standard 1	Standard 2	Standard 3	Standard 4	Standard 5
M_W *(kg/mol)*	6.53	15.0	32.9	63.9	145
N [a]	32	73	160	310	704
L [b] *(nm)*	5.4	12.4	27.2	52.7	120

[a] Degree of polymerization, derived from polymer molecular weight (M_W) divided by monomer molecular weight. [b] contour length calculated with the monomeric distance = 0.17 nm[31].

The stiffness of a charged polyelectrolyte chain can be characterized by its contour length L and persistence length l_p. Based on the study of Kassapidou et al.[42] the persistence length l_p for PSS in a salt-free solution is 15.8 nm and 18.6 nm at ionic strengths of 0.004 and 0.001 mol/L. Lower ionic strength results in longer l_p for the same polyelectrolyte since the charges on the backbone are not as effectively screened. An estimate of the confined PSS l_p in this work is difficult, since the polyelectrolyte concentration and counterions are restricted by the channel size. If we assume the concentration of monomer units inside the channel is governed by the partition effect only and the counterions distribute homogeneously in the system, the monomer concentration inside the channel can be estimated as:

$$c_{m,tube} = (1 - R_H / R_t)^2 c_{m,bulk} \tag{7}$$

where $c_{m,tube}$ is always lower than 0.004 mol/L. The PSS persistence lengths in this study are therefore l_p>15.8 nm. This length scale is most likely in the same order of magnitude with the contour lengths L of the five PSS standards listed in Table A.3. Therefore we can consider the polymer chains to be extended and rod like in their conformation.

A second challenge in determining charged chain conformation relates to the electrostatic interactions that occur in salt-free solution, which is usually modelled with the Debye-Huckel approximation[23]. Based on the assumption that there is no inter-chain charge stiffening, and electrostatic screening is only caused by noncondensed counterions, the calculation of Debye-Huckel screening length (κ^{-1}) for salt-free polyelectrolytes can be simplified to [23,43]

$$\kappa^{-1} = (4\pi l_B c_m)^{-1/2} \tag{8}$$

where l_B is the Bjerrum length, c_m is the monomer concentration in a unit volume. This equation shows the Debye-Huckel screen length is directly determined by the monomer concentration, lower concentration results in longer screen length with square-root dependence. Given a Bjerrum length of 0.7 nm for water at 25 °C, and an average monomer concentration of 0.002 mol/L in this study, κ^{-1} is estimated to be 7.8 nm. This screen length is in the order of the contour length and persistence length scale, again this indicates the macromolecule likely takes on an elongated configuration.

Park et al. studied the statistical mechanics of polyelectrolyte in cylindrical pores with a Gaussian chain assumption based on a Debye-Huckel screen length[44,45]. Taken into account were the effects of screened electrostatic interactions and the excluded volume effect between monomeric unit and pore wall as well as between monomeric unit pairs. Neglecting the counterion condensation, they found a crossover of chain conformation from stretched ($R_g \propto L$ if $R_g \leq \kappa^{-1}$) to self-avoiding chain ($R_g \propto L^{3/5}$ if $R_g > \kappa^{-1}$) regime. If we apply Park's simulation to the present work, the PSS standards 1 to 4 would have a stretched conformation since R_g is in the same magnitude of κ^{-1}. However, the equilibrium partition concentration of Sample 5 with a large coil size is significantly reduced since the polymer size approaches the channel size. That is, the electrostatic screening length scale would increase according to Equation (8). Again, although the R_g of Sample 5 in bulk is about 19.5 nm, which appears sufficiently long to behave as a self-avoiding coil, when confined in the channels with R_t = 16, 27, 40 nm, the partition concentration of the large PSS inside channels would be reduced to a factor of 0.05, 0.29 or 0.48 of the bulk concentration, respectively. This dilution thus leads to longer Debye-Huckel screening lengths of up to 30 nm in small channels. Therefore, the large polyelectrolyte chain would also deform and elongate inside the small channels. This rigid extended chain conformation explains the enhanced molecular weight dependence of diffusion in nanochannels and thus following a different hindrance model in comparison with the solid sphere model.

A.4.3 Scaling of Diffusivity Based on Elongated Blob Chain Model

Given the lack of a complete fit with the rigid sphere model, and the indication of extended conformation for most of the polymer samples inside nanochannels, we correlated our data to the theories pertaining to chains that are stretched such as de Gennes' elongated cigar model or Odijk's theory. The crossover behavior between de Gennes and Odijk regimes is currently not fully understood. However we can speculate that Odijk's model is better suited than de Gennes' cigar model to account for diffusion of polymers under stronger confinement. A rough critical confinement size was identified by Reisner et al by measuring DNA extension and relaxation time inside square shaped nanochannels (channel width ranged from 30 to 400 nm). They found the crossover behavior between de Gennes and Odijk's regimes when the channel width is about twice of the DNA persistence length.[46] Below this critical width, bending rigidity becomes significant (Odijk's model) and power law scaling of relaxation time with channel width disagrees with de Gennes' prediction. If we equate the cylindrical channel diameter with square channel width in this study, the three membrane diameters ($2R_t$ = 32, 54, 80 nm) are generally over twice of the polyelectrolyte persistence length (15-18 nm). That is, the polyelectrolyte chains should retain bending and backfolding segments, which could be better explained by the blob model.

Given that the hydrodynamic radii or radii of gyration of the present polymer standards are smaller than the radii of channels in the membranes, the lateral dimension of stretched chains should have even smaller size if they orient along the nanochannel axis. To apply the blob chain model in this study, we hence assume the equivalent blob size (b) of a confined polyelectrolyte chain is $b = \gamma R_t$, where γ is a constant factor less than 1. Therefore the number of monomeric units inside a blob is defined as:

$$g = \left(\gamma R_t / a\right)^{1/\nu} \tag{9}$$

where ν is Flory exponent = 3/5, a is the monomer size. The dimension of the polymer chain inside channel ($l_{//}$) therefore is:

$$l_{//} = N^*(\gamma R_t) = \left(N / g\right)(\gamma R_t) = \left(aN\right)\left(\gamma R_t / a\right)^{-2/3} \tag{10}$$

where N^* is the number of blobs ($N^*=N/g$). The friction coefficient of the polymer chains inside the channel is thus

$$\zeta_{chain} = 6\pi\eta l_{//} \tag{11}$$

Finally, the diffusion coefficient inside the channel is described by:

$$D_{eff} \propto \frac{T}{6\pi\eta l_{//}} \propto (aN)^{-1}(\frac{\gamma R_t}{a})^{2/3} \qquad (12)$$

Given that *a* and γ are numerical constants, a simplified scaling law of diffusion as a function of chain length and channel size is:

$$D_{eff} \propto N^{-1} R_t^{2/3} \qquad (13)$$

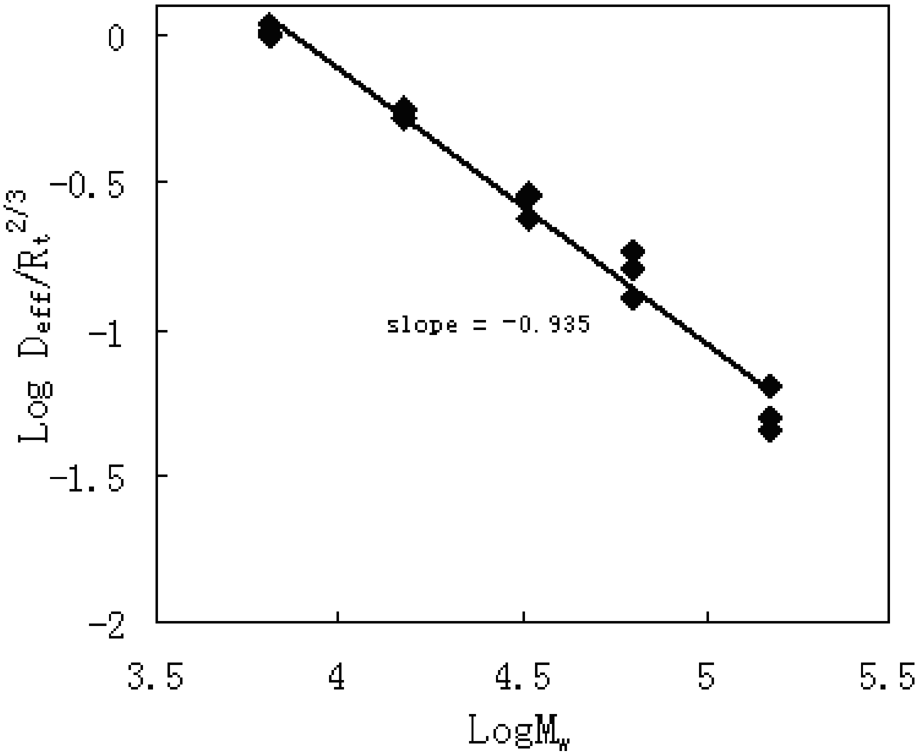

Figure A. 5 Effective diffusivity divided by the channel radius to the 2/3 power versus PSS molecular weight.

To test the applicability of Equation (13), the effective diffusion coefficient of the five standards over the channel sizes to the power predicted by the blob theory was plotted against molecular weight. As shown in Figure A.5, the majority of the data points fall nicely onto a master curve with a slope = -0.95, which is close to the -1 power predicted for elongated chain diffusion. We therefore conclude that the diffusion of polyelectrolytes in salt-free solution can best be modelled as rigid rod like molecules with little to no frictional retardation.

A.5 Conclusions

We studied the confined diffusion of polyelectrolyte in a salt-free environment through PC membrane nano-channels with the polymer/pore size ratios ranged from 0.05 to 0.8. Scaling of the effective diffusion coefficient versus molecular weight revealed a diffusion mechanism that is distinct from that observed in bulk (i.e., self-avoiding walk) with $D_0 \propto N^{-3/5}$. The chain length dependence of the effective diffusion inside the nanochannels ranged from $D_{eff} \propto N^{-0.85}$ to $D_{eff} \propto N^{-1}$ as the channel size decreased. Although the equivalent hydrodynamic radii of polymers were smaller than the nanochannel sizes, the inverse proportion of diffusion coefficient with chain length was indicative of 1-D diffusion behavior. The hindrance of confined diffusion coefficient of such polyelectrolyte was found to be smaller than that of rigid sphere solutes. Scaling of the diffusivity with molecular weight and channel size showed good agreement with the blob theory, which is indicative of elongated/stretched conformation of the polyelectrolyte. The polyelectrolyte chain was modeled as a sequence of blobs with the blob size smaller than the channel size. In agreement with the blob model where the diffusivity was inversely proportional to the degree of polymerization, the experimental data showed the diffusivity proportional to the power of -0.94 ($D \sim N^{-0.94} R_t^{2/3}$). This exponent close to unity suggested the applicability of elongated chain conformation inside the nanochannel, and further intra-molecular hydrodynamic screening. In conclusion, for the charged PSS in this study, the crossover regime of free diffusion and ideal 1-D diffusion started before the polymer radius of gyration exceeded the channel size, which differs from the typical theoretical assumptions. We attributed this to the charged nature of the polyelectrolyte which caused an extended chain conformation.

A.6 References

1. Brochard, F.; deGennes, P. G. *Journal of Chemical Physics* **1977**, 67, 52-56.
2. Kremer, K.; Binder, K. *Journal of Chemical Physics* **1984**, 81, 6381-6394.
3. Sheng, Y.J.; Wang, M. C. *Journal of Chemical Physic* **2001**, 114, 4724-4729.

4. Wei, C.Y.; Srivastava, D. *Physical Review Letters* **2003**, 91, 235901.

5. Brochard-Wyart, F.; Tanaka, T., Borghi, N.; de Gennes, P.G. *Langmur* **2005**, 21, 4144-4148.

6. Yang, H.; Liu, Y.; Zhang, H.; Li, Z.S. *Polymer* **2006**, 47, 7607-7610.

7. Renkin, E. M. *The journal of general Physiology* **1954**, 38, 225–243.

8. Kimmich, R.; Fatkullin, N., Mattea, C.; Fischer, E. *Magnetic Resonance Imaging* **2005**, 23, 191-196.

9. Cannell, D. S.; Rondelez, F. *Macromolecules* **1980**, 13, 1599-1602.

10. Davidson, M.G.; Deen, W.M. *Macromolecules* **1988**, 21, 3474-3481.

11. Deen, W. M. *AIChE Journal* **1987**, 33, 1409-1425.

12. Teraoka, I. *Progress in Polymer Science* **1996**, 21, 89-149.

13. Davison, M. G.; Deen, W. M. *Journal of Membrane Science* **1988**, 35, 167-192.

14. Koene, R.S.; Mandel, M. *Macromolecules* **1983**, 16, 973-978.

15. Sedlak, M.; Amis, E.J. *Journal of Chemical Physics* **1992**, 96, 826-834.

16. Sedlak, M.; Amis, E. J. *Journal of Chemical Physics* **1992**, 96, 817-825.

17. Tanahatoe, J. J.; Kuil, M. E. *Macromolecules* **1997**, 30, 6102-6106.

18. Porod, G. *Monats. Chem.* **1949**, 80, 251-255.

19. Kratky, O.; Porod, G. *Rec. Trav. Chim. Pays-Bas* **1949**, 68, 1106-1122.

20. Odijk, T.; Houwaert A. C. *J. Polym. Sci., Polym. Phys.* **1978**, 16, 627-639.

21. Odijk, T. *Macromolecules* **1979**, 12, 688-693.

22. Odijk, T. *Macromolecules* **1983**, 16, 1340-1344.

23. Balducci, A.; Mao, P.; Han, J.; Doyle, P. S. *Macromolecules* **2006**, 39, 6273-6281.

24. Landolt-Bornstein, Numerical Data and Functional Relationships in Science and Technology (6th Edition), Vol. II/5a, Heidelberg: Springer-Verlag, **1969**.

25. Teraoka, I. polymer solutions: An introduction to physical properties, New York: John Wiley & Sons, Inc. **2002**, 239.

26. Malone, D. M.; Anderson, J. L. *AIChE Journal* **1977**, 23, 177-184.

27. Colton, C. K.; Smith, K. A. *AIChE Journal* **1972**, 18, 958-967.

28. Bohrer, M. P. *Industrial & Engineering Chemistry Fundamentals* **1983**, 22, 72-78.

29. Deen, W. M.; Bohrer, M. P.; Epstein, N. B. *AIChE Journal* **1981**, 27, 952-959.

30. Beerlage, M. A. M.; Peeters, J. M. M.; Nolten, J. A. M.; Mulder, M. H. V.; Strathmann, H. *Journal of Applied Polymer Science* **2000**, 75, 1180-1193.

31. Tanahatoe, J. J.; Kuil, M. E. *Journal of Physical Chemistry A* **1997**, 101, 8389-8394.

32. Guo, Y. H.; Langley, K. H.; Karasz, F. E. *Macromolecules* **1990**, 23, 2022-2027.

33. Pincus, P. *Macromolecules* **1976**, 9, 386-388.

34. Pincus, P. *Macromolecules* **1977**, 10, 210-213.

35. Doi, M.; Edwards, S.F. The theory of polymer dynamics, *Clarendon Press*, Oxford, England, **1986**.

36. Ferry, J. D. *The Journal of General Physiology* **1936**, 20, 95-104.

37. Faxen, H. *Ark. Mat.Astron. och Fysik* **1922**, 17, 27.

38. Bacon, L. R. *The journal of Franklin Institut.* **1936**, 221, 251-273.

39. Kathawalla, I. A.; Anderson, J. L. *Industrial & Engineering Chemistry Research* **1988**, 27, 866-871.

40. Guillot, G.; Leger, L.; Rondelez, F. *Macromolecules* **1985**, 18, 2531-2537.

41. Ichimura, S,.; Tsuru, T.; Nakao, S.; Kimura, S. *Journal of Chemical Engineering of Japan* **2000**, 33, 141-151.

42. Kassapidou, K.; Jesse, W.; Kuil, M. E.; Lapp, A.; Egelhaaf, S.; van der Maarel, J. R.C. *Macromolecules* **199**, 30, 2671-2684.

43. Dobrynin, A. V.; Colby, R. H.; Rubinstein, M. *Macromolecules* **1995**, 28, 1859-1871.

44. Park, P. J.; Sung, W. *Journal of chemical physics* **1999**, 111, 5259-5266.

45. Park, P. J.; Chun, M. S.; Kin, J. J. *Macromolecules* **2000**, 33, 8850-8857.

46. Reisner, W.; Morton, K. J.; Riehn, R.; Wang, Y. M.; Yu, Z. N.; Rosen, M.; Sturm, J. C.; Chou, S. Y.; Frey, E.; Austin, R. H. *Physical Review Letters* **2005**, 94, 196101-1-4.

Appendix B Additional TEM Images of Nanowires Fabricated by Controlled Chattering

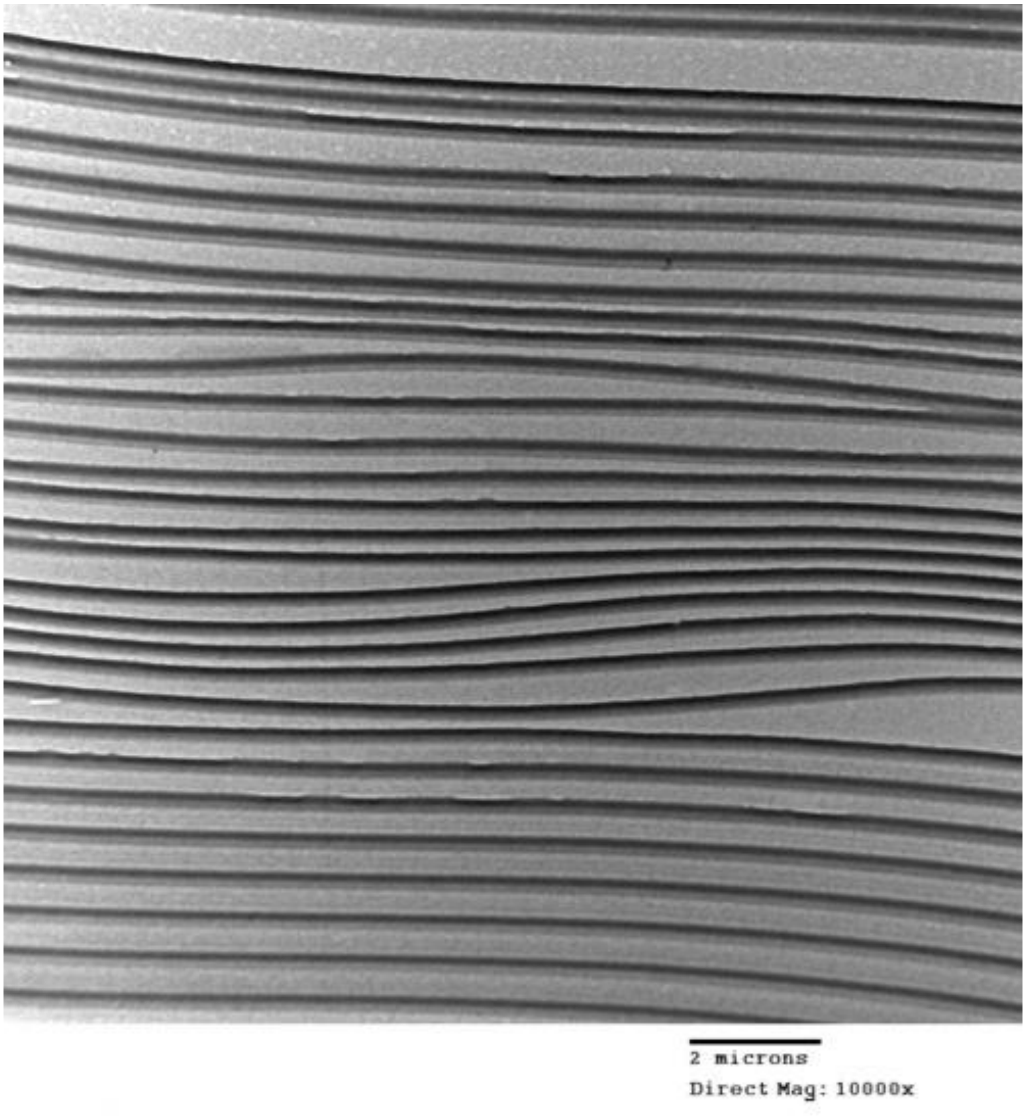

Figure B. 1 TEM of PMMA nanowires (crosslinked with 1% EGDMA) sectioned by controlled chattering at 50 mm/s cutting speed, 40 kHz oscillation frequency and 20 nm section feed. Magnification: 10,000 times.

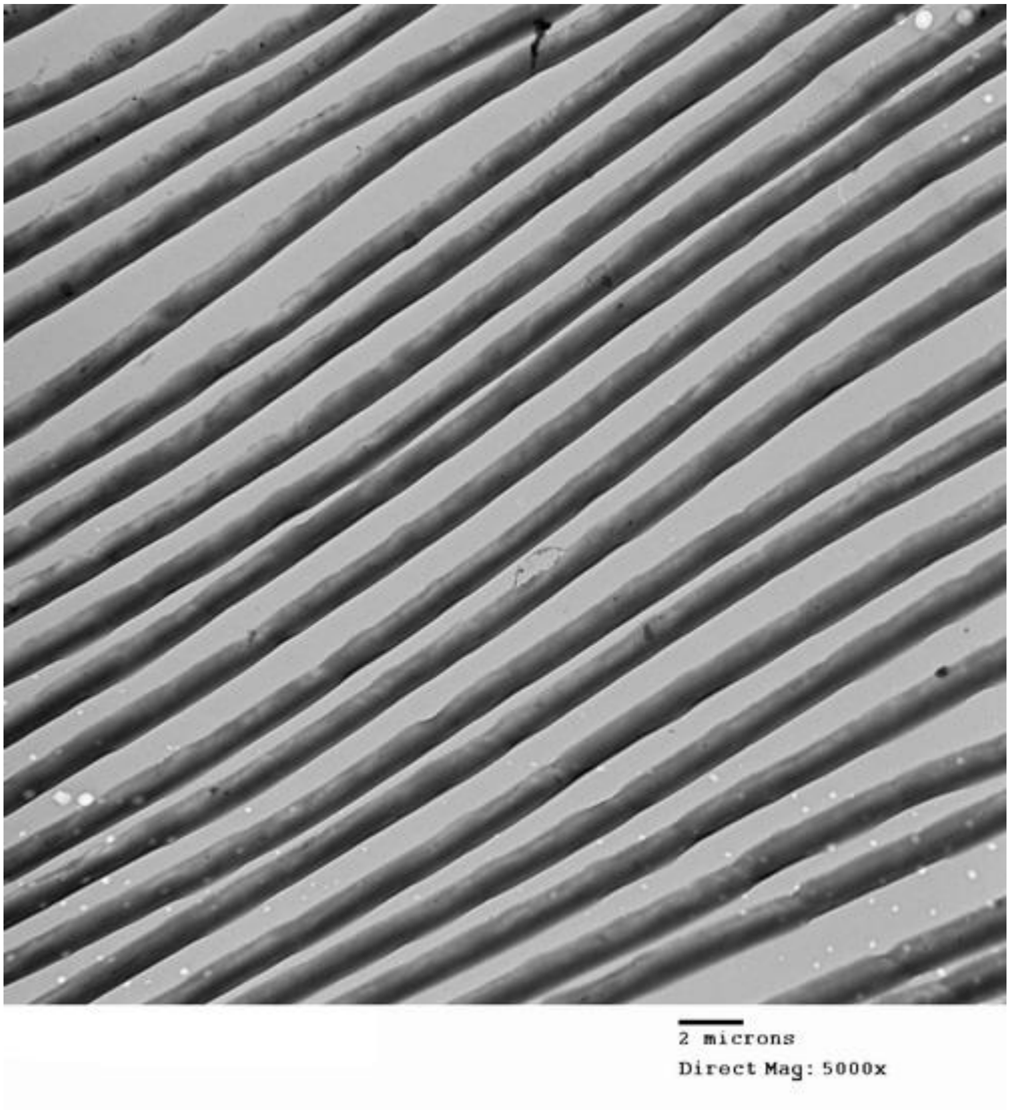

Figure B. 2 TEM of PMMA wires (crosslined with 1% EGDMA) sectioned by controlled chattering at 80 mm/s cutting speed, 40kHz oscillation frequency and 60 nm section feed. Magnification: 5,000 times.

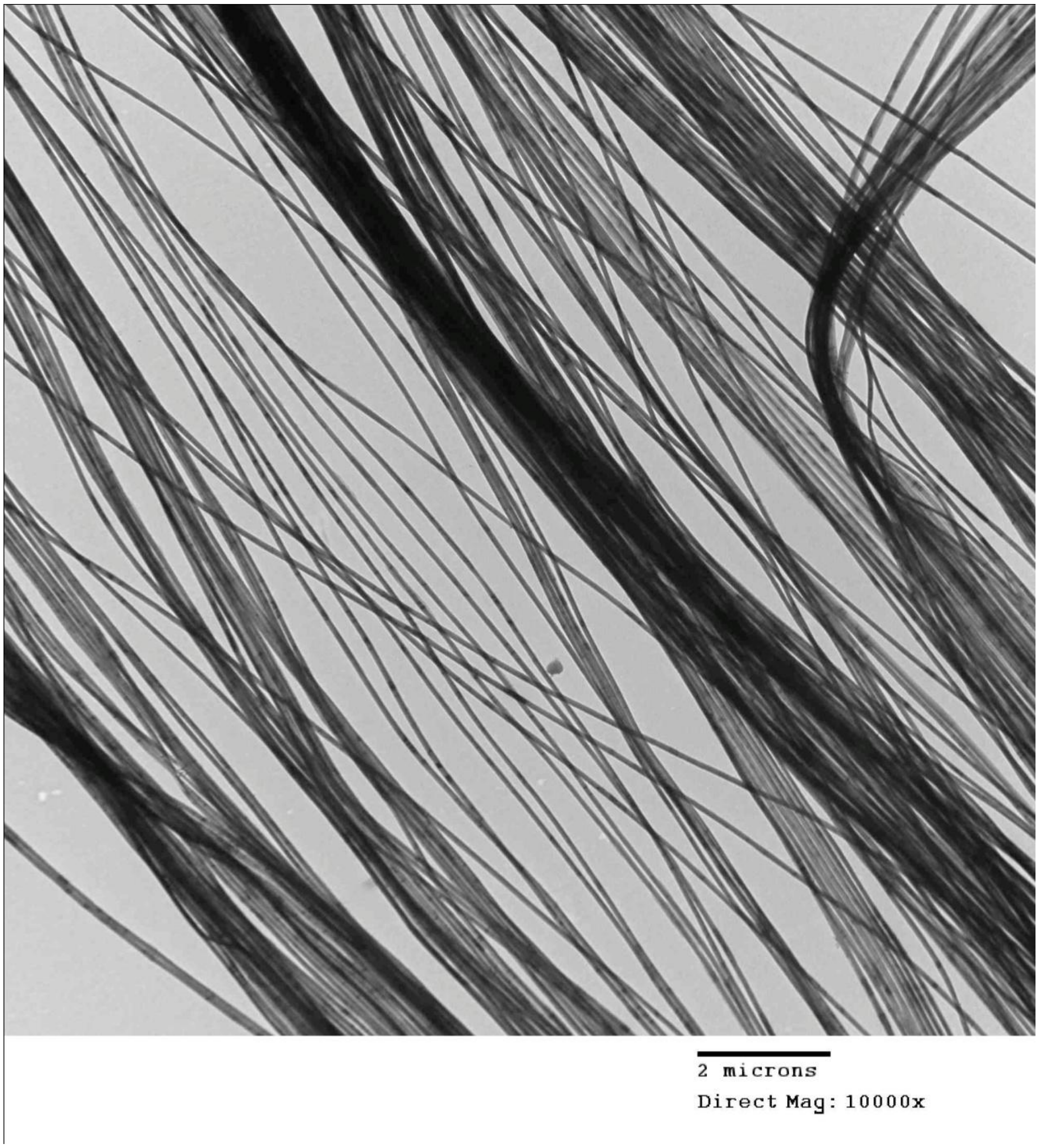

Figure B. 3 TEM of aluminum nanowires sectioned by controlled chattering at 8 mm/s cutting speed, 40 kHz oscillation frequency and 20 nm section feed at 10000 times magnification. Magnification: 10,000 times.

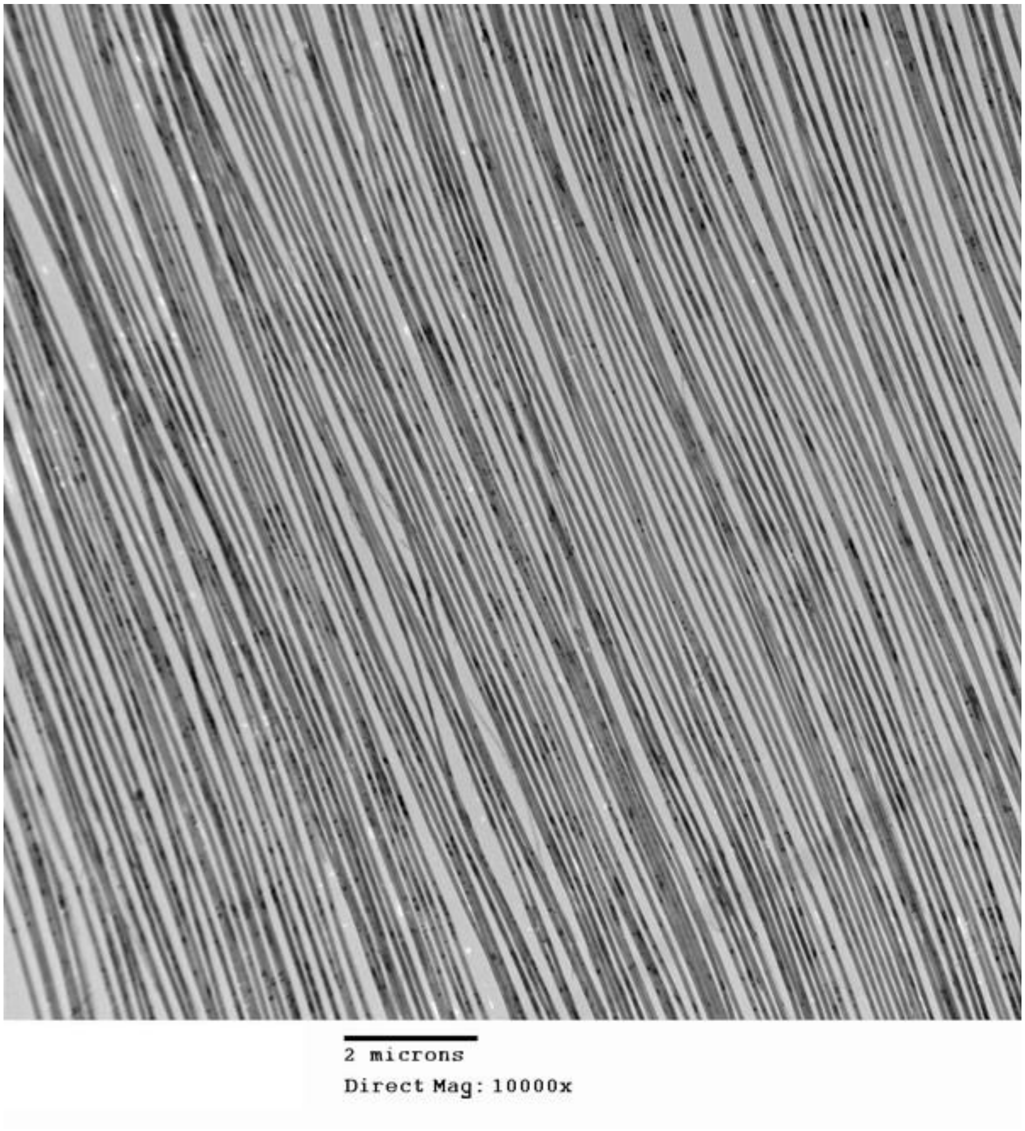

Figure B. 4 TEM of aluminum nanowires sectioned by controlled chattering at 8 mm/s cutting speed, 40 kHz oscillation frequency and 30 nm section feed. Magnification: 10,000 times.

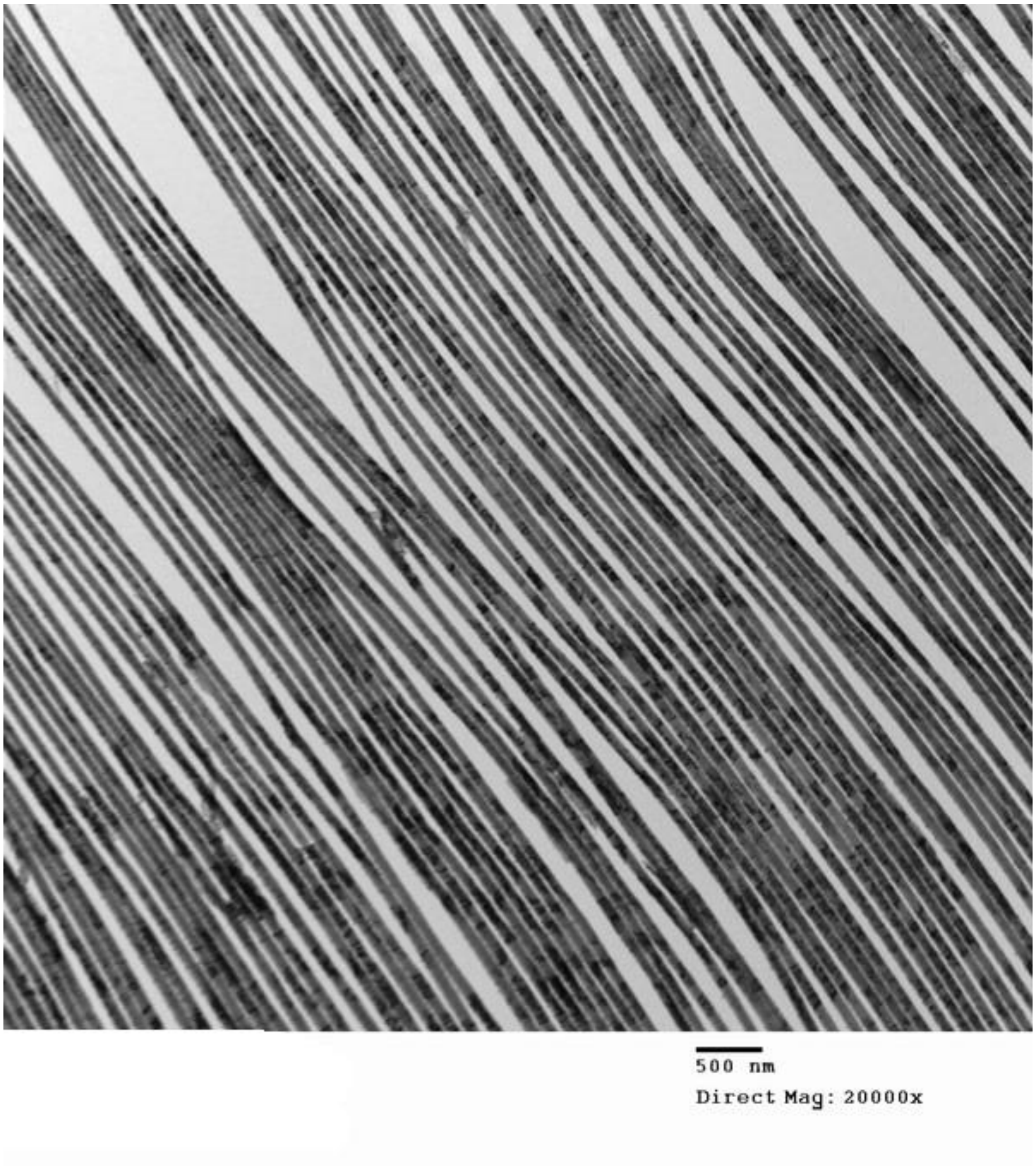

Figure B. 5 TEM of copper nanowires sectioned by controlled chattering at 8 mm/s cutting speed, 40 kHz oscillation frequency and 20nm section feed. Magnification: 20,000 times.

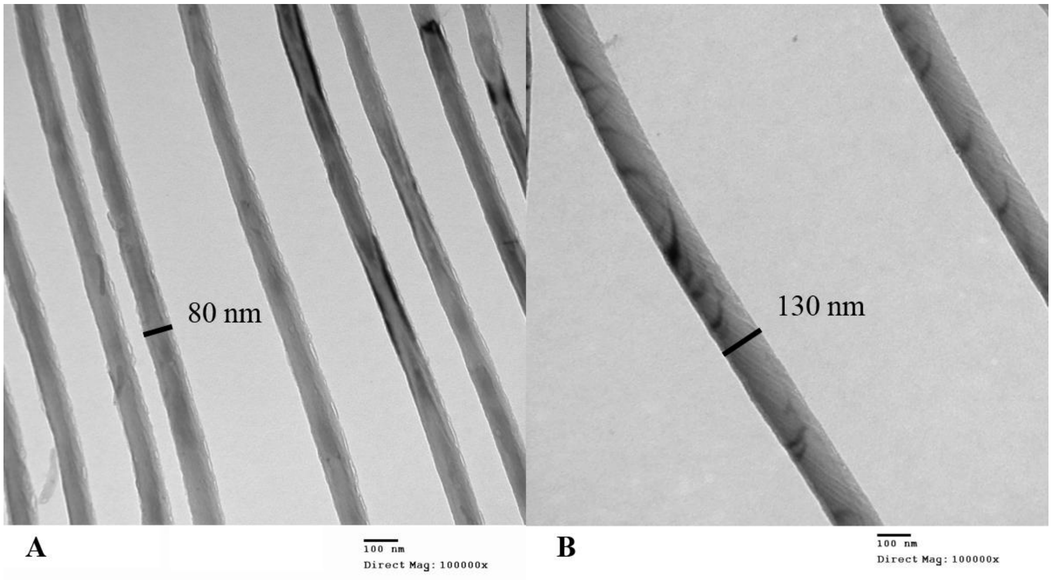

Figure B. 6 TEM of aluminum nanowires sectioned with (A) 20 nm feed, and (B) 30 nm feed. Both samples were cut at 8mm/s cutting speed, 40 kHz oscillation frequency. Images were taken at 100,000 times magnification.

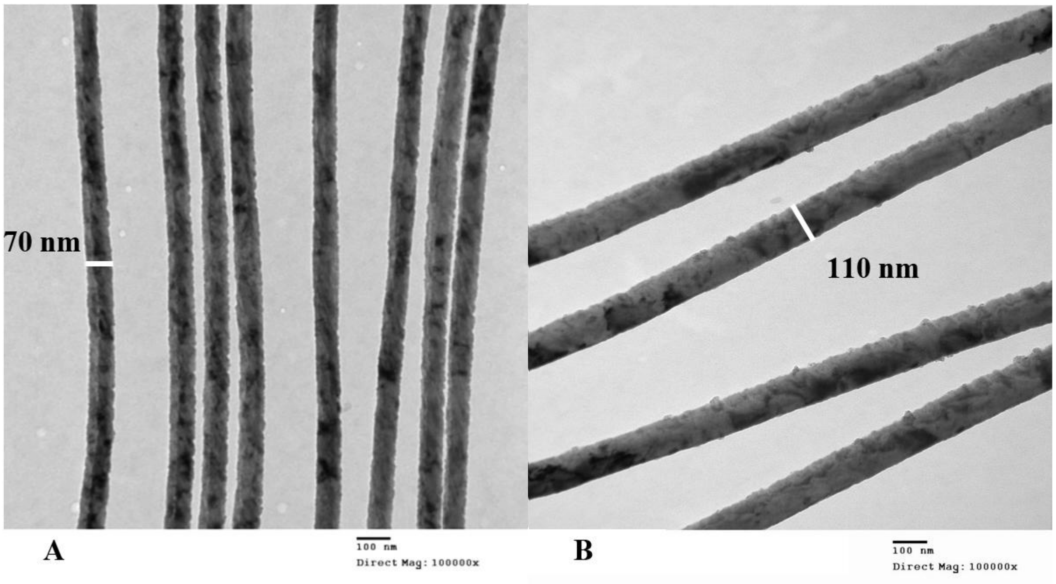

Figure B. 7 TEM of copper nanowires sectioned with (A) 20 nm feed, and (B) 25 nm feed. Both samples were cut at 8 mm/s cutting speed, 40 kHz oscillation frequency. Images were taken at 100,000 times magnification.